
**Coastal polynyas in the southwestern Weddell Sea:
Surface fluxes, sea ice production and
water mass modification**

Vom Fachbereich Physik/Elektrotechnik
der Universität Bremen

**zur Erlangung des Doktorgrades der Naturwissenschaften
Dr. rer. nat.**

genehmigte Dissertation

von

Verena Haid

 **Universität Bremen**

AWI 

2013

Eingereicht am: 22. Juli 2013

Tag des Promotionskolloquiums: 18. September 2013

1. Gutachter: Prof. Dr. Peter Lemke

2. Gutachter: Prof. Dr. Günther Heinemann

"La vraie définition de la science est qu'elle est l'étude de la beauté du monde."

Simone Weil, L'enracinement

Zusammenfassung

In den Polarmeeren werden selbst im Winter Gebiete mit geringer oder fehlender Eisbedeckung beobachtet, die sich entlang der Küstenlinie oder anderen Hindernissen für die Eisdrift bilden, wenn ablandige Winde oder in seltenen Fällen Strömungen das Meereis von der Küste fortschieben. Für den Ozean sind diese Küstenpolynjas Gebiete, in denen der Austausch mit der Atmosphäre kaum behindert wird und hohe Wärmeflüsse eine starke Eisbildung anregen. Auf den antarktischen Kontinentalschelfen sammelt sich das Salz, das beim Prozess der Eisbildung abgestossen wird, in der Wassersäule und führt zur Bildung einer sehr dichten Wassermasse, des Hochsalinen Schelfwassers (HSSW). Bei Verlassen des Kontinentalschelfes leistet das HSSW einen wichtigen Beitrag in der Bildung des Antarktischen Bodenwassers, welches im größten Teil des Weltmeeres den Boden bedeckt.

Im südwestlichen Weddellmeer erfüllen breite Kontinentalschelfe und hohe Polynja-Aktivität die Voraussetzungen für die Bildung HSSWs und es wird angenommen, dass es die wichtigste Ursprungsregion für Antarktisches Bodenwasser ist. Mit dem Finite Element Sea Ice-Ocean Model wurde die Entwicklung von Küstenpolynjas, ihr Beitrag zur Eisbildung und die daraus folgende Bildung HSSWs, sowie dessen Export mit Antriebsdaten der NCEP/NCAR Reanalyse simuliert und für den Zeitraum 1990-2009 analysiert. Außerdem wurden kürzere Modellläufe, die mit GME- und COSMO-Modelldaten angetrieben wurden, ausgeführt und die Ergebnisse verglichen.

Im 20-jährigen Mittel bedeckten Küstenpolynjas im südwestlichen Weddellmeer in den Wintermonaten Mai-September täglich eine Fläche von 9000 km^2 . Die Polynjafläche ist einer hohen zwischenjährlichen Variabilität unterworfen. Dies gilt auch für die Oberflächenflüsse in den Polynjas, jedoch in einem schwächeren Ausmaß. Je nach Region beträgt der Wärmefluss in die Atmosphäre $310\text{-}510 \text{ W/m}^2$ im 20-jährigen Mittel über die Wintermonate. Davon werden $50\text{-}60 \text{ W/m}^2$ durch den Wärmeinhalt des Ozeans aufgebracht und der verbleibende Wärmefluss führt zu Eisbildungsraten von $7\text{-}13 \text{ cm/Tag}$. Im 20-jährigen Mittel produzieren die Küstenpolynjas in den Wintermonaten 105 km^3 Meereis, was 11% der Eisbildung im südwestlichen Weddellmeer in derselben Zeitspanne (auf 0.6% der Fläche) entspricht. Im Durchschnitt ist der Wärmefluss in die Atmosphäre in den Küstenpolynjas $7\text{-}10$ mal so hoch wie im umgebenden eisbedeckten Gebiet, und da $10\text{-}20 \%$ davon durch Ab-

kühlung der Wassersäule kompensiert werden, übertrifft die Eisbildung diejenige der Umgebung um ein 9-14faches.

Im Langzeit-Modelllauf wurde die Front des Ronneschelfeises als die Region mit der stärksten Polynjaaktivität identifiziert, in der auch die höchsten Bodensalinitäten zu finden sind. Das HSSW-Volumen auf dem Kontinentalschelf weist einen starken Jahresgang und eine hohe zwischenjährliche Variabilität auf. Im Mittel werden 2 Sv ($1 \text{ Sv} = 1 \cdot 10^6 \text{ m}^3/\text{s}$) HSSW exportiert und tragen zur Bildung von geschätzt 4-6 Sv Weddellmeer-Tiefenwassers bei.

Die erheblichen Unterschiede zwischen den Windfeldern der Datensätze für den atmosphärischen Antrieb verursachen regional beträchtliche Differenzen in der Bildung der Küstenpolynjas, vor allem entlang der Küste von Coats Land und vor dem Filchnerchelfeis. Von den drei Jahren, die für einen Vergleich zur Verfügung standen, ist 2008 dasjenige, welches die größten Unterschiede aufweist. Das Jahr 2008 ist jedoch geprägt durch ein La Niña-Ereignis / einen positiven Southern Oscillation Index (SOI) und wenn es auch einen Eindruck der Spannweite vermittelt, die die Antriebsdaten in den Ergebnissen hervorrufen können, ist es nicht als typisch einzustufen.

Abstract

Even in winter, we find areas with little or no sea ice cover in the polar seas which are located at the coastline or other obstacles to sea ice drift and open, when offshore winds or in rare cases currents push the sea ice away from the coastline. To the ocean, these coastal polynyas are areas of hardly obstructed interaction with the atmosphere, where high heat fluxes induce strong sea ice production. On the Antarctic continental shelves, the salt rejected in the process of ice formation accumulates in the water column and leads to the formation of a very dense water mass, the High Salinity Shelf Water (HSSW), which upon leaving the shelf takes part in the formation of Antarctic Bottom Water, which covers most of the world ocean's bottom.

In the southwestern Weddell Sea, wide continental shelves and high polynya activity fulfill the requirements for HSSW production and it is thought the major source region of Antarctic Bottom Water. The formation of coastal polynyas, their contribution to the sea ice production and the ensuing formation and export of HSSW in the southwestern Weddell Sea were simulated using the Finite Element Sea Ice-Ocean Model with NCEP/NCAR forcing and analysed in the period 1990-2009. Furthermore, shorter model runs forced with GME and COSMO model data were branched off and compared.

In the 20-year mean, coastal polynyas in the southwestern Weddell Sea were found to cover 9000 km² daily in the winter months May-September. The polynya area features a strong interannual variability, and so do the surface fluxes within polynyas although to a lesser degree. Depending on the region, the 20-year winter mean heat flux to the atmosphere is 310-510 W/m², whereof 50-60 W/m² are supplied by the ocean's heat content and the remainder induces a sea ice production per unit area of 7-13 cm/d. The 20-year mean winter ice production in the coastal polynyas of 105 km³ contributes 11 % to the mean winter sea ice production of the southwestern Weddell Sea within the same time frame (from 0.6 % of the area). On average, we find that the atmospheric heat flux is 7-10 times higher at polynyas than in the surrounding ice-covered areas and since 10-20 % of it is compensated by the ocean's cooling, the sea ice production per unit area exceeds that of the surrounding area by a factor of 9-14.

In the long-term model run, the most active polynya region was found to be in front of

Ronne Ice Shelf, where also the highest bottom salinities occur. The HSSW volume on the continental shelf has a strong seasonal cycle and interannual variability and in the mean 2 Sv ($1 \text{ Sv} = 1 \cdot 10^6 \text{ m}^3/\text{s}$) HSSW are exported which are estimated to contribute to the formation of 4-6 Sv Weddell Sea Deep Water.

The considerable differences between the wind fields of the different atmospheric forcing data sets regionally cause substantial disparities in the formation of coastal polynyas, especially at the Coats Land coastline and in front of Filchner Ice Shelf. Of the three years that were available for comparison, 2008 featured the strongest disparities. However, 2008 is influenced by a La Niña / positive SOI event and although it illustrates the range that forcing data can induce in the results, it is not considered a typical year.

Contents

1	Introduction	13
1.1	Impact of coastal polynyas on ocean and atmosphere	14
1.2	The Weddell Sea	17
1.2.1	Location and topography	17
1.2.2	Weddell Sea water masses and bottom water formation	20
1.3	Coastal polynyas in the Weddell Sea	24
2	Model description	27
2.1	The Finite Element Method (FEM)	27
2.2	The Finite Element Sea ice-Ocean Model FESOM	28
2.2.1	The ocean component: FEOM	28
2.2.2	The sea ice component: FESIM	29
2.2.3	The coupling of FEOM and FESIM	33
2.2.4	Configuration and initialisation of FESOM	36
2.3	Atmospheric forcing of FESOM	37
2.3.1	NCEP/NCAR Reanalysis	38
2.3.2	GME	38
2.3.3	COSMO	39
3	Model validation	43
3.1	Omissions in the applied version of FESOM	43
3.1.1	Influence of tides	43
3.1.2	Influence of ice shelf cavities	44
3.1.3	Influence of icebergs	46
3.2	Sea ice concentration	46
3.3	Sea ice thickness	51
3.4	Temperature and salinity of the on-shelf water column	55
3.5	Temperature and salinity in the deep Weddell Sea	60

4	Heat flux and sea ice production	65
4.1	Seasonal cycle in the southwestern Weddell Sea	65
4.2	Spatial distribution during the winter months	70
4.2.1	Multi-year mean fields	70
4.2.2	Regions of interest	72
4.3	Regional characteristics	73
4.3.1	Polynya area	73
4.3.2	Atmospheric heat flux	74
4.3.3	Oceanic heat flux	79
4.3.4	Sea ice production	81
4.4	Chapter summary	84
5	Water mass modification on the continental shelf	87
5.1	Surface fresh water balance	87
5.2	Salinity distribution	88
5.3	Seasonal cycle of the on-shelf waters	90
5.4	High Salinity Shelf Water	94
5.4.1	HSSW volume	94
5.4.2	HSSW export	95
5.5	Deep water formation: An estimate	97
5.5.1	High Salinity Mixing Partner and formation potential	97
5.5.2	Potential formation of WSDW	99
5.5.3	Contribution by ISW formation and export	101
5.6	Chapter summary	102
6	Impact of different atmospheric forcing data sets	105
6.1	Polynya formation	105
6.2	Mean patterns	109
6.2.1	Near-surface wind	109
6.2.2	Air temperature	112
6.2.3	Sea ice concentration	112
6.2.4	Sea ice production	114
6.3	Bottom salinity and HSSW	116
6.4	Polynya events and variability	119
6.5	Quantitative overview	124
6.6	Chapter summary	127

7 Conclusions and outlook	131
8 Acknowledgements	135
List of variables and abbreviations	141
List of tables	143
List of figures	146
Bibliography	147

1 Introduction

The global circulation pattern of the oceans is dependent on high-latitude deep water formation. The density increase of water at freezing point by salinification with brine that is released in sea ice formation is the most important way to produce water masses dense enough to sink to the bottom of the world ocean and ventilate the abyss. Today, it is primarily in the context of climate change that detailed knowledge about the turnover of the world oceans and its variability is crucial. Thorough knowledge of the deep water formation process and the response period of the deep ocean is crucial to address the subjects of oceanic heat and carbon uptake and storage capacity and the consequences of ocean warming and acidification.

The densest (very cold and very saline) water masses are generated on the continental shelf and transformed by various mixing processes on their way into the deepest basins of the world ocean. Thus, on their arrival they are to some degree warmer and less saline.

Polynyas are areas in an ice-covered ocean that have no or little ice cover. In these areas, exchange processes between ocean and atmosphere are considerably more intense than in the surrounding area. Two categories of polynyas are differentiated by their driving mechanism. Open ocean polynyas (also called sensible heat polynyas) are formed by upward heat transfer by mixing or upwelling of warm water melting the sea ice or inhibiting its formation. Although no ice is formed, the ocean is cooled significantly.

Coastal polynyas (or latent heat polynyas) are mechanically opened due to wind- or current-related ice drift. Coastal polynyas are sites of strong ocean-atmosphere heat flux and high sea ice production. (The name 'latent heat polynya' refers to the latent heat released in the ice formation.) They are of great importance for bottom and deep water formation (Smith et al., 1990; Morales Maqueda et al., 2004).

This study investigates coastal polynyas and the associated processes. The term polynya in this study is used for all areas with a sea ice concentration below 70 % or sea ice thickness of less than 20 cm. This implies that in the so-called 'ice-covered' ocean locally up to 30 % of the area can be stretches of open water called leads. Leads are usually narrow but often several kilometres long features that open and close due to ice drift divergence and convergence, respectively. Even in areas of high sea ice concentration, leads typically

cover at least 1 % of the area (Smith et al., 1990). With respect to sea ice formation and ocean-atmosphere fluxes, leads act in the same way as coastal polynyas (Morales Maqueda et al., 2004). But when it comes to the modification of water properties there is a crucial difference: Leads are subject to ice drift; they constantly change location and often open and close within hours, while polynyas are fixed in space (although their size may vary) and often have a lifespan of several days, which allows for a continuous localised and thus much more effective salinification of the water.

1.1 Impact of coastal polynyas on ocean and atmosphere

Sea ice is not stationary, but – with the exception of fast ice, which is fixed in place by its connections to the shore or the ocean bottom – drifts forced by winds and currents. When offshore winds prevail, the ice is pushed away from the shoreline, leaving a narrow band of open water. With ocean temperatures at the freezing point and air temperatures below, immediate ice production sets in as heat is transferred from the ocean to the atmosphere. With no or only little ice cover the ocean-atmosphere heat flux is much higher in the polynya than in the adjacent ice covered area. Coastal polynya ice production rates therefore surpass those of the ice covered ocean by far. With this high ice production a strong enrichment of salt in the surface water is linked, since the water rejects the salt molecules when arranging into the lattice structure of the solid state. An increase of salinity of a water parcel always results in a rise of density. Given a certain spatial and temporal stability (enduring offshore winds), high ice production rates (low air temperatures) and shallow water depths (continental shelves) the situation eventually results in convective mixing and salinification of the whole water column, creating a very dense on-shelf water mass that is then led by the bottom topography and pressure gradients, leaving the continental shelf in plumes and sinking until it reaches water masses of equal density or the ocean bottom. On its way to the abyss it is gradually diluted by mixing with the surrounding waters. It loses some of its salinity and gains heat; therefore the bottom water of the world ocean is less dense than the water masses that can be found on the continental shelves.

The densification and sinking of water masses from both polar regions is an essential driving force of the global thermohaline circulation. The Antarctic contribution at atmospheric pressure is less dense than the Arctic contribution, but due to its colder temperatures its density increases faster with the pressure of the overlying waters and thus it underlies the Arctic waters at the ocean bottom. Eventually, coastal polynyas – narrow areas of a few kilometers width existing on timescales of days or weeks – influence the large-scale circulation of the world ocean. (Smith et al., 1990; Renfrew et al., 2002; Morales Maqueda et al., 2004; Barber

and Massom, 2007)

Contrary to their cooling effect in winter, coastal polynyas are focal points for the oceanic heat uptake in spring and summer (Smith et al., 1990; Ohshima et al., 1998). The open-water areas have a much lower albedo (ca. 0.1) than melting sea ice (ca. 0.7-0.8) so that the incoming solar shortwave radiation is received by the ocean with only small losses. This heat is then used to melt ice in the surrounding area, leading to an increase in open water area and initiating a positive feedback loop.

During the melting season a 'coastal polynya' technically does not exist since no ice formation takes place and the term 'polynya' only applies for areas with less than 70 % sea ice cover as long as they are not linked to the open ocean. For practical reasons the denomination 'coastal polynyas' will be used throughout the year in this study because a differentiation of when the term is applicable is not always straight forward. This study will mostly concentrate on the freezing processes in the winter season and warnings will be added whenever 'coastal polynyas' during summer are discussed.

The atmosphere is strongly influenced by polynyas on the micro- and mesoscale (Raddatz et al., 2011). In the winter season, the polar atmosphere is typically characterised by an inversion (temperatures increasing with height) and a stable boundary layer (Andreas et al., 2000; Heinemann, 2008). However, cold air moving over the warmer ocean induces large sensible and latent heat fluxes. Also, a substantial flux of moisture occurs since air flowing over a coastal polynya may arrive saturated with respect to an ice surface, but undersaturated with respect to water (Pease, 1987). With the air taking up heat and moisture over the polynya, both heat and moisture fluxes decrease with fetch since the gradients at the surface decrease (Renfrew and King, 2000; Morales Maqueda et al., 2004). Also, due to the wind driving the newly formed ice away from the shoreline, the polynya's ice cover tends to increase with fetch, which amplifies the fetch-dependent reduction of surface fluxes (Fiedler et al., 2010).

By warming and moistening, air loses density and convection is generated, entailing the formation of a convective (thermal) internal boundary layer (Renfrew and King, 2000; Heinemann, 2008; Fiedler et al., 2010; Raddatz et al., 2011), the height of which increases linearly with the natural logarithm of the fetch (Andreas and Cash, 1999). This boundary layer elevates the inversion height (Overland and Guest, 1991; Heinemann, 2008) and is characterised by cloud formation (Renfrew and King, 2000; Heinemann, 2008) which affects the local radiative heat balance (Smith et al., 1990). The presence of clouds is an obstacle for incoming solar shortwave radiation so the earth's surface receives less heat, but the longwave radiation emitted by the earth is partly absorbed and again radiated by the clouds. Thus, a fraction of the heat lost by the earth is restored by the clouds.

Furthermore, there is a biological and biogeochemical aspect to coastal polynyas.

Polynyas in general constitute a habitat for a range of biological species from mammals and birds to smaller lifeforms like algae and diatoms. In the winter months, when daylight is scarce or absent, mammals and birds are thought to leave the Antarctic continent with exception of the emperor penguin, for whom coastal polynyas provide access to the ocean (Massom et al., 1998). For mammals like whales or seals, coastal polynyas provide a possibility to breathe, enabling them to stay in ice-covered areas for prolonged time periods. Although winter surveys are scarce, rare sightings of killer whales (close to a coastal polynya off Adélie Land; Gill and Thiele, 1997) and Weddell, crabeater and leopard seals (at latitudes 73-75° S off Victoria Land; Van Dam and Kooyman, 2004) have been reported. Since coastal polynyas constitute the initial source of heat at the turn of the freezing to the melting season and widen by melting the adjacent sea ice, they are still of great influence in the spring, when algae profit from the unobstructed incidence of light in the open water areas. Species feeding on algae and every higher level of the food chain consequentially benefit from the existence of coastal polynyas.

With regard to the global carbon cycle and a possible climate change, bottom water production is an important mechanism for the oceanic uptake of carbon and other gases. But also the biogeochemical metabolism of oceanic species influences the carbon budget. In the process of changing inorganic carbon into organic carbon (carbon fixation) especially the small species of the phytoplankton are of importance. Knowledge of the physical conditions that prevail in polynyas is essential, since changes in the physical parameters of the environment can cause a change in species dominance which again can lead to a substantial change in CO₂ drawdown (Arrigo et al., 1999).

Further important studies addressing coastal polynyas around Antarctica (since the availability of satellite observations) were conducted by Zwally et al. (1985), who used brightness temperatures from passive microwave satellite observations to examine sea ice concentration around the continent, the localisation of polynyas, their driving mechanisms and consequences on sea ice production and the underlying water, and Cavalieri and Martin (1985), who investigated polynyas off Wilkes Land coast in winter 1979 with the help of passive microwave data.

Recently, studies of coastal polynyas with sea ice-ocean models have been conducted in various Antarctic regions. For the Ross Sea, Mathiot et al. (2012) performed simulations with the regional sea ice-ocean circulation model NEMO, along the coast of East Antarctica Kusahara et al. (2010) employed the sea ice-ocean model COCO, and the Mertz Glacier Polynya off the coast of Adélie Land was investigated by Kusahara et al. (2004) with a variant of MPIOM. For the Weddell Sea, model studies of coastal polynyas are so far scarce.

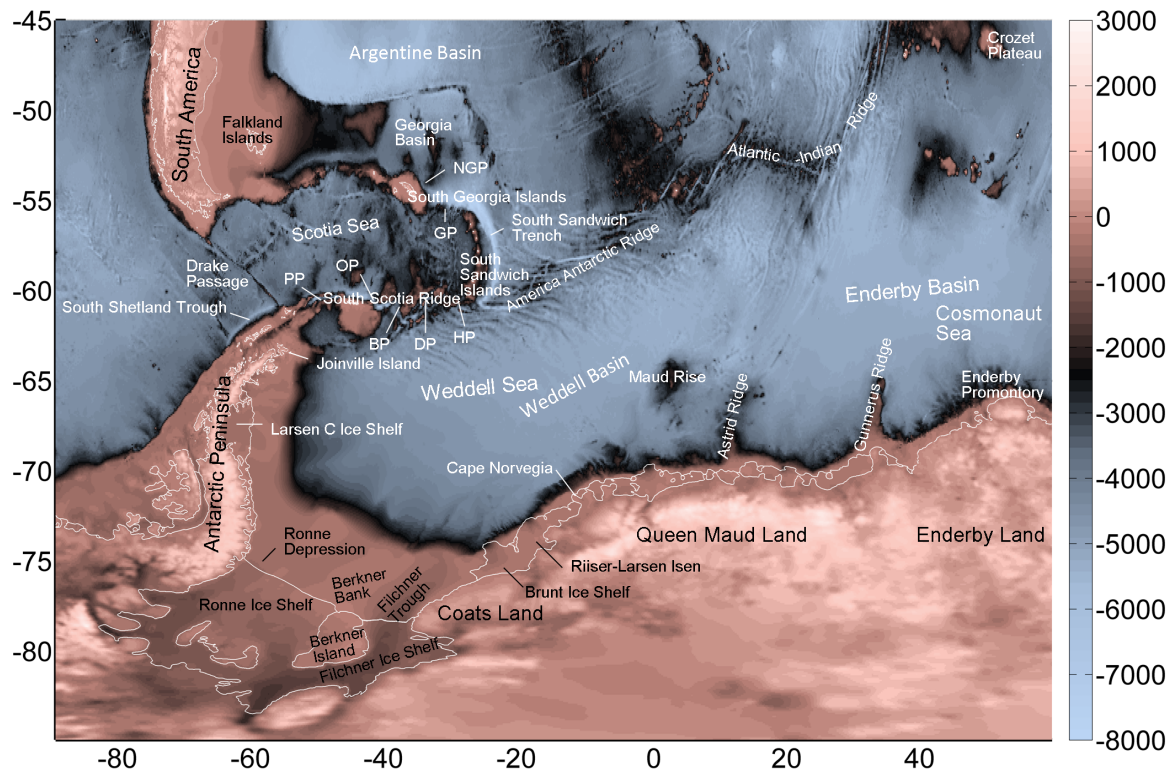


Figure 1.1: Map of the Weddell Sea. The following abbreviations are used: PP – Philip Passage, OP – Orkney Passage, BP – Bruce Passage, DP – Discovery Passage, HP – Hoyer Passage, GP – Georgia Passage, NGP – Northeast Georgia Passage

1.2 The Weddell Sea

1.2.1 Location and topography

The Southern Ocean is important for the global thermohaline circulation for two reasons. First, because it features wide areas with seasonal sea ice cover, the production of which enables deep convection via bottom water formation. Secondly, it is also the only deep connection between the great ocean basins. Only here, a latitudinal circumnavigation of the globe is possible and the west wind belt, which also is unobstructed by continents, gives rise to the world's strongest current system, the Antarctic Circumpolar Current (ACC). The ACC maintains an eastward transport of approximately 130 Sv (Nowlin Jr. et al., 1977; Whitworth III et al., 1982; Rintoul and Sokolov, 2001; Cunningham et al., 2003) ($1 \text{ Sv} = 10^6 \text{ m}^3/\text{s}$). South of the ACC, where the distance to the continent allows, we find three cyclonic subpolar gyres (Weddell Gyre, Ross Gyre and Amery Gyre; Klatt, 2002; Carter et al., 2008) and next to the Antarctic coastline the rather narrow band of the westward

coastal current.

One of the subpolar gyres is the Weddell Gyre with a transport of approximately 30-40 Sv (Fahrbach et al., 1994; Gordon et al., 2001). From the east coast of the Antarctic Peninsula it reaches to $\approx 30^\circ$ E (Deacon, 1979; Gouretski and Danilov, 1993), although Park et al. (2001) found evidence for a much wider extent reaching at least to the Enderby Land promontory (53° E). The boundary between Weddell Gyre and ACC is given by the streamline from the tip of the Antarctic Peninsula. There is evidence of a front, the Southern Boundary/Scotia Front, that is marking the boundary (Whitworth III and Nowlin Jr., 1987; Veth et al., 1997) and Orsi et al. (1995) observed a close coincidence of the Southern ACC Boundary with the hydrographic characteristic of Upper Circumpolar Deep Water (UCDW) becoming entrained in the mixed layer and south of the front it is undistinguishable from the surface waters. UCDW is found below the surface waters of the ACC. It is a water mass which is characterised by a maximum in nutrients and an oxygen minimum. The Southern ACC Boundary is varying, but remains close to a chain of submarine ridges: the South Scotia Ridge, the America Antarctic Ridge at $\approx 60^\circ$ S and at its eastern extremity the Atlantic-Indian Ridge at $\approx 53^\circ$ S.

The area of the Weddell Sea can roughly be defined as the Atlantic sector of the Southern Ocean south of the Antarctic Circumpolar Current. Its western border is provided by the Antarctic Peninsula. Neglecting the geographic definition that states Coats Land (ca. 30° W) as eastern boundary of the Weddell Sea, in the oceanographical sense the eastern boundary is found at ca. 30° E defining the whole extent of the Weddell Gyre as part of the Weddell Sea (Fahrbach and Beckmann, 2001). In the south, the Weddell Sea features an up to 500 km wide continental shelf with an average depth of ca. 500 m. The comparatively high depth of the Antarctic continental shelves is caused by the immense weight of the ice sheet burdening the continent and depressing the earth's crust to where the isostatic equilibrium with the mantle is reached. For the Weddell Sea shelf the vertical displacement amounts to 100-400 m (increasing toward the continent) (Huybrechts, 2002).

In the south, two large ice shelves adjoin the continental shelf, the Ronne Ice Shelf and the Filchner Ice Shelf, which are often collectively called Filchner-Ronne Ice Shelf (or Ronne-Filchner Ice Shelf) since they are divided at their seaward front by Berkner Island, but connected at their grounding line where they are fed by various ice streams draining the Antarctic Ice Sheet. At the grounding line the Ronne Ice Shelf reaches depths of 800-1000 m, while at its front the average depth is 250 m. The Filchner Ice Shelf, however, retains a thickness of ≈ 500 m at its front. Beneath the Filchner Ice Shelf is the deep Filchner Trough. It has a depth of 1230 m at the Filchner Ice Front and continues north until meeting the continental shelf break with a sill depth of 610 m and south under the ice steadily gaining depth and

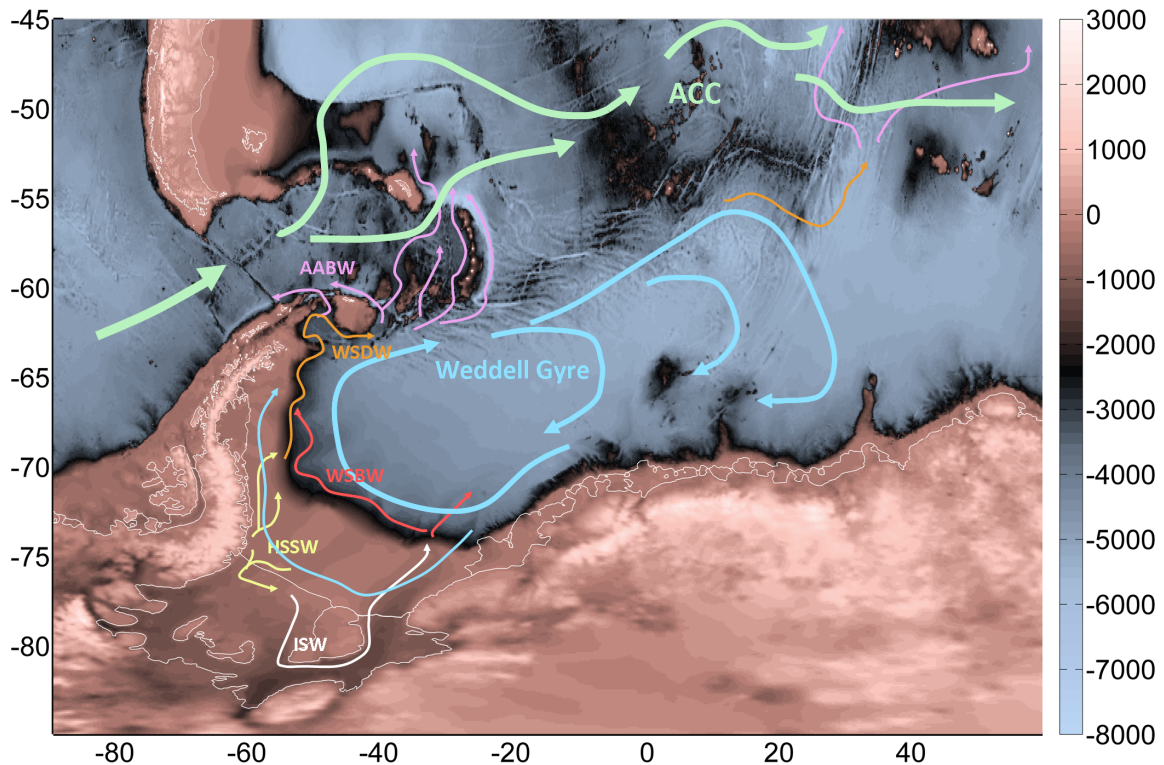


Figure 1.2: Pathways of the Weddell Sea waters. Simplified flow patterns of the ACC, the Weddell Gyre and the water masses HSSW, ISW, WSDW and WSBW.

reaching 1800 m at the deepest point of the grounding line. Under the front of Ronne Ice Shelf on the western side we also find a depression, the Ronne Depression, that under the ice shelf reaches depths of 1300 m but at the ice shelf front is only 610 m deep and flattens to a shallow 537 m toward the continental shelf break. (RTopo-1; Timmermann et al., 2010)

The deep basin of the Weddell Sea reaches depths of more than 5000 m. However, the western part, called Weddell Basin, is shallower than the eastern part, called Enderby Basin (depth within the Weddell Basin increases from west to east). Since the boundary between Weddell Basin and Enderby Basin is topographically open, both are often collectively called Weddell-Enderby Basin. The main topographical features are Maud Rise at 3° E, a sea mount that reaches up to 1600 m beneath the sea surface, Astrid Ridge at 11° E, a ridge extending ca. 250 km from the continent into the basin with water depths of ≈ 2000 m, and Gunnerus Ridge to the east of the Weddell Gyre at 33° E, a ridge of only 1200 m depth connecting the continent with a sea mount that reaches 850 m beneath the sea surface. (RTopo-1; Timmermann et al., 2010)

The basin of the Weddell Sea has several connections to the world ocean that allow for the

export of deep water (Figure 1.1):

- A number of deep outlets through the South Scotia Ridge into the Scotia Sea (Gordon, 1966; Nowlin Jr. and Zenk, 1988; Locarnini et al., 1993), namely Philip Passage (47° W, ca. 2000 m), Orkney Passage (40° W, 3800 m), Bruce Passage (38° W, 2900 m), Discovery Passage (33° W, 2800 m), and Hoyer Passage (30° W, 2600 m), allow the Weddell Sea Deep Water (WSDW) to enter the Scotia Sea. From there, some of the water flows to the west and into the southern Drake Passage filling the South Shetland Trough (Figure 1.1), but seems to spread no farther from there (Sievers and Nowlin Jr., 1984), but to get incorporated into the ACC by upwelling (Schodlok et al., 2002). However, the bulk of WSDW entering Scotia Sea flows to the northeast and through Georgia Passage and Northeast Georgia Passage into the western Georgia Sea (Naveira Garabato et al., 2002a) from where it spreads north into the Argentine Basin.
- The South Sandwich Trench, which with depths below 7000 m (8264 m at the deepest point) allows WSDW to spread into the Argentine Basin or the western Georgia Basin (Naveira Garabato et al., 2002a), but the passage of Weddell Sea Bottom Water (WSBW) is blocked by the hydrographic barrier of the ACC (Locarnini et al., 1993). It is constrained to the circulation of the Weddell Gyre (Orsi et al., 1993).
- Deep passages through the Southwest Indian Ridge, which continues northeast from the Atlantic-Indian Ridge, allow WSDW to escape into the basins around the southern tip of Africa (Agulhas Basin, Cape Basin, Natal Basin and Mozambique Basin) where it is trapped by topography, however, and can not spread farther.
- In the eastern part of the Enderby Basin the Crozet-Kerguelen Gap provides a deep passage and lets the deep water from the Weddell Sea escape northward into the Crozet Basin from where it moves further northward into the Madagascar Basin of the Indian Ocean (Haine et al., 1998).

1.2.2 Weddell Sea water masses and bottom water formation

Antarctic Bottom Water (AABW) is the water mass with the highest in-situ density found in the open oceans filling the abyssal plains from the south. It originates from the Southern Ocean from where it spreads north through the deep passages described in the section before. It is colder than the deep water formed in the northern hemisphere and profits from the thermobaric effect such that it underlies northern water masses, although at surface pressure, its density is less than the density of the saline northern deep water. AABW covers the ocean

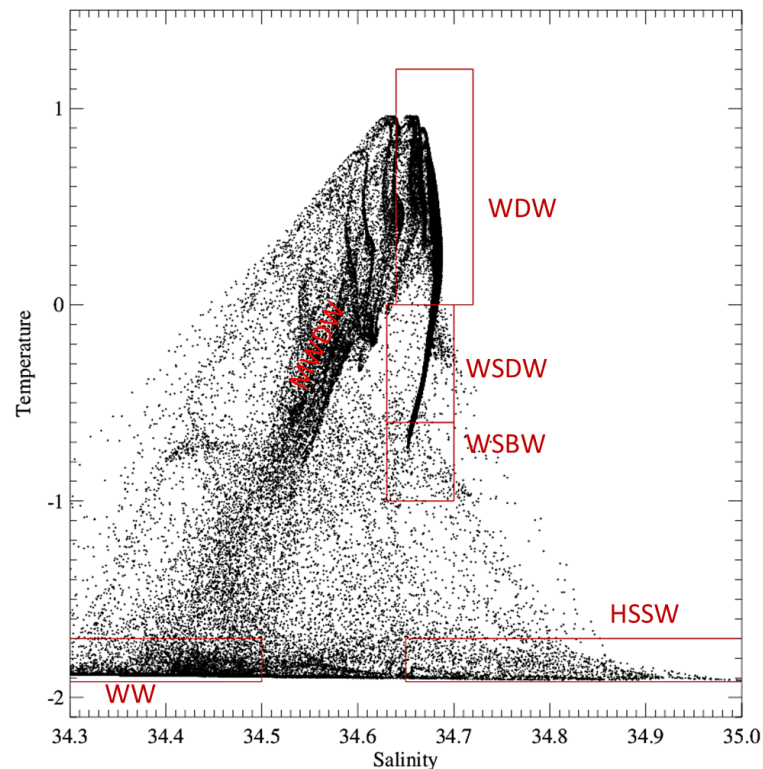


Figure 1.3: TS-diagram showing the water masses of the Weddell Sea.

bottom in the Indian and Pacific basins and in the western Atlantic Ocean spreads as far north as 40° N.

The Weddell Sea is considered an important source region of Antarctic Bottom Water (Deacon, 1937). Foldvik and Gammelsrød (1988) estimate that the Weddell Sea is the source region to 80 % of AABW, Orsi and Bullister (1999) considers the Weddell Sea as the major source region of AABW, naming the Ross Sea as the second main contributor. Newer studies demonstrate that also other regions can have a substantial share in deep water formation if their geometry supports recurring polynyas, e. g. the Mertz Glacier Polynya (Rintoul, 1998; Williams and Bindoff, 2003). The Adélie Land Bottom Water was suggested to be three times the volume of deep water originating from the Ross Sea by Bindoff et al. (2001) and Tamura et al. (2008) found Cape Darnley Polynya west of the Amery Ice Shelf to be a potential source region of AABW.

The circulation of the Weddell Sea is dominated by the cyclonic flow of the Weddell Gyre (Figure 1.2). On its eastern end, Lower Circumpolar Deep Water (LCDW) from the ACC is entrained and within the Weddell Gyre it is called Warm Deep Water (WDW). With $T > 0^\circ\text{C}$ and $34.64 < S < 34.72$ (Foster and Carmack, 1976), it constitutes the warmest

water mass in the Weddell Sea. It is generally found at depths between 150 m and 1500 m (Fahrbach et al., 2004). Below the WDW we find Weddell Sea Deep Water (WSDW) with $-0.6^{\circ}\text{C} < T < 0^{\circ}\text{C}$ and $34.63 < S < 34.7$. Underlying WSDW is Weddell Sea Bottom Water (WSBW). It has a higher density than WSDW due to its lower temperatures ($T < -0.6^{\circ}\text{C}$; Foster and Carmack, 1976) but the transition is gradual and the threshold value is defined by the possibility to escape the circulation of the Weddell Sea through the gaps in South Scotia Ridge. Thus, most of the Weddell Sea-originated AABW derives from WSDW and not from WSBW.

At the surface the waters are subject to atmospheric influences. While in winter they are usually kept at freezing point and the salinity increases with time because of ice formation, in the summer season ice melt reduces their salinity and where the ice cover is removed, water temperatures can rise. These highly variable waters are commonly referred to as surface waters. In the western Weddell Sea usually a substantial volume of sea ice survives the summer season, thus the surface waters are largely kept at freezing point.

The southern limb of the Weddell Gyre brings the water in contact with the coastline. East from the 25° W meridian, the continental shelves of the Weddell Sea are narrow and mostly covered by ice shelves. Thus, WDW entering upon the continental shelf can easily reach the ice shelves and induce melting, which reduces the salinity of the water (Fahrbach et al., 1994). Also, polynyas formed at the ice shelf edges are positioned close to the shelf break or even over the deep ocean so that an increase in salinity caused by ice formation leads to a convective process rendering the salt gain insignificant to a water column of several 1000 m. These two factors prevent the ice formation in the polynyas from leading to dense water formation here. The water that stems from these processes is called Eastern Shelf Water (ESW) and is mostly found on the continental shelves east of the Filchner Trough (Carmack and Foster, 1975a). In the southwestern Weddell Sea, however, the continental shelves are wide and WDW entering upon them is modified by mixing with Winter Water (WW), which has temperatures close to the freezing point T_f and salinities between 34.3 and 34.5 (Foster and Carmack, 1976), to form Modified Warm Deep Water (MWDW) with temperatures and salinities in a range between those of WDW and WW according to the mixing ratio. As the name suggests, WW is formed during winter. It has experienced cooling by the atmosphere and moderate salinification by freezing processes.

On the wide shelves of the southwestern Weddell Sea current velocities typically amount to 5-10 cm/s (Fahrbach et al., 1992; Kottmeier and Sellmann, 1996; Markus et al., 1998; Foldvik et al., 2001) and the mean water column thickness is ca. 500 m. The water reaching the ice shelf fronts has already lost most of its heat and is close to freezing temperatures. Polynya formation here enables exceptionally high sea ice formation rates because most of

the heat transferred to the atmosphere has to be gained by ice formation and the brine-release rapidly increases the salinity of the entire water column. Thus a very dense water mass, the High Salinity Shelf Water (HSSW) ($T \approx T_f, S > 34.65$; Grosfeld et al., 2001) is produced.

Due to its density, HSSW spreads downslope on the ocean floor steered by topography. To some extent it enters into the ice shelf cavities where it is transformed into Ice Shelf Water (ISW). When it enters the cavity, the water has a potential temperature close to the surface freezing point of sea water but with the ice shelf thickening, the in-situ freezing point for water at its bottom drops due to the increasing pressure and will become even lower than the in-situ temperature of HSSW. Hence the HSSW melts the glacial ice and freshens and cools in the process. The newly formed ISW ($T < T_f$; Grosfeld et al., 2001) is less dense than HSSW and rises. Thus, the pressure decreases and it can reach a depth where the in-situ temperature of the water equals its in-situ freezing point and the formation of marine ice at the bottom of the ice shelf occurs. Evidence of the formation of marine ice was found under Filchner Ice Shelf east of Berkner Island (Foldvik and Gammelsrød, 1988) and several large areas of Ronne Ice Shelf (Lambrecht et al., 2007).

Three different pathways for the formation of WSDW / WSBW are known:

- HSSW that does not enter the ice shelf cavity spreads on the continental shelf until it reaches the shelf break, where it is mixed with MWDW and descends the continental slope as WSDW / WSBW. This formation path was described by Foster and Carmack (1976) and has therefore often been referred to as the Foster-Carmack Process.
- ISW leaving the cavity of Filchner Ice Shelf fills the Filchner Trough to the sill depth of 610 m. The overflow mixes directly with WDW and also descends the continental slope as WSDW / WSBW. This process was described by Foldvik et al. (1985a) and has been called Foldvik Process or ISW Process.
- Gordon (1978) suggests a further process for bottom water formation in the Weddell Sea. Due to the upwelling in the center of the Weddell Gyre, the stability there is low and might collapse thus allowing for deep convection. Based on a simple model Martinson et al. (1981) finds the contribution of this process to exceed 1 Sv. However, these studies were conducted under the impression of the Weddell Polynya of the early 1970s. The process is probably linked to the formation of a sensible heat polynya like the Weddell Polynya and only of significance in years with such a polynya (Mensch et al., 1996), which is not the case in the period investigated in this study.

1.3 Coastal polynyas in the Weddell Sea

In the southwestern Weddell Sea, the wide continental shelves meet the topographic requirement for dense shelf water formation, the high latitude provides low winter air temperatures, and frequent offshore winds generate high coastal polynya activity. This makes the Weddell Sea an ideal place for deep and bottom water formation.

The formation of deep and bottom water in the Weddell Sea starts with the strong ocean-atmosphere heat flux in autumn and winter. The water on the shelves slowly flows westward and is rapidly cooled to the freezing point. Then ice formation sets in to maintain the heat flux. Now the salinification of the water begins and while slowly flowing westward along the ice shelf edge salt is accumulated more and more during the freezing season. When a coastal polynya opens due to the offshore (partly katabatic) winds this slow process is accelerated considerably and eventually the salinity-enhanced water is pushed over the threshold value for HSSW.

Not all of the HSSW that is formed at the Ronne Ice Shelf Front will leave the continental shelf at a location to the north of its origin, but a part of it follows the bottom slope and flows under the ice shelf. There it turns east due to the influence of the Coriolis force until it encounters the barrier of Berkner Island (Figure 1.2). It then is steered around the island in anti-clockwise direction, probably by contours of equal water column thickness eventually emerging from the ice shelf on the western side of the Filchner Trough (Foldvik and Gammelsrød, 1988; Jenkins et al., 2004). While under the ice shelf, the water mass is modified (see Section 1.2.2). In the Ronne Depression ISW occurs only in summer but probably does not leave the basin and recirculates again under the iceshelf (Nicholls et al., 2003). Only in the Filchner Trough ISW can escape from the shelf and is involved in deep water formation. Foldvik et al. (2004) estimated the outflow of ISW to be 1.6 Sv.

Several studies have addressed coastal polynyas in the Weddell Sea. Among the most important and the most recent are the following:

- Kottmeier and Engelbart (1992) studied the ice motion and polynya formation at the coast of the eastern Weddell Sea based on observations and a free ice drift model. They concluded the polynyas to be primarily wind-driven and to open if the offshore angle is at least 30° for northeasterly winds, while southwesterly winds can create polynyas even though they have a slight onshore component due to the Coriolis force acting to the left in the southern hemisphere. They found the heat flux to be fetch-dependent since the air is warmed over the polynya and time-dependent due to new ice formation.
- Comiso and Gordon (1998) correlated the annual ice extent and polynya area in the

Weddell Sea (ice concentration obtained from SSMR and SSM/I data using a Bootstrap technique; Comiso, 1995) with air temperature and wind in the Atlantic sector (60° W- 20° E). They found large interannual variations and good correlations between polynya area and meridional wind as well as between polynya area and ice extent (especially east of Filchner Ice Shelf) and deduced that coastal polynyas are important in sea ice production and thus the production of dense water (provided a large enough shelf area).

- Markus et al. (1998) investigated the coastal polynyas of the Weddell Sea deriving polynya area from SSM/I passive microwave data using an algorithm developed by Markus and Burns (1995). The application of a basic thermodynamic model forced with ECMWF 2m-temperatures and 10m-wind speeds allowed them to calculate sea ice production. For May-October 1992-1994 they found mean polynya areas of 3800 km^2 in front of the Ronne and Filchner Ice Shelves in the south and 4700 km^2 along the Antarctic Peninsula coastline in the west. The seasonal sea ice production in the polynyas of the southern region was determined as 87 km^3 ; 37 km^3 were found in the western polynyas along the peninsula.
- Focusing on the Ronne polynya, Renfrew et al. (2002) established a surface energy budget and derived ice production also based on polynya area derived from SSM/I data using the algorithm of Markus and Burns (1995) and meteorological information from automated weather stations and the NCEP/NCAR Reanalysis. They found the upward atmospheric heat flux over the polynya to be ranging from minimum values of -350 W/m^2 in summer to maxima of $> 1100 \text{ W/m}^2$ in winter and to be subject to a strong interannual variability. A mean ice production of 24 m or $1.11 \cdot 10^{11} \text{ m}^3$ within a freezing period was calculated for the coastal polynya but, again, found to be subject to high interannual variability. Renfrew et al. (2002) found the interannual variability of the total ice production of the Weddell Sea to be very small and essentially determined by the variability of the coastal polynyas.
- Tamura et al. (2008) calculated sea ice production for all large Antarctic polynyas, including the Ronne polynya, using thin ice thickness data derived from polarisation ratios of brightness temperatures of SSM/I data and AVHRR data with a new algorithm presented by Tamura et al. (2007). They used ECMWF Reanalysis and NCEP/NCAR Reanalysis 2 data to perform a heat budget analysis (Nihashi and Ohshima, 2001) under the assumption that all transferred heat was gained by ice formation. For the period March-October 1992-2005 Tamura et al. (2008) found a mean annual sea ice production of 85 km^3 in Ronne polynya but allowed that this might be an underestimation

since the method has difficulties to detect very narrow polynyas.

- Drucker et al. (2011) investigated the polynya sea ice production in the Weddell and Ross Seas calculated from ECMWF atmospheric temperatures and geostrophic winds, and the polynya ice thickness, which they derived from SSM/I and AMSR-E brightness temperature ratios. Within the Weddell Sea they identified three main contributing regions: the Eastern Weddell Polynya next to Brunt Ice Shelf, the coastal polynya in front of Ronne Ice Shelf and the polynya around the stationary iceberg A23. With a maximum production rate of 15 m/yr for both, the Eastern Weddell Polynya features a mean sea ice production of 112 km³/season and the Ronne polynya gives 99 km³/season. Including the contribution of the polynyas around A23, the ice production of the polynyas in the southwestern Weddell Sea is found to be 241 km³/season. In their calculation Drucker et al. (2011) used data from 1 April-30 October 2003-2008. They considered only polynya contributions where the water column was no deeper than 1000 m and limited their consideration to the area south of 70.5° S.

The aims of this thesis are to quantify the share the coastal polynyas have in the winter heat budget and ice production of the southwestern Weddell Sea (Chapter 4), and to investigate the effect on the waters on the continental shelf (Chapter 5) using the Finite Element Sea Ice-Ocean Model described in Chapter 2. The validity of the model results is assessed in Chapter 3 and their robustness against the atmospheric forcing data is investigated in Chapter 6. In Chapter 7 the findings are summed up and lastly a short outlook on further interesting work related to the topic is given.

2 Model description

In order to investigate coastal polynyas in the southwestern Weddell Sea and their influence on sea ice production and water mass modification the Finite Element Sea ice-Ocean Model (FESOM), a general ocean circulation model including a sea-ice component, is used. In this chapter, first the Finite Element Method (FEM) is explained, then the model components, their mode of communication as well as the chosen set-up and the atmospheric data sets used for the surface forcing are presented.

2.1 The Finite Element Method (FEM)

The Finite Element Method (FEM) is the method of choice to solve complex numerical problems with intricate geometries. It allows for the use of unstructured grids, which makes resolution highly adjustable. When modelling the ocean with its complex geometry of coastline and bathymetry, this is of great advantage, because narrow straits that are often decisive for circulation patterns require high resolution, while computing time can still be minimised by coarser resolution in the large ocean basins.

Like all numerical methods to solve a system of partial differential equations the FEM discretizes the continuous volume. As the name implies, the FEM splits the geometry into an arbitrary amount of elements. In the two-dimensional case these usually are triangles, in the three-dimensional case tetrahedrons or prisms. These elements are called finite, signifying that any numerical solution would only be an approximation of the exact solution, since only the use of infinitely small elements (exactly reproducing the continuous volume) would render the exact solution. The accuracy of the solution improves with higher resolution but also the computing time increases. Both quantities should be in a balance that permits informative results within an acceptable time span. The essential advantage of the FEM is the possibility to enhance resolution well-directed in selected areas that are crucial for the studied processes, contrary to the Finite Differences Method, where a structured grid is required.

The solution of the partial differential equation is attained by the introduction of basis functions. Often, these are linear functions but higher order functions can improve the solu-

tion. However, higher order polynomials require additional nodes and are connected with increased computational effort. The specifications for the basis functions are continuity and piecewise differentiability. They are chosen to equal 1 at their assigned grid point and 0 at every other grid point.

The grid used in this study for calculations with FESOM is based on an unstructured triangular surface grid. The three-dimensional partitioning into tetrahedrons takes place by introducing horizontal depth levels (z -coordinates). The number of levels and the assigned depth of the levels can be chosen arbitrarily and according to the problem at hand. By vertical projection of the surface grid onto the underlying levels, prisms are produced, which then are each split into three tetrahedrons. Every tetrahedron constitutes a finite element for which the prognostic variables are calculated with linear basis functions.

2.2 The Finite Element Sea ice-Ocean Model FESOM

The Finite Element Sea-ice Ocean Model FESOM is a fully-coupled combination of a finite-element physical ocean circulation model, the Finite Element Ocean Model FEOM, and a dynamic-thermodynamic sea-ice component, the Finite Element Sea-Ice Model FESIM. FESOM was developed at Alfred Wegener Institute and has been described by Timmermann et al. (2009) in an earlier version.

2.2.1 The ocean component: FEOM

FEOM is a hydrostatic ocean circulation model that solves the primitive equations in a spherical geometry. It is based on the Finite Element model of the North Atlantic (FENA) described by Danilov et al. (2004). For the parameterisation of subgrid-scale processes the model makes use of a Pacanowski-Philander type vertical mixing scheme (Pacanowski and Philander, 1981), which is combined with additional vertical mixing over a depth dependent on the Monin-Obukhov length as proposed by Timmermann and Beckmann (2004). The dedicated equation of state as proposed by Jackett and McDougall (1995) facilitates the calculation of in-situ density as a function of potential temperature. Temperature, salinity, horizontal velocities and surface elevation are represented by continuous, linear functions. The model temperature is always the potential temperature.

Main equations

The model solves the momentum evolution equation

$$\frac{\partial \vec{u}_h}{\partial t} + f \left(\vec{k}_v \times \vec{u}_h \right) + g \nabla_h H_S - \nabla_h \cdot A_h \nabla_h \vec{u}_h - \frac{\partial}{\partial z} A_v \frac{\partial \vec{u}_h}{\partial z} = -\frac{1}{\rho_0} \nabla_h p - \vec{F}_u \quad (2.1)$$

with the horizontal velocity vector $\vec{u}_h = (u, v)$, the latitude-dependent Coriolis parameter f , the vertical unit vector \vec{k}_v , the gravitational acceleration g , the horizontal Nabla operator $\nabla_h = \left(\frac{\partial}{\partial x}, \frac{\partial}{\partial y} \right)$, the sea surface elevation H_S , the horizontal and vertical momentum diffusion coefficients A_h and A_v , respectively, the mean sea water density ρ_0 , the deviations from which are denominated by ρ , the baroclinic pressure anomaly p computed with the atmospheric pressure p_a by

$$p = p_a + \int_z^0 g \rho dz = 0 \quad (2.2)$$

and the non-linear advection $\vec{F}_u = (\vec{u}_h \nabla_h + w \frac{\partial}{\partial z}) \vec{u}_h$ under the integral continuity constraint

$$\frac{\partial H_S}{\partial t} + \nabla_h \cdot \int_{-H}^{H_S} \vec{u}_h dz = 0 \quad (2.3)$$

The vertical velocity is calculated from the horizontal velocities using the continuity equation which under the hydrostatic and the Boussinesq approximation reads

$$\frac{\partial u}{\partial x} + \frac{\partial v}{\partial y} + \frac{\partial w}{\partial z} = 0 \quad (2.4)$$

describing the ocean as an incompressible fluid conserving volume rather than mass.

Potential temperature T and salinity S are calculated from the tracer evolution equations

$$\frac{\partial T}{\partial t} + \nabla \cdot (\vec{u}T) = \nabla_h \cdot K_h^T \nabla_h T + \frac{\partial}{\partial z} K_v^T \frac{\partial T}{\partial z} \quad (2.5)$$

and

$$\frac{\partial S}{\partial t} + \nabla \cdot (\vec{u}S) = \nabla_h \cdot K_h^S \nabla_h S + \frac{\partial}{\partial z} K_v^S \frac{\partial S}{\partial z} \quad (2.6)$$

with the horizontal and vertical diffusion coefficients K_h and K_v , respectively, for each of the water mass properties.

2.2.2 The sea ice component: FESIM

FESIM is a dynamic-thermodynamic sea ice model using the Parkinson and Washington (1979) thermodynamics and an elastic-viscous-plastic rheology as described by Hunke and

Dukowicz (1997) and Hunke and Lipscomb (2010). The model includes a snow layer the presence of which affects sea ice growth and melting considerably (Owens and Lemke, 1997). Snow redistribution by winds is not considered, but the transformation of snow to ice by flooding with sea water is accounted for (Leppäranta, 1983; Fischer, 1995). Heat storage within ice or snow is not considered. Instead, linear temperature profiles are assumed in both layers applying the zero-layer approach of Semtner Jr. (1976). Prognostic variables are the mean ice thickness (ice volume per unit area) h_i , mean snow thickness (snow volume per unit area) h_s , ice concentration A , and ice drift velocity \vec{u}_i . Snow and sea ice thickness are both assumed evenly distributed over the ice covered part of each 2D element. They can change by melting and freezing processes and by converging sea ice drift. The ice drift is influenced by wind stress, ocean surface velocity, sea surface slope and internal forces of the ice that are dependent on ice thickness and concentration (see Equation 2.15).

Main equations

The sea ice model FESIM first calculates thermodynamic sea ice growth, then solves the momentum balance to determine the sea ice velocity, which eventually defines the ice thickness growth by deformation. The surface energy budget is calculated following Parkinson and Washington (1979). The heat flux to the atmosphere Q_a is split into its components: The radiative heat flux is a combination of the shortwave radiative heat flux Q_{sw} and the longwave radiative heat flux Q_{lw} ; the turbulent heat flux consists of sensible heat flux Q_s and latent heat flux Q_l :

$$Q_a = Q_{sw} + Q_{lw} + Q_s + Q_l \quad (2.7)$$

All heat flux components are calculated as net upward heat fluxes (i.e. upward flux minus downward flux), so that heat loss to the atmosphere is positive.

The downward shortwave radiation depends on angular zenith distance of the sun ζ and inhibition by relative cloud cover C ; part of it is reflected at the surface depending on its albedo α , so that

$$Q_{sw} = (\alpha - 1) \cdot \frac{\mathcal{S}_0 \cos^2 \zeta \cdot C}{(\cos \zeta + 2.7) \cdot e_{v,a} \cdot 10^{-5} + 1.085 \cdot \cos \zeta + 0.1}, \quad (2.8)$$

an empirical equation following Zillman (1972), with the solar constant \mathcal{S}_0 , the cloud factor $C = 1 - 0.6 \cdot C^3$ (Laevastu, 1960) and the vapor pressure in the air $e_{v,a}$ in Pa. In the winter months at high latitudes, the shortwave radiation, if at all, is a very small contribution to the atmospheric heat flux.

The longwave radiative heat flux is a function of the 2-m air temperature T_a , the surface temperature T_s (both in K) and relative cloud cover:

$$Q_{lw} = \epsilon_s \sigma_B T_s^4 - \epsilon_a \sigma_B T_a^4 \quad (2.9)$$

with the emissivities of the ice/ocean surface $\epsilon_s = 0.97$ and of the atmosphere $\epsilon_a = 0.765 + 0.22 \cdot C^3$ (König-Langlo and Augstein, 1994) and the Stefan-Boltzmann constant σ_B .

The sensible heat flux is determined by the ocean-atmosphere temperature difference and the 10-m wind speed u_{10} following

$$Q_s = c_p \rho_a C_s u_{10} \cdot (T_s - T_a) \quad (2.10)$$

with the specific heat of air c_p , the density of air ρ_a , the heat transfer coefficient for sensible heat $C_s = 1.75 \cdot 10^{-3}$ over ice, snow and water (Maykut, 1977; Parkinson and Washington, 1979), and the surface temperature T_s . For open water, T_s is the temperature of the ocean model surface layer, for ice it is obtained as part of the diagnostic computation of the sea ice surface energy budget.

The latent heat flux is the heat flux linked with evaporation, sublimation and their reversed processes. While the mass flux associated with evaporation is determined by the forcing data, the latent heat flux is re-calculated using wind speed and the difference between specific humidity at the surface q_s (where saturation is assumed) and at 2 m height q_a :

$$Q_l = L_e \rho_a C_l u_{10} \cdot (q_s - q_a) \quad (2.11)$$

with the heat of evaporation L_e , the density of air ρ_a and the heat transfer coefficient for latent heat $C_l = 1.75 \cdot 10^{-3}$ over ice, snow and water (Maykut, 1977; Parkinson and Washington, 1979). Thus, we obtain a self-consistent energy budget while at the same time precipitation P and evaporation E are based on one data set, providing a good estimate for net precipitation $P - E$, which is important for the ocean surface freshwater budget in this global model.

All heat flux components are calculated separately for the ice-covered and the ice-free part of each element and weighted with A and $(1-A)$, respectively.

Thermodynamic sea ice growth rate D_{h_i} , snow layer growth rate D_{h_s} and sea ice concentration change D_A are calculated from the local temporal change and the advection terms as follows

$$D_{h_i} = \frac{\partial h_i}{\partial t} + \nabla \cdot (\vec{u}_i h_i) , \quad (2.12)$$

$$D_{h_s} = \frac{\partial h_s}{\partial t} + \nabla \cdot (\vec{u}_i h_s) , \quad (2.13)$$

$$D_A = \frac{\partial A}{\partial t} + \nabla \cdot (\vec{u}_i A) \quad (2.14)$$

with the condition that $0 \leq A \leq 1$. The ice (and snow) drift velocity \vec{u}_i is determined by the momentum balance

$$m \left(\frac{\partial}{\partial t} + f(\vec{k}_v \times) \right) \vec{u}_i = A(\vec{\tau}_{ai} + \vec{\tau}_{io}) + \vec{F} - mg \nabla H_S \quad (2.15)$$

with the mass of ice plus snow per unit area m , the Coriolis parameter f , the vertical unit vector \vec{k}_v , the wind stress $\vec{\tau}_{ai}$, the ice/ocean stress $\vec{\tau}_{io}$, the gravitational acceleration g and sea surface elevation H_S . The term $\vec{F} = \nabla \cdot \boldsymbol{\sigma}$ accounts for the effect of internal stresses. The internal stress tensor $\boldsymbol{\sigma}$ is construed according to the chosen rheology (Hunke and Lipscomb, 2010) such that the relation between stress $\boldsymbol{\sigma}$ and strain $\boldsymbol{\epsilon}$ is described by the following equations for the divergence D_D , the horizontal tension and shearing strain rates D_T and D_S , respectively:

$$D_D = \dot{\epsilon}_{11} + \dot{\epsilon}_{22} = \frac{1}{\mathcal{E}} \frac{\partial \sigma_1}{\partial t} + \frac{\partial \sigma_1}{2\zeta} + \frac{P_i}{2\zeta} \quad (2.16)$$

$$D_T = \dot{\epsilon}_{11} - \dot{\epsilon}_{22} = \frac{1}{\mathcal{E}} \frac{\partial \sigma_2}{\partial t} + \frac{\partial \sigma_2}{2\eta} \quad (2.17)$$

$$\frac{1}{2} D_S = 2 \dot{\epsilon}_{12} = \frac{1}{\mathcal{E}} \frac{\partial \sigma_{12}}{\partial t} + \frac{\partial \sigma_{12}}{2\eta} \quad (2.18)$$

where $\sigma_1 = \sigma_{11} + \sigma_{22}$ and $\sigma_2 = \sigma_{11} - \sigma_{22}$, with Young's modulus \mathcal{E} , the ice strength P_i

$$P_i = P^* h_i e^{-c^*(1-A)} \quad (2.19)$$

with the two empirical factors $P^* = 20000$ N/m and $c^* = 20$, and the strain rate components

$$\dot{\epsilon}_{ij} = \frac{1}{2} \left(\frac{\partial u_i}{\partial x_j} + \frac{\partial u_j}{\partial x_i} \right) , \quad (2.20)$$

the bulk viscosity ζ

$$\zeta = \frac{P_i}{2\Delta} \quad (2.21)$$

and the shear viscosity η

$$\eta = \frac{P_i}{2\Delta e^2}, \quad (2.22)$$

where

$$\Delta = \sqrt{D_D^2 + \frac{1}{e^2}(D_T^2 + D_S^2)}, \quad (2.23)$$

with the axis ratio e of the elliptical yield curve.

The ice / ocean stress is calculated by

$$\vec{\tau}_{io} = \rho_0 c_{d,io} (\vec{u}_i - \vec{u}_o) |\vec{u}_i - \vec{u}_o| \quad (2.24)$$

with the ice-ocean drag coefficient $c_{d,io} = 3 \cdot 10^{-3}$ and the ocean surface velocity \vec{u}_o and the atmosphere / ice stress is given by

$$\vec{\tau}_{ai} = \rho_a c_{d,ai} (\vec{u}_a - \vec{u}_i) |\vec{u}_a - \vec{u}_i| \quad (2.25)$$

with the atmosphere-ice drag coefficient $c_{d,ai} = 1.5 \cdot 10^{-3}$ and the wind velocity \vec{u}_a .

2.2.3 The coupling of FEOM and FESIM

FEOM and FESIM use the same surface grid and time-stepping. This makes communication between the two model components easy since no interpolation or other treatment of results from either side is necessary. Heat flux Q_o , salt flux \mathcal{F}^S and momentum flux, represented by the ocean surface stress $\vec{\tau}_o$, are transferred between FESIM and FEOM after each timestep.

The salinity flux is given as a combination of the salt flux from thermodynamic ice growth (including snow melt) \mathcal{F}_{io}^S , the fresh water flux from ocean / atmosphere interaction over open water \mathcal{F}_{ow}^S (including rain running off the ice floes) and the salt flux effect of the possible snow-to-ice conversion by flooding \mathcal{F}_{fl}^S

$$\mathcal{F}^S = \mathcal{F}_{io}^S + \mathcal{F}_{ow}^S + \mathcal{F}_{fl}^S \quad (2.26)$$

where

$$\mathcal{F}_{io}^S = (S_o^* - S_i^*) \frac{\rho_i^*}{\rho_o^*} \left(\frac{\partial h_i}{\partial t} \right)_{th} + S_o^* \frac{\rho_s^*}{\rho_o^*} \left(\frac{\partial h_s}{\partial t} \right)_{th}, \quad (2.27)$$

$$\mathcal{F}_{ow}^S = S_o^* \cdot \begin{cases} P - E & \text{if } T_a \geq 0^\circ\text{C} \\ (1 - A) \cdot (P - E) & \text{if } T_a < 0^\circ\text{C} \end{cases} \quad (2.28)$$

and

$$\mathcal{F}_{fl}^S = S_i^* \frac{\rho_i^*}{\rho_o^*} \left(\frac{\partial h_i}{\partial t} \right)_{fl} \quad (2.29)$$

with an assumed constant ocean surface salinity $S_o^* = 34.7$, and the corresponding surface water density $\rho_o^* = 1027 \text{ kg/m}^3$, an assumed constant salinity of the sea ice $S_i^* = 4$ and the assumed constant densities of sea ice $\rho_i^* = 910 \text{ kg/m}^3$ and snow $\rho_s^* = 290 \text{ kg/m}^3$.

The momentum flux

$$\vec{\tau}_o = A \cdot \vec{\tau}_{io} + (1 - A) \cdot \vec{\tau}_{ao} \quad (2.30)$$

is calculated from the atmosphere/ocean momentum flux $\vec{\tau}_{ao} = \rho_a c_{d,ao} \vec{u}_{10} \cdot |\vec{u}_{10}|$ with the atmosphere-ocean drag coefficient $c_{d,ao} = 1.0 \cdot 10^{-3}$, the 10-m wind velocity \vec{u}_{10} and the ice/ocean momentum flux $\vec{\tau}_{io}$ as given in Equation 2.24.

The heat flux Q_o is calculated as

$$Q_o = A \cdot Q_{io} + (1 - A) \cdot Q_{ow} \quad (2.31)$$

where the ice/ocean heat flux Q_{io} is given by

$$Q_{io} = \rho_o c_{p,o} c_{h,io} u_* (T_o - T_f) \quad (2.32)$$

with the friction velocity $u_* = \sqrt{c_{d,io}} |\vec{u}_i - \vec{u}_o|$, the specific heat of water at constant pressure $c_{p,o}$ and the heat transfer coefficient $c_{h,io} = 0.012$.

The open-water heat flux

$$Q_{ow} = Q_{ao} + \rho_i^* L_f \left(\frac{\partial h_i}{\partial t} \right)_{ow} \quad (2.33)$$

is a combination of the atmosphere/ocean heat flux Q_{ao} and the heat flux involved in the formation of sea ice with the latent heat of fusion L_f . Q_{ao} is calculated according to the open-water surface heat budget (see Equations 2.7 – 2.11).

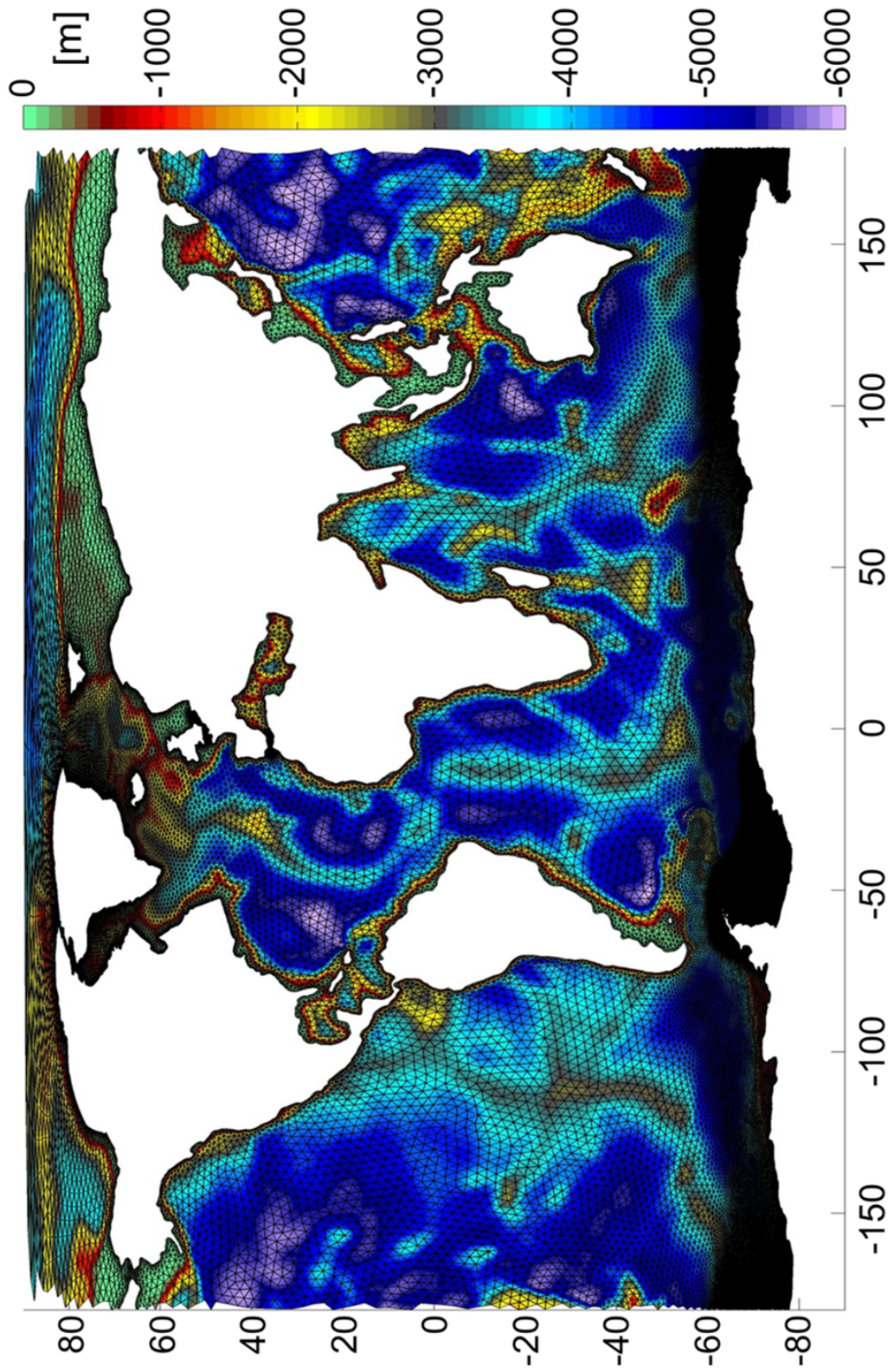


Figure 2.1: Surface grid and bathymetry of the model implemented for this study.

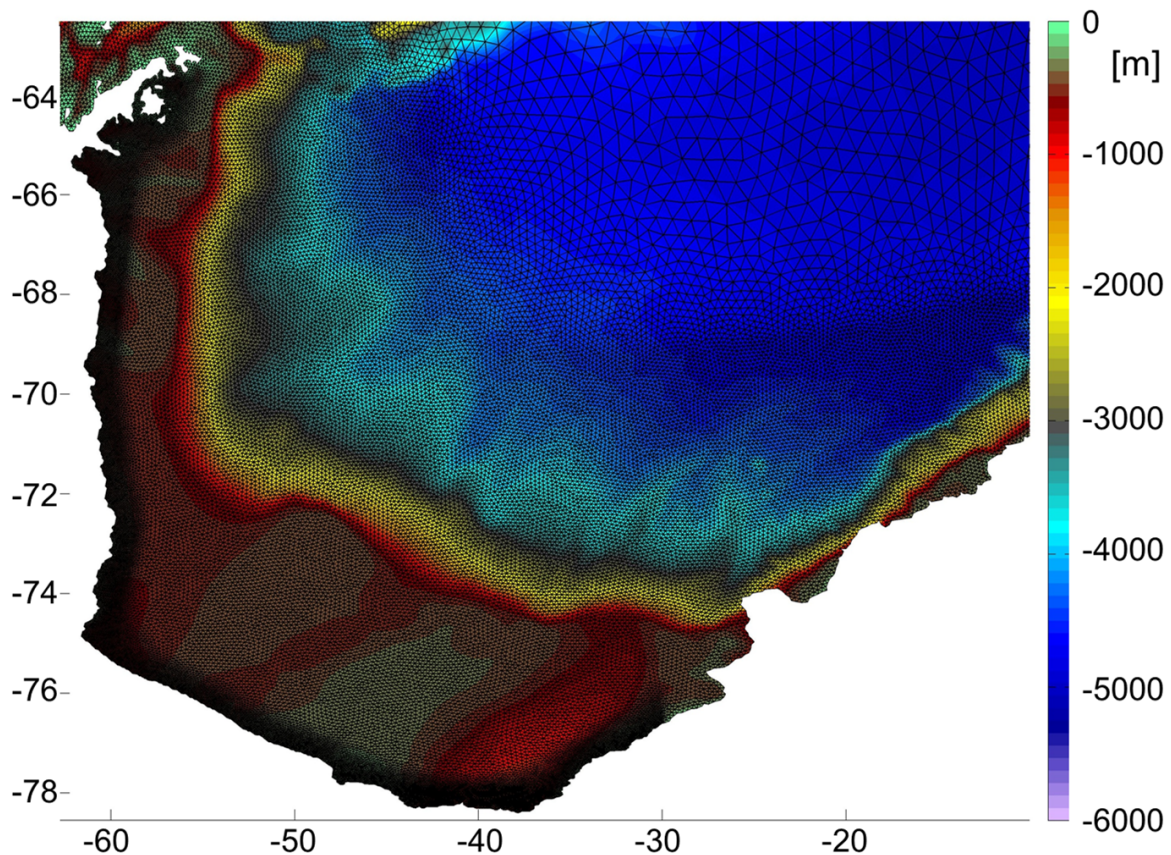


Figure 2.2: Surface grid and bathymetry of the model's implementation in the southwestern Weddell Sea.

2.2.4 Configuration and initialisation of FESOM

The model was run on a global unstructured grid with a horizontal resolution that ranges from 2.5° (max. 280 km) in the open ocean basins to less than 3 km at the western Weddell Sea coastline. Globally, the coastline was resolved with a resolution of 0.5° (max. 56 km) or better. Also, in the Southern Ocean a minimum resolution of ≈ 50 km was introduced but is widely exceeded (Figure 2.1). Above the southwestern Weddell Sea continental shelves and in the vicinity of the continental slopes horizontal resolution is again refined to 10 km or less and ultimately a narrow belt along the coastline is resolved with 5 km or less (Figure 2.2). Due to the spherical shape of the earth, resolution increases with latitude reaching approximately 3 km at the front of the Filchner-Ronne Ice Shelf.

In vertical direction, 37 depth levels (z-levels) were installed with increasing resolution toward the surface. Starting out with a layer thickness of 10 m between levels, thickness first increases by 5 m with every subsequent layer. At 270 m depth, the increase of layer thickness

Layer no.	Depth	Layer no.	Depth	Layer no.	Depth
1	0 m	14	670 m	27	3500 m
2	10 m	15	820 m	28	3750 m
3	25 m	16	990 m	29	4000 m
4	45 m	17	1180 m	30	4250 m
5	70 m	18	1390 m	31	4500 m
6	100 m	19	1600 m	32	4750 m
7	135 m	20	1825 m	33	5000 m
8	175 m	21	2050 m	34	5250 m
9	220 m	22	2275 m	35	5500 m
10	270 m	23	2500 m	36	5750 m
11	340 m	24	2750 m	37	6000 m
12	430 m	25	3000 m		
13	540 m	26	3250 m		

Table 2.1: Depths of the horizontal z-layers of the model’s implementation.

is advanced to 20 m. At the depth of 1390 m, layer thickness is prescribed as 210 m. From 1600 m to 2500 m depth, layer thickness is set to 225 m and finally the maximum layer thickness of 250 m is reached at all depths below 2500 m. The exact depths of the individual z-layers are listed in Table 2.1.

To enable a smoother and more realistic representation of bathymetry the bottom nodes are allowed to deviate from the depth levels in a manner similar to the shaved-cells approach in finite-difference models (Wang, 2007). The topographic dataset RTopo-1 (Timmermann et al., 2010) was used to create the model bathymetry. It has a resolution of 1’ and was smoothed under consideration of the horizontal model grid resolution before the interpolation of depth values to the 2D-grid nodes. In total, the grid features $1.8 \cdot 10^6$ grid nodes (92881 surface nodes).

The model was initialised on January 1st 1980 with data from Polar Science Center Hydrographic Climatology (Steele et al., 2001). The timestep was set to 3 min since the high spatial resolution of the model requires a correspondingly high temporal resolution. The results were recorded as daily mean values.

2.3 Atmospheric forcing of FESOM

To provide the atmospheric surface forcing for the long-term simulation, NCEP/NCAR Reanalysis data (Kalnay et al., 1996) is used. To test for sensitivity to forcing (Section 6), branched-off shorter runs use higher-resolution Global Model Europe (GME) data (Majewski et al., 2002; Majewski and Ritter, 2002) and locally highly-resolved regional model data from COSMO (Steppeler et al., 2003; Baldauf et al., 2011) (in combination with the

global GME data set) as atmospheric forcing. A short introduction to the different data sets and their application is given in this chapter.

The variables of all forcing data sets are interpolated in space from the gridpoints on which they are provided to the FESOM surface grid points and in time between the points at which they are given to every individual FESOM time step.

2.3.1 NCEP / NCAR Reanalysis

The long term atmospheric forcing for the years 1980-2009 was derived from the NCEP / NCAR Reanalysis data set (Kalnay et al., 1996). This is a global dataset with a horizontal resolution of 1.875° . Daily datasets of 10-m wind velocity \vec{u}_{10} , 2-m air temperature T_a , 2-m specific humidity q , precipitation rate P , relative cloud cover C and latent heat flux Q_l are used. From these quantities, evaporation E is calculated as

$$E = \frac{Q_l}{L_e \rho_w} \quad (2.34)$$

with the latent heat of evaporation L_e of water and the density of water ρ_w . Incoming longwave radiation Q_{lw}^\downarrow and incoming short wave radiation Q_{sw}^\downarrow are calculated from the respective terms in Equations 2.9 and 2.8, where the vapor pressure in the air $e_{v,a}$ in Pa is approximated by

$$e_{v,a} = q \cdot p_a \cdot \frac{M_{da}}{M_w} \quad (2.35)$$

with the molar mass of dry air M_{da} and the molar mass of water M_w .

2.3.2 GME

The GME model is a global weather prediction model developed by Germany's national meteorological service, the Deutscher Wetterdienst (DWD). It is based on an almost uniform icosahedral-hexagonal grid with a horizontal resolution of 40 km. In vertical direction the model features 60 layers from the earth's surface up to a height of approximately 34 km.

A 6-hourly dataset covering the period from April 2007 to December 2009 was provided by L. Ebner from University of Trier, Germany. It contains the variables 10-m wind velocity \vec{u}_{10} , 2-m air temperature T_a , dew point T_d , sea level air pressure p_a , precipitation rate P and relative cloud cover C . The data was interpolated from the original model grid onto a regular grid with 0.5° spacing. To obtain the variables necessary to run FESOM, the vapor pressure $e_{v,a}$ is calculated using the empirical relationship with the dew point T_d

$$e_{v,a} = 6.11^{-3} \cdot e^{\frac{19 \cdot T_d}{T_d + 250}} \quad (2.36)$$

giving results in mbar.

With the result from (2.36), the specific humidity q is calculated using (2.35).

Then the latent heat flux Q_l and the evaporation E are determined according to the standard bulk formulas

$$Q_l = L_e \rho_w E = L_e \rho_a c_e |\vec{u}_w| \cdot (q - q_s) \quad (2.37)$$

with the transfer coefficient of latent heat $c_e = 1.75 \cdot 10^{-3}$ and the saturated surface specific humidity q_s

$$q_s = 0.98 \cdot \frac{640380 \frac{\text{kg}}{\text{m}^3}}{\rho_a} \cdot e^{\frac{-5107.4\text{K}}{T_o}} \quad (2.38)$$

where T_o is the ocean surface temperature in K.

The calculations for longwave and shortwave radiation are the same as for the NCEP data set. For more detailed information on the GME model please refer to Majewski et al. (2002) and Majewski and Ritter (2002).

2.3.3 COSMO

The COSMO model (Baldauf et al., 2011) is named after the **C**onsortium for **S**mall-scale **M**odelling whose members are meteorological and military services from 7 European countries. It is a further development of the Lokalmmodell (Doms and Schättler, 2002; Doms et al., 2005) of DWD. COSMO is a regional fully-compressible, non-hydrostatic, hydro-/thermodynamic, primitive-equation atmosphere model with terrain-following vertical coordinates.

Data from two realisations of the COSMO model were provided by L. Ebner from University of Trier, Germany, covering the period from March to August 2008 with hourly mean values. The first COSMO data set stems from a model run with 15 km horizontal resolution and will therefore be called COSMO-15 in this study, while the second configuration has a horizontal resolution of 5 km and will be called COSMO-5. The data was supplied on a regular grid with 0.125° (COSMO-15) and 0.05° (COSMO-5) spacing.

The model providing the COSMO-15 data set covered the region between the corner points 98.37° W/ 58.36° S, 42.47° W/ 42.68° S, 7.21° E/ 54.72° S and 120.29° E/ 84.96° S (Figure 2.3). The data was applied to FESOM within an area south of 57.5° S from 75° W to 0° (also Figure 2.3). The COSMO-5 implementation with its higher horizontal resolution covers a smaller region than COSMO-15: the area between 86.75° W/ 65.36° S, 52.47° W/

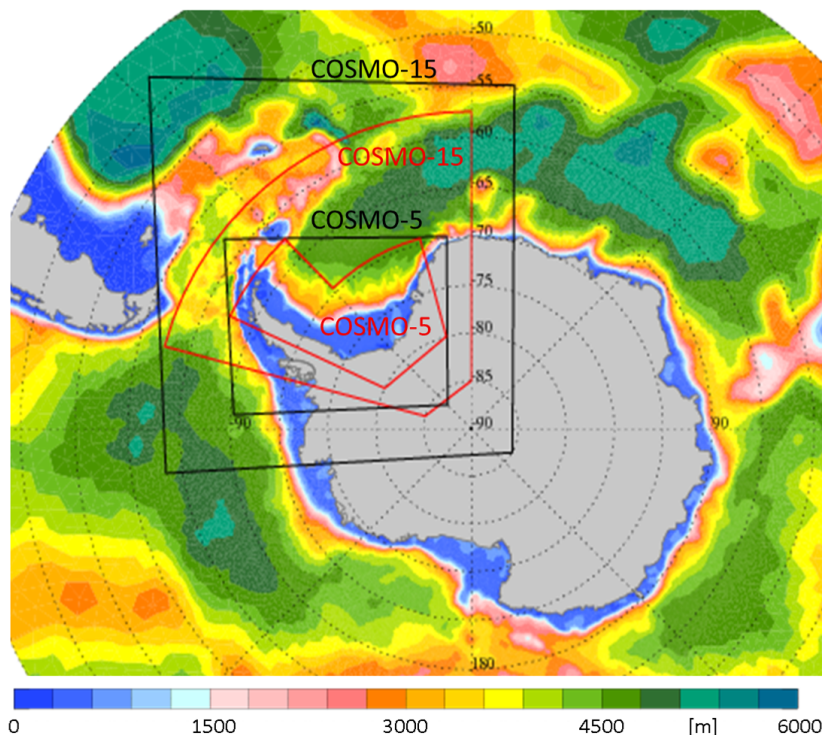


Figure 2.3: Domains of the COSMO implementations (black lines) and areas where the data is applied to FESOM (red lines).

58.10° S, 7.21° W / 69.85° S and 44.70° W / 86.5° S. The data was applied to FESOM in an L-shaped area: south of 62.55° S from 65° W to 44.5° W and south of 69.5° S from 44.5° W to 15.05° W (both Figure 2.3). While COSMO-15 receives its boundary conditions from GME, COSMO-5 is run with boundary conditions from COSMO-15 (so-called double-nesting). In all aspects apart from the geometric implementation and the boundary conditions, COSMO-5 and COSMO-15 are identical.

For both COSMO realisations, as in the GME case, the variables provided are 10-m wind velocity \vec{u}_w , 2-m air temperature T_a , dew point T_d , sea level air pressure p_a , precipitation rate P and relative cloud cover C . The calculation of vapor pressure $e_{v,a}$, specific humidity q , latent heat flux Q_l , evaporation E , longwave and shortwave radiation Q_{lw}^\downarrow and Q_{sw}^\downarrow follows the same equations as given in Section 2.3.2 about GME forcing data.

In the COSMO-forced FESOM runs, GME forcing was applied during the period 01.04.2007–29.02.2008. Also during the period March to August 2008, both COSMO data sets were complemented by the GME dataset to achieve global coverage. The GME data set was chosen since it provided the boundary conditions for the COSMO model runs (although only indirectly for COSMO-5) and thus major discontinuities in the forcing fields are

avoided.

3 Model validation

When working with model data, one always has to put the validity of the model results into perspective. Since no model with the complexity of an Ocean General Circulation Model can include or perfectly parameterize every physical process affecting the prognostic variables, every model's results are subject to uncertainties. Comparisons of model results with independently acquired data are a widely-used way to get a measure of the model's trustworthiness.

In this chapter the effects of omitted features are discussed. To assess the reliability of the simulation, comparisons of sea ice concentration and thickness as well as water properties on the continental shelf and in the deep Weddell Sea with independent observations are analysed.

3.1 Omissions in the applied version of FESOM

This version of FESOM, described in Section 2, does not include tidal effects, the cavities below the ice shelves or icebergs. The influence of tides is discussed in Section 3.1.1, the effects of ice shelf cavities are treated in Section 3.1.2 and the consequences of the omission of icebergs follow in Section 3.1.3.

3.1.1 Influence of tides

The influence of tides is highest close to the coastline or at sharp topographic steps as e.g. ice shelf fronts. The ocean currents are shifted by the predominant tidal mode but unless residual currents are produced the effect on the oceanic velocity field is rendered negligible when daily averages are considered. The tidal motion, however, can have a significant effect on the sea ice cover.

By enhancing divergent drift, tides favour the opening of leads and thus increase the open water fraction (Padman et al., 1998; Morales Maqueda et al., 2004). Especially the alternation of convergent and divergent ice drift will be of strong influence, since the convergent ice drift causes the floes to raft and build ridges, packing the ice tighter and reducing the ice-covered area. The following divergence will cause leads to open. This interplay results

in an increase of ocean-atmosphere exchange processes and in added ice production if freezing conditions prevail. Since such tide-induced leads primarily open close to the coastline, and effectively constitute a narrow tidally forced coastal polynya. The associated freezing processes lead to increased brine release and eventually a rise in HSSW volume (Padman et al., 1998; Makinson and Nicholls, 1999) and water mass density.

Mooring data from the Ronne ice front show a dominance of the semidiurnal tidal modes (Makinson and Schröder, 2004). Robertson et al. (1998) observed tidal current speeds that are 5-10 times stronger than the mean current speed on the continental shelf of 6 cm/s (Kottmeier and Sellmann, 1996; Fahrback et al., 1994). Makinson and Nicholls (1999), who modelled the tidal currents in the southwestern Weddell Sea and under the Filchner-Ronne Ice Shelf, found peak tidal velocities of 1 m/s during spring tide. Their results indicate that no substantial transport of ISW occurs by residual tidal outflows from under the Ronne Ice Shelf west of Berkner Island due to the strong barrier currents.

Another important effect of tides is the increase of bottom shear and mixing (Robertson et al., 1998; Morales Maqueda et al., 2004). From analysing current meter data from moorings near the Ronne Ice Front, Makinson et al. (2006) found that during the stratified regime of the summer months an additional boundary layer is present that originates from the base of the ice shelf and influences a stretch of a few tens of km width along the ice shelf front. This second boundary layer increases shear and vertical mixing in the water column substantially. It is only observed in summer and its non-existence in the model provides a possible explanation for the underestimation of the summer mixed layer depth in the simulation and the ensuing overestimation of warming of the surface waters and ice melt (see Section 3.4).

3.1.2 Influence of ice shelf cavities

Ice shelf cavities play a crucial role in the formation of Ice Shelf Water, the formation process of which is described in Section 1.2.2. Since the model version used in this study does not include the ice shelf cavities, I will assess which variables are affected by the omission and estimate the influence on them.

For the ice shelf cavity to change HSSW to ISW the water has to remain under the ice shelf for a prolonged time period, indicating a big ice shelf, and the depth of the ice shelf bottom has to be considerable in order to attain a significant reduction of the freezing point. It is therefore acceptable to presume that the vast majority of ISW in the Weddell Sea is formed under the Filchner-Ronne Ice Shelf and I will limit my considerations to this area.

At the Ronne Depression the sea floor is sloped southward and due to its high density HSSW can sink into the cavity under the ice shelf. However, the access is not unlimited

and only a fraction of the HSSW will pass below the ice shelf. From current meter moorings, Nicholls et al. (2003) estimate a flow of 0.9 Sv of HSSW underneath the ice shelf at Ronne Depression, Makinson et al. (2011) yielded 0.6 Sv as Ronne Depression inflow in a simulation including tides and Foldvik et al. (2001) found 0.5 Sv inflow for the Ronne Ice Shelf front between Berkner Island and the Ronne Depression, which gives a total estimate of 1.0-1.4 Sv HSSW that enter the cavity. This is in good agreement with the 1.6 Sv ISW outflow Foldvik et al. (2004) found at the Filchner sill.

In the cavity the water is cooled by melting the glacial ice at a depth where the in-situ freezing point is below the surface freezing point of salt water. The gain in volume by entraining the meltwater is only a very small fraction of its original volume and the salinity decreases by roughly 0.1 (Nicholls et al., 2003). Also, during the subsequent rising motion, the water volume can be reduced by the formation of marine ice at the ice shelf bottom as was observed at Filchner Ice Shelf (Foldvik and Gammelsrød, 1988). Thus, the volume of HSSW entering into the cavity roughly equals the volume of ISW leaving the cavity.

The first important effect of the ice shelf cavities for the deep Weddell Sea lies in the very cold temperatures of ISW, which is supercooled with respect to the surface freezing point. Even after mixing with ambient waters, the resulting water mass retains very cold temperatures and low salinities. Due to the thermobaric effect it gains density with depth faster than a water mass with the same in-situ density, but a higher salinity. Thus, deep water mixed from ISW has a higher probability to end up as bottom water. Due to the omission of ice shelf cavities in the model, the WSBW in the simulation is likely to slowly gain heat and lose density since the supply of ISW is missing.

The second important influence is the relocation of the dense water overflow from the western continental shelf to the outflow from the Filchner Trough in the east. The deepest outflow for IWS at the Filchner-Ronne Ice Shelf is at 610 m depth where the Filchner Trough meets the continental shelf break. This is several hundred kilometres to the east from where the original HSSW was formed. A large fraction of the ISW-originated deep water will not circulate along the continental slope with the Weddell Gyre, but upon spilling from the Filchner Trough it meets with a prominent underwater ridge at approximately 36° W and is steered down-slope by Akademik Fedorov Canyon without following the Weddell Gyre westward. Thus, the ISW-originated deep water is more likely to stay within the Weddell Sea.

3.1.3 Influence of icebergs

From a physical point of view, the presence of an iceberg influences the surrounding environment primarily in three ways:

- An iceberg consists of glacial ice and is a source of freshwater, since during its lifetime it is in a constant process of melting. During winter on the continental shelf water temperatures are below the freezing point of glacial ice; however, the salt content of the waters still induces a slow melting on the accessible surface. In summer or if warmer waters are present, the melting process is strongly accelerated. Over the deep ocean, large icebergs, due to their deep draft, often reach below the cold surface waters and thus also experience increased melting. Silva et al. (2006) estimate the freshwater flux from icebergs in the Weddell Sea to exceed net precipitation, which leaves it much smaller than the seasonal freshwater flux associated with sea ice formation or melting (see Section 4.1) but in most places of the same order of magnitude as the sea ice-related freshwater balance of the entire year (see Section 5.1).
- Due to the bulk of an iceberg, its drift characteristics differ from those of sea ice (Hunke and Comeau, 2011). Therefore an iceberg can not only block sea ice motion (Markus, 1996) or by pushing on the ice induce dynamic growth, but in addition the relative velocity creates a polynya, which in terms of heat flux, sea ice production and water modification acts in the same way as a coastal polynya. By changing the sea ice drift, an iceberg can also prevent coastal polynyas to form at parts of the coastline or shelter a part of coastline and increase polynya extent and frequency there (Markus, 1996; Tamura et al., 2008).
- A massive iceberg, especially when grounded, can even change the circulation of the ocean. This was found e.g. for A23 in a study by Grosfeld et al. (2001), who investigated the changes exacted by the calving event of icebergs A22, A23 and A24, their subsequent drift and the grounding events on the adjacent Filchner Trough which caused some of the HSSW formed around the icebergs to feed into the outflow waters which consequently became warmer and saltier.

3.2 Sea ice concentration

One of the best known quantities of polar oceans is sea ice concentration. It can be measured by satellites using microwave radiation, which is daylight-independent and can penetrate

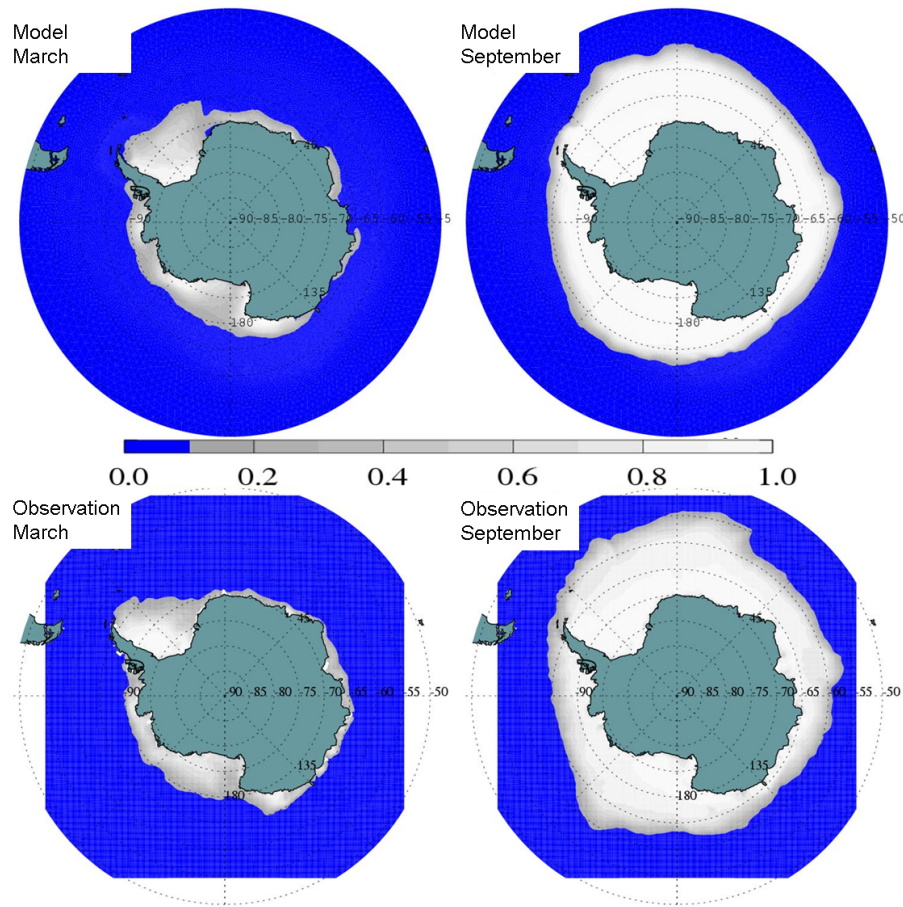


Figure 3.1: Multi-year mean of the sea ice concentration in March/September 1990-2009 from the simulation (top panels) and SSM/I data (bottom panels).

clouds with little attenuation. Thus, year-round data acquisition on a large spatial scale is possible.

To assess the large-scale performance of the model, a comparison of multi-year mean maps of sea ice concentration in March and September from both SSM/I measurements (Cavaliere et al., 2008) and the simulation is presented (Figure 3.1). The March sea ice extent closely coincides with the minimum sea ice extent at the end of summer and September is close to the maximum extent at the end of the winter season.

In general, the model results and satellite based observations agree very well, however, several differences in details occur. In summer, the simulation slightly underestimates the sea ice cover of the Indian Ocean sector, while in the Weddell Sea the ice-covered area in summer is overestimated. The slightly lower ice concentration values in the simulation in most of the Weddell Sea indicate that the model does not per se overestimate the ice-covered

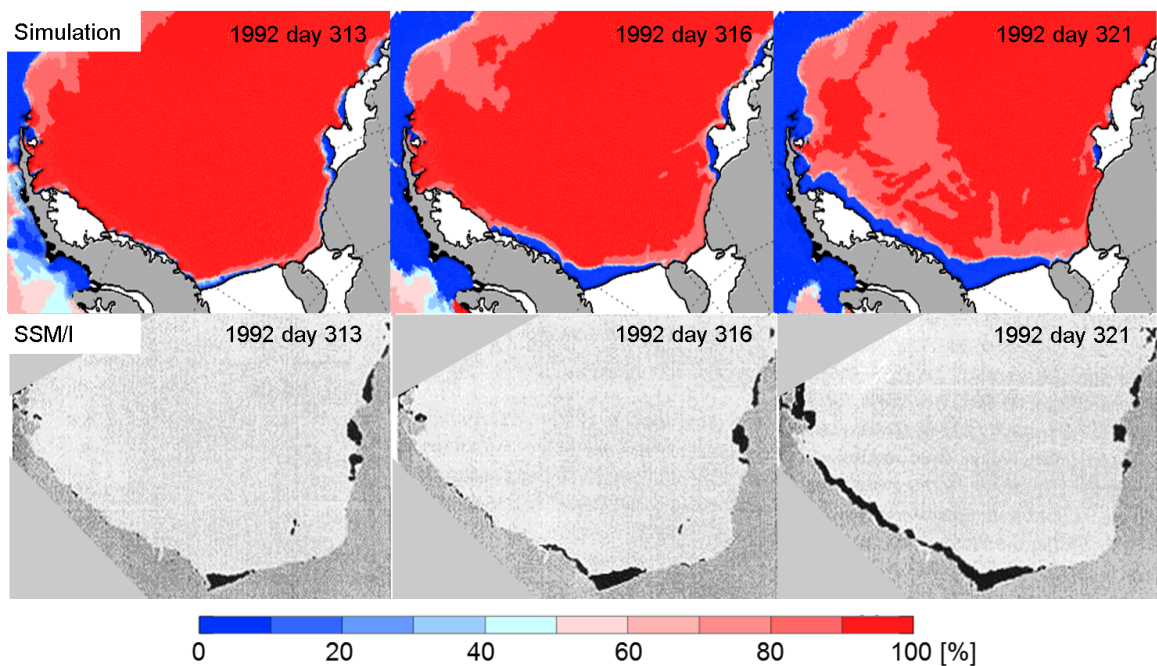


Figure 3.2: Comparison of simulated sea ice concentration (upper panels, colorscale) with polynya area derived from SSM/I data by Markus et al. (1998) (lower panels, black) in late spring 1992

area but rather the interannual variability in location of the remaining ice field.

The September picture reveals the model's maximum sea ice extent to be of a much smoother geometry than observations indicate. Since the ice edge in winter is primarily defined by the warm waters of the Antarctic Circumpolar Current, this may be due to an ACC that, due to the model's smoothed bathymetry, experiences less topographic steering. Especially the eastern boundary of the Weddell Gyre at 25° E, the eastern flank of the Kerguelen Plateau at 80° E and the Pacific-Antarctic Ridge at 150° W fail to make a strong imprint on the sea ice edge in the simulation.

On smaller spatial and temporal scales, coastal polynyas become apparent in ice concentration maps as areas of low values. To assess the model's ability to reproduce the formation of polynyas, a late spring and a late autumn event are presented. Simulated ice concentration maps of the western Weddell Sea (three days out of a 9-day period in November 1992) are compared to polynya areas that were defined by Markus et al. (1998) using an algorithm developed by Markus and Burns (1995) on SSM/I data (Figure 3.2). The algorithm improves the possibilities to extract polynya extent from satellite images, but it has to be kept in mind that due to the footprint of the measuring method, very narrow polynyas will not always be captured by the satellite imagery. Markus and Burns (1995) used a threshold value of 75 %

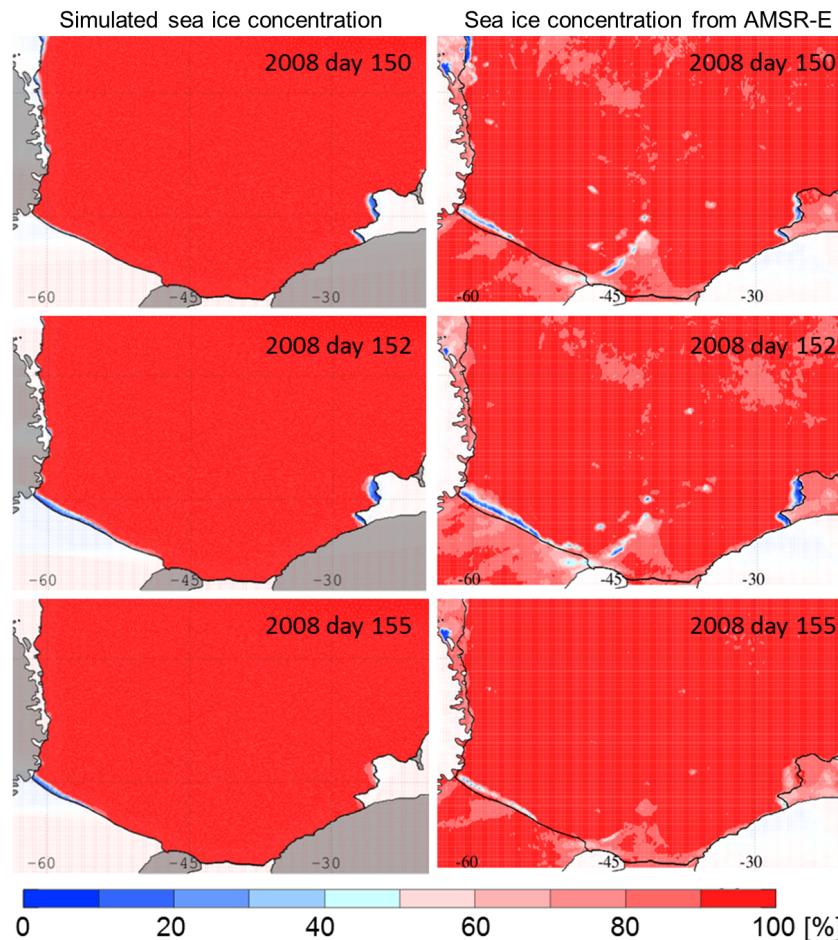


Figure 3.3: Comparison of simulated sea ice concentration (left hand panels) with AMSR-E data (right hand panels) in late autumn 2008. In the left hand panels, the actual coastline may differ from the drawn coastline, since the ice shelf fronts are subject to change.

ice concentration to identify polynyas.

On day 313, the simulated ice concentration shows open polynyas to the west of Cape Norvegia, Riiser-Larsen Ice Shelf and Brunt Ice Shelf. A less distinctive signal is visible along the Coats Land coastline. The polynya in front of Ronne ice shelf is open and while narrow in the eastern part widens toward the Antarctic Peninsula. Along the southern coastline of the Antarctic Peninsula several small polynyas are open in the simulation. On the same day, Markus et al. (1998) also identified polynyas next to Cape Norvegia, Riiser-Larsen Ice Shelf and Brunt Ice Shelf as well as along the north-eastern part of Coats Land. At Ronne Ice Shelf they found a polynya along the western part of the front (widest in the corner with the Antarctic Peninsula).

After three days (day 316), the polynyas along the eastern ice shelves still look similar in the simulation, however the polynya at the Coats Land coastline is closed. The polynya in front of Ronne Ice Shelf has increased in size and elongated northward along the Antarctic Peninsula to the southern boundary of Larsen C Ice Shelf. Also Markus et al. (1998) found the eastern polynyas open with exception of the Coats Land coast and the Ronne polynya enlarged and continuing along the peninsula. However, they find it smaller than simulated and covering the coastline only from $\approx 54^\circ$ W to $\approx 72^\circ$ S.

Another five days later (day 321), the simulation shows the eastern polynyas diminished. Only the northern Brunt polynya is still of considerable size and remnants are visible next to Cape Norvegia and west of Riiser-Larsen Ice Shelf. In the west, however, the open water reaches from Berkner Island to the tip of the Antarctic Peninsula in a wide belt. Markus et al. (1998) found the western polynya slightly narrower and thus reaching only from $\approx 51^\circ$ W to $\approx 66^\circ$ S (northern boundary of Larsen C Ice Shelf) with small interruptions. In the east, they found evidence of a small polynya at Cape Norvegia, the Riiser-Larsen polynya and both Brunt polynyas.

The model performs well regarding the localisation of open polynyas, also the opening process from the Ronne polynya in the southwestern corner along the shoreline of the Antarctic Peninsula toward the northern tip over time is well recreated. Polynya size, however, while it still compares well with observations in the eastern part, is clearly overestimated by the simulation in the western part. The polynya size differences are caused by an underestimation of the mixed layer in spring and summer (see also Section 3.4), which in combination with the positive ice-albedo feedback leads to an overestimation of surface heating and ice melt. Thus, it is an issue limited to the melting season.

The example of a freezing season polynya event (three days out of a 6 day period in May/June 2008; Figure 3.3) will illustrate the model's representation of the wintertime processes. The satellite data are AMSR-E measurements (Spreen et al., 2008) that were obtained via the Center for Marine and Atmospheric Sciences (ZMAW), a cooperation between the University of Hamburg and the Max Planck Society.

On day 150, the simulation shows very low ice concentrations to the west of the Brunt Ice Shelf which compares very well with the satellite observations. The polynya at the Ronne Ice Shelf, however, is barely visible in the simulations while the AMSR-E data shows a definite opening. Both AMSR-E data and model feature a polynya in front of Larsen C Ice Shelf, although the model shows it narrower and more elongated to the south. The satellite data also show a polynya north of Berkner Island that is formed downwind of a fast-ice bridge between the iceberg A-23A and Berkner Island. Since the model does not include icebergs, it lacks the capability to reproduce polynyas connected to them. Both the fast-ice bridge and

the iceberg are visible in the satellite measurement as a signal of reduced ice concentration. Often, also the ice shelves register as areas of reduced ice concentration. Therefore, it is often challenging to correctly identify polynya area from satellite data (Tamura et al., 2008), especially since the coastline of the ice shelves changes constantly and no temporally fixed ice shelf mask can be used. In Figure 3.3 the depicted coastline is the coastline used in the simulation. The real coastline of the ice shelves is variable and may differ from the drawn line. The model's coastline was included in the picture to improve orientation and the AMSR-E data was plotted indiscriminately for ocean surface and ice shelves. In winter 2008, the biggest differences between model and real coastline appear to be along the coast of the Antarctic Peninsula, where patches of slightly reduced concentration values are stable over the 6-day period and thus indicate their identity as part of the ice shelf.

Two days later, on day 152, in both data sets the polynya in front of Larsen C Ice Shelf is closed and the Ronne polynya as well as the Brunt polynyas have grown in size. However, the simulated polynyas are smaller than observed. Also, the AMSR-E sea ice concentration still depicts a polynya in the lee of the fast ice bridge.

Another three days later, on day 155 all polynyas have receded. In simulation as well as satellite measurement the Ronne polynya still leaves the strongest signature. The simulation shows the Ronne polynya with a smaller area but lower ice concentration values than the AMSR-E data. In the simulation, the only other visible remnant of the polynyas is found at the northern Brunt polynya, where a slight reduction in ice concentration is discernible. The signal found in the AMSR-E data is similar in values, although further offshore. Also, in the observations the southern Brunt polynya leaves a more pronounced mark and the flaw polynya at the fast ice bridge is still faintly visible.

Again, the polynyas are well captured in both location and opening time. In winter and in contrast to the melting season, the simulation tends to underestimate polynya size. The lack of icebergs in the model amplifies the underestimation of total polynya area in this case.

3.3 Sea ice thickness

Not only sea ice concentration is of importance when assessing the capability of the model to simulate the sea ice cover. Sea ice thickness is another parameter that together with the ice concentration determines the ice volume. The measurement of sea ice thickness is not straightforward since ice floes can raft upon each other or build ridges under pressure e.g. by convergent drift. This leads to a high variability in sea ice thickness even if only one ice floe is considered. Ice core drilling gives only very local information and with its cost in manpower and difficult access is not a suitable method to achieve long-term or area-wide

data.

In the years 2003-2009 the Ice, Cloud and Elevation Satellite (ICESat) gathered wide-ranging datasets of the Arctic and Antarctic including sea ice thickness. The ice thickness measurements were conducted with a laser altimeter and unfortunately are very error-prone. The altimeter measures the height of the ice or snow surface above sea surface height (SSH), the so-called freeboard. However, in areas with high sea ice concentrations the exact identification of the SSH is difficult, since the footprint of the signal (70 m) will almost always include ice-covered areas. It is customary to assume the lowest 2 % of the measurements to represent the SSH (Yi et al., 2011). Thus, the measurements tend to underestimate freeboard. Sea ice with a density of 910 kg/m^3 is submerged with 89 % of its thickness in water with a density of 1027 kg/m^3 . An error of 1 cm in the freeboard measurement will thus result in an error of 8.8 cm when calculating the ice thickness. Another even more prominent source of error is the unknown snow layer thickness. The density of snow (290 kg/m^3) is much lower than the density of sea ice. Given a freeboard of 30 cm, an assumed 10 cm snow layer means an ice thickness of 2.0 m while 20 cm of snow yield an ice thickness of 1.4 m.

An alternative approach is the measurement of sea ice thickness from below. Upward Looking Sonars, deployed as part of a mooring, measure the sea ice draft via travel time of an acoustic signal. They will not provide spatially continuous data but local information over long time periods with high temporal resolution. By measuring the draft of an ice floe, instead of freeboard, the error propagation when calculating ice thickness is significantly reduced. An error of 1 cm in the ice draft will only result in an error of 1.12 cm in ice thickness. Still there is the uncertainty in snowlayer but given a draft of 1.5 m, assuming a 10 cm snow layer yields an ice thickness of 1.66 m while 20 cm of snow lead to 1.63 m ice thickness. Thus, the ice draft measurements provide much more reliable ice thickness values. Also their reproduction of the reference level, the ocean surface, is more accurate in high ice concentration areas since their footprint is smaller than the satellite's by an order of magnitude (5 m, given a deployment depth of 150 m and a beam opening angle of 2°) so that the few leads are more likely to be captured without interference.

At six locations in the western Weddell Sea, ULS instruments have been deployed within the years 1990-2009 (Figure 3.4). However, due to instrument loss and failure most locations were actively sampling for only 2 years or less. The westernmost location, station 207, alone was repeatedly equipped with a ULS sensor resulting in 7 years of data in three separate time intervals.

The instruments were deployed with depths ranging from 125 m to 175 m and measuring with time steps of 8-15 minutes. Per measurement, the instruments send out four 300-kHz pulses that are reflected at the surface so that the echo is received by the instrument. The

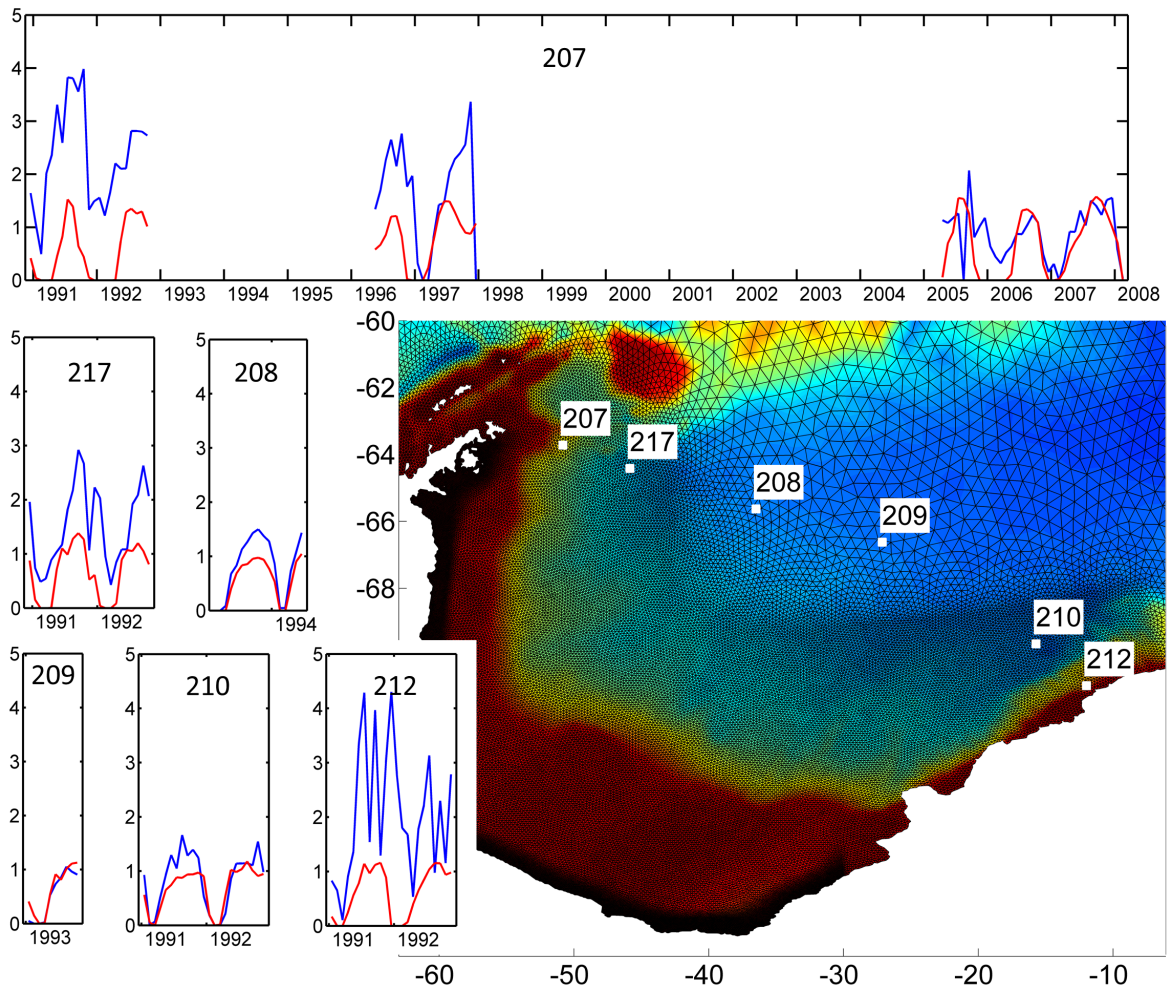


Figure 3.4: Locations of ULS instruments deployed in the western Weddell Sea, measured sea ice thickness (blue) and simulated sea ice thickness (red).

travel time is transformed into distance under consideration of the local vertical sound velocity profile which is determined with a dynamic-thermodynamic sea ice mixed layer model for the Weddell Sea described by Timmermann et al. (1999). The travel time of the signal is measured once the returning signal reaches a given threshold amplitude. It can therefore happen that spots with deep drafts within the footprint dominate the result of the measurement. This results in the measurements being biased toward higher ice thickness values. Also, as the instrument measures sea ice thickness, icebergs might pass over it and are recorded as exceptionally deep drafts. In the data processing, which was carried out by H. Witte and W. Dierking from Alfred Wegener Institute, drafts exceeding 30 m have been removed, since they are obviously caused by icebergs, but smaller icebergs remain undetected and thus

influence results toward higher values.

Station 207 was active from 12/90 to 10/92, from 05/96 to 12/97 and from 04/05 to 02/08. It is located close to the tip of the Antarctic Peninsula at 63.72° S, 50.82° W over the continental slope (Figure 3.4). The observations in the first measuring period show winter maxima of 4.0 m (10/91) and 2.8 m (07/92) ice thickness and summer minima of 0.5 m (02/91) and 1.2 m (02/92). The model shows maxima of 1.5 m (07/91) and 1.3 m (07/92). In the simulations, both summers are ice free and the strong increase in ice thickness in autumn 91 is not captured. From spring 1991 to the end of the measuring period, an approximate difference of 1.5 m between observation and simulation is maintained.

The second sequence of measurements displays summer maxima of 2.8 m (10/96) and 3.4 m (11/97) in the observations and 1.2 m (09/96) and 1.5 m (06/97) in the simulations. The summer 96/97 is ice-free although the model precedes the observations by 2 months. The summer 97/98 on the other hand still exhibits 1 m ice thickness in the model when the measurement period ends, while observations claim the location to be ice free.

During the last measurement period, observations and simulation agree remarkably well. While model data still have maximum values of approximately 1.5 m in winter, the observed data reduced their maxima from 3-4 m in the 90s to 1-2 m. The summers, with the exception of 2006 with a minimum of 0.3 m in March, are ice-free in model and observation.

A little bit further to the southeast, Station 217 is located at 64.42° S, 45.85° W. It collected data during the same time span as the first measuring period of Station 207 (12/90-10/92). Observations here yield winter maxima of 2.9 m (09/91) and 2.6 m (09/92) while simulations give 1.4 m (09/91) and 1.2 m (08/92). The summers are ice-free in the simulation but in the observations retain an ice thickness of approximately 0.5 m.

At Station 208, located at 65.63° S, 36.49° W and active from 02/93 to 06/94, the observed winter maximum of 1.6 m (10/93) is underestimated by the model (1.0 m; 10/93) and again at the end of the observation period (06/94) the modeled early winter ice thickness is 1.0 m and the observations yield 1.4 m. During both summers within the observation period, model and observations show the area ice-free.

At Station 209, which was measuring between 01/93 and 10/93 at 66.62° S, 27.12° W, model and observation are in very good agreement. Both show the location ice-free in summer. While the observed maximum thickness is 1.1 m in August 1993, in the model we find the same value as maximum at the end of the measuring period in October 1993.

Station 210 is positioned at 69.66° S, 15.72° W. It was active from 01/91 to 11/92. Here, observations and simulation display the usual seasonal cycle with winter maxima of 1.7 m (08/91) and 1.5 m (10/92) and 1.0 m (11/91) and 1.2 m (08/92), respectively, and the summers practically ice-free.

Very close to the coastline at Cape Norvegia (70.91° S, 11.96° W) is the position of Station 212. It covers the same time period as Station 210 (01/91-11/92). In the case of observations highly fluctuating sea ice thickness values ranging from 0.1 m to 4.3 m with a tendency of the lowest values to occur in late summer. The simulation shows a typical seasonal cycle: ice-free summers and winter maxima of 1.2 m ice thickness (10/91 and 08/92).

In general, the model produces a smoother seasonal cycle than the observations display. Also, simulations tend to underestimate sea ice thickness with maximum values usually between 1 m and 1.5 m. In the central part of the section, this is a good representation of the sea ice thickness. Approaching the coastline, however, observed ice thickness increases and at the two stations closest to the coastline values between 3 m and 4 m are not uncommon.

This discrepancy between model and measurement is probably due to the model's underestimation of ridging and rafting processes. Sea ice gains only part of its thickness by thermodynamic growth processes but much is added by ridging and rafting processes that are caused by pressure exerted on the floes. But ridging and rafting events do not only increase sea ice thickness directly, they indirectly further thermodynamic growth of sea ice by reducing the area of the ice floes and increasing the area of leads.

The forces causing the ice floes to raft or build ridges can be convergent ice drift induced by winds or currents and ice drift against an obstacle such as the coastline or even icebergs. Tides that periodically press the sea ice against the coastline can have a major impact on the resulting ice thickness. Since tides are not represented in the model, sea ice thickness especially close to the coastline tends to be underestimated. Also, it has to be kept in mind that the measuring method of ULS instruments is biased toward higher thicknesses and small icebergs might have influenced the observations.

3.4 Temperature and salinity of the on-shelf water column

Observations of temperature and salinity on the southwestern Weddell Sea continental shelves are scarce. Wintertime observations in this area are almost nonexistent. Still, data from a few summer expeditions is available during which CTD-profiles in front of Ronne Ice Shelf were taken. These date from the 1980's and 1990's. Since the first decade of the model run is considered spin-up time for the model, only data from the 90's is used in this comparison. A location on the eastern flank of Ronne Depression was chosen for its likeliness to be within an active polynya. The geographical location of the CTD measurements is farther north than the chosen location of the modeled profile but the decisive variable here is distance from the ice shelf edge. In May 2000 the Ronne Ice Shelf edge was changed signif-

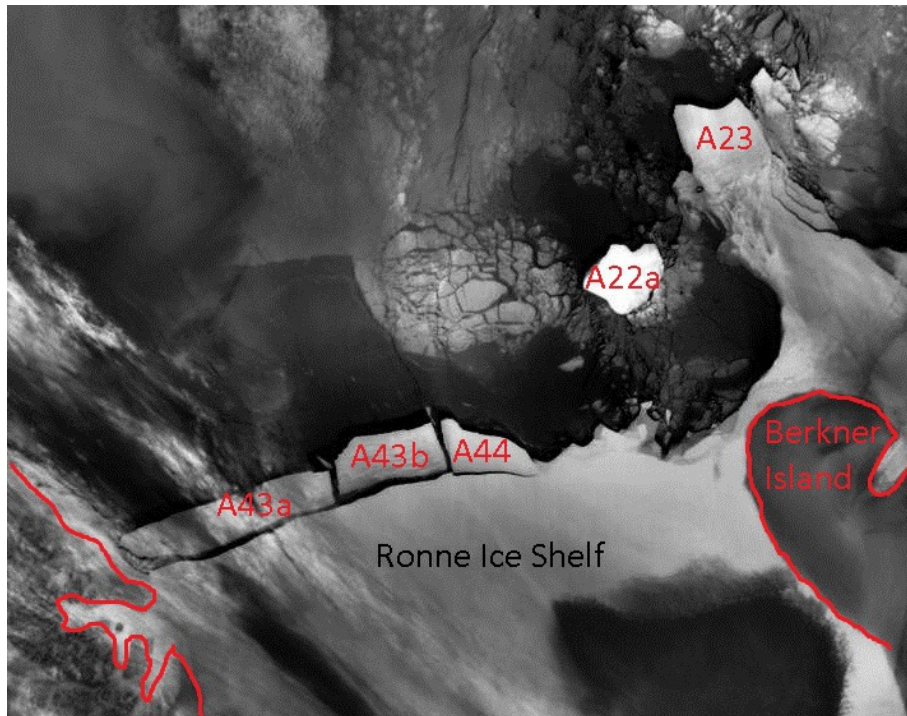


Figure 3.5: A thermal image of Ronne Ice Shelf front on May 6, 2000. Visible are the recently calved icebergs A43a, A43b, A44 and the older icebergs A22a and A23 (calved from Filchner Ice Shelf in 1986) as well as the fast ice bridge between A23 and Filchner Ice Shelf/Berkner Island. Satellite image from the National Snow and Ice Data Center (Scambos et al., 1996).

icantly by the calving of iceberg A43, which had a width of 30 km (Figure 3.5). Since the measurements were taken before the event, while the model works with a more recent coastline, the distance to the ice shelf edge is similar for the measured and the modeled profiles. In Figure 3.6 the CTD locations were therefore corrected by moving them south by 0.27° (30 km). Specifications which CTD-profiles are used in this comparison can be obtained from Table 3.1.

In the lower water column, simulated temperature profiles in all three years are close to the surface freezing point and only stray from there toward warmer temperatures (Figure 3.7, top panels). Considering the model's incapability to produce ISW, this behaviour is expected. Below a depth of 200 m the largest differences between model and observation are ca. 0.15 K but usually less. Temperatures above 200 m exhibit a much larger variability in the years 1995 and 1998 when a summer polynya is present at the Ronne Ice Front compared to 1999 when the entire water column is close to the freezing point and the simulation exhibits strong temporal stability.

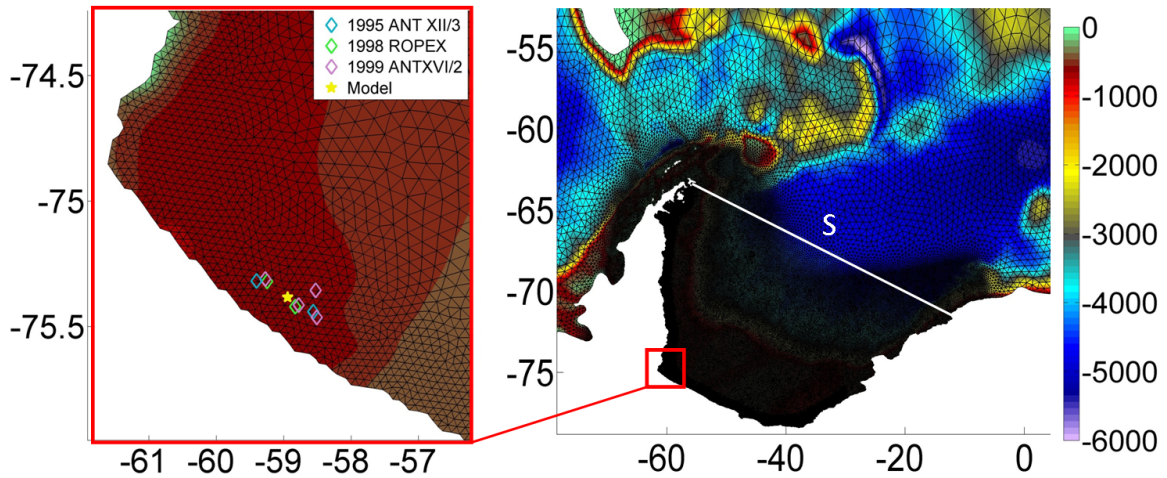


Figure 3.6: Locations of observed and simulated temperature and salinity profiles. Since the model coastline shows a situation after the break-off of iceberg A43 in 2000 and observations are from the 1990s, CTD locations were corrected relative to the ice shelf edge by a southward shift of 0.27° .

Station	Expedition	Date	Longitude	Latitude	Citation
PS34/175-1	ANTXII/3	1995-02-17	-60.3100	-74.2267	Schröder, 2010
PS34/176-1	ANTXII/3	1995-02-17	-60.0117	-73.9883	Schröder, 2010
PS34/177-1	ANTXII/3	1995-02-17	-59.3817	-73.9967	Schröder, 2010
PS34/178-1	ANTXII/3	1995-02-17	-58.7417	-74.0033	Schröder, 2010
ROPEX_084-1	ROPEX	1998-02-01	-59.0213	-74.4462	Jenkins, 2006a
ROPEX_085-1	ROPEX	1998-02-01	-59.3217	-74.43	Jenkins, 2006b
ROPEX_086-1	ROPEX	1998-02-01	-59.9217	-74.3883	Jenkins, 2006c
PS53/020-1	ANTXVI/2	1999-02-02	-60.9597	-74.7098	Rohardt and Harms, 2010
PS53/022-1	ANTXVI/2	1999-02-02	-61.1482	-74.7143	Rohardt and Harms, 2010

Table 3.1: CTD-Stations used in the on-shelf comparison (Section 3.4)

In 1995 and 1998 surface temperatures are above the freezing point and, most pronounced in 1998, the model shows a warm bias at the surface. The simulated mixed layer depth is very shallow and simulated temperatures at depths of 20-70 m are colder than observed.

The salinity profiles (Figure 3.7, bottom panels) reveal an underestimation of salinity in the upper 100 m and a tendency to overestimate salinity in the lower water column. Only in 1999 simulated salinities are lower than observed throughout most of the water column. Surface values are best recreated in 1995 where the ranges of simulation and observations overlap, but can be as far off as 0.8 (1998). Also, the bottom salinities are best matched in 1995 where the simulated value of 34.83 is within the range of observations while in 1998 bottom salinity is overestimated by the simulation by 0.14. The high bottom salinity values in 1999 are probably due to remnants of HSSW from the previous year. While observed

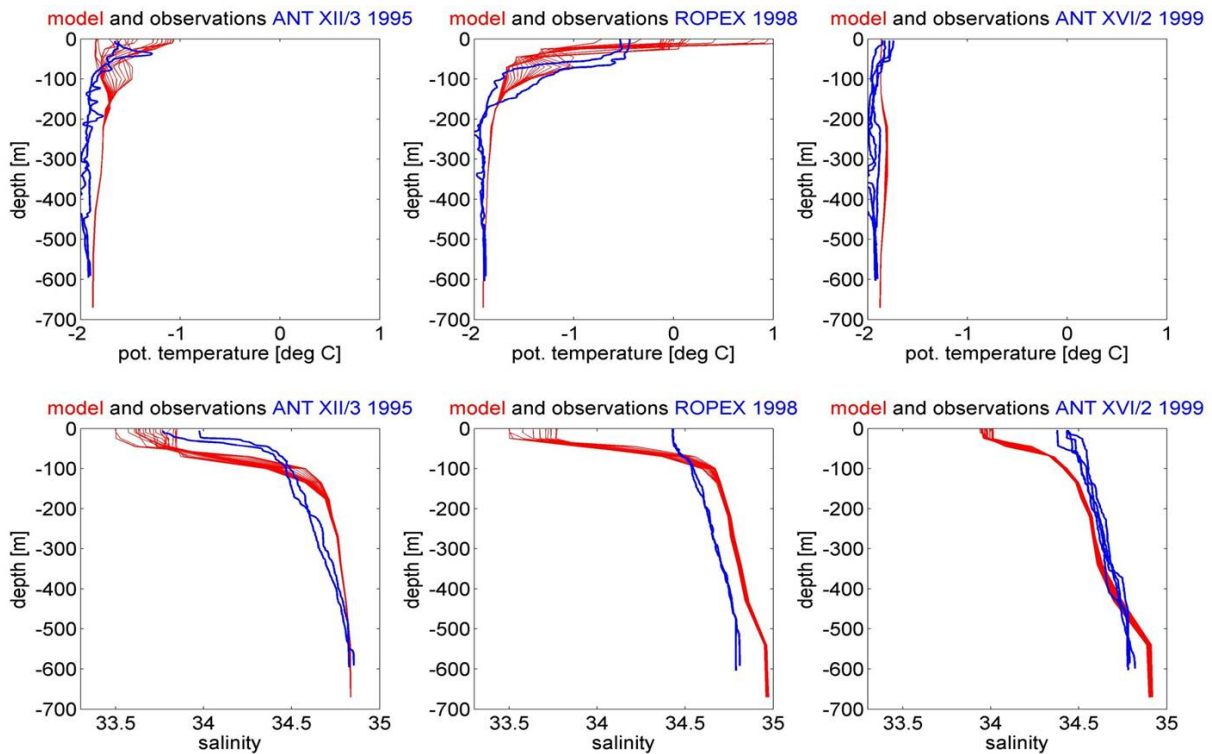


Figure 3.7: Observed and simulated temperature and salinity profiles in front of Ronne Ice Shelf. CTD measurements were taken in February 1995, 1998 and 1999. Simulated profiles show daily mean values for a time span of ± 10 days around the day of the observation. Note: The different simulated profiles show variations over time, while observed profiles differ in location (and were taken within a very short time range).

salinities through most of the water column change little between the different years, the model seems to overestimate the interannual variability of salinity on the continental shelf.

The modelled surface waters tend to be fresher and warmer than observed during summer. This is a systematic flaw in the simulation. The exaggeration of surface warming and freshening is rooted in a slight underestimation of vertical mixing in the model (also connected to the lack of tides), resulting in a too shallow surface mixed layer. Thus, the ocean distributes the heat it receives mainly by shortwave radiation within a too small volume, which leads to a warm bias in summer surface temperatures. This entails an overestimated sea ice melt which in turn reduces the high albedo area and leads to a positive feedback. At the same time the fresh water input from melting increasingly inhibits mixing and deepening of the surface layer. Over the summer season this self-enhancing loop can cause substantial discrepancies between model and observations, especially when sea ice conditions are light. With the low solar angles and the cold air temperatures at the end of summer, the surface layer is cooled

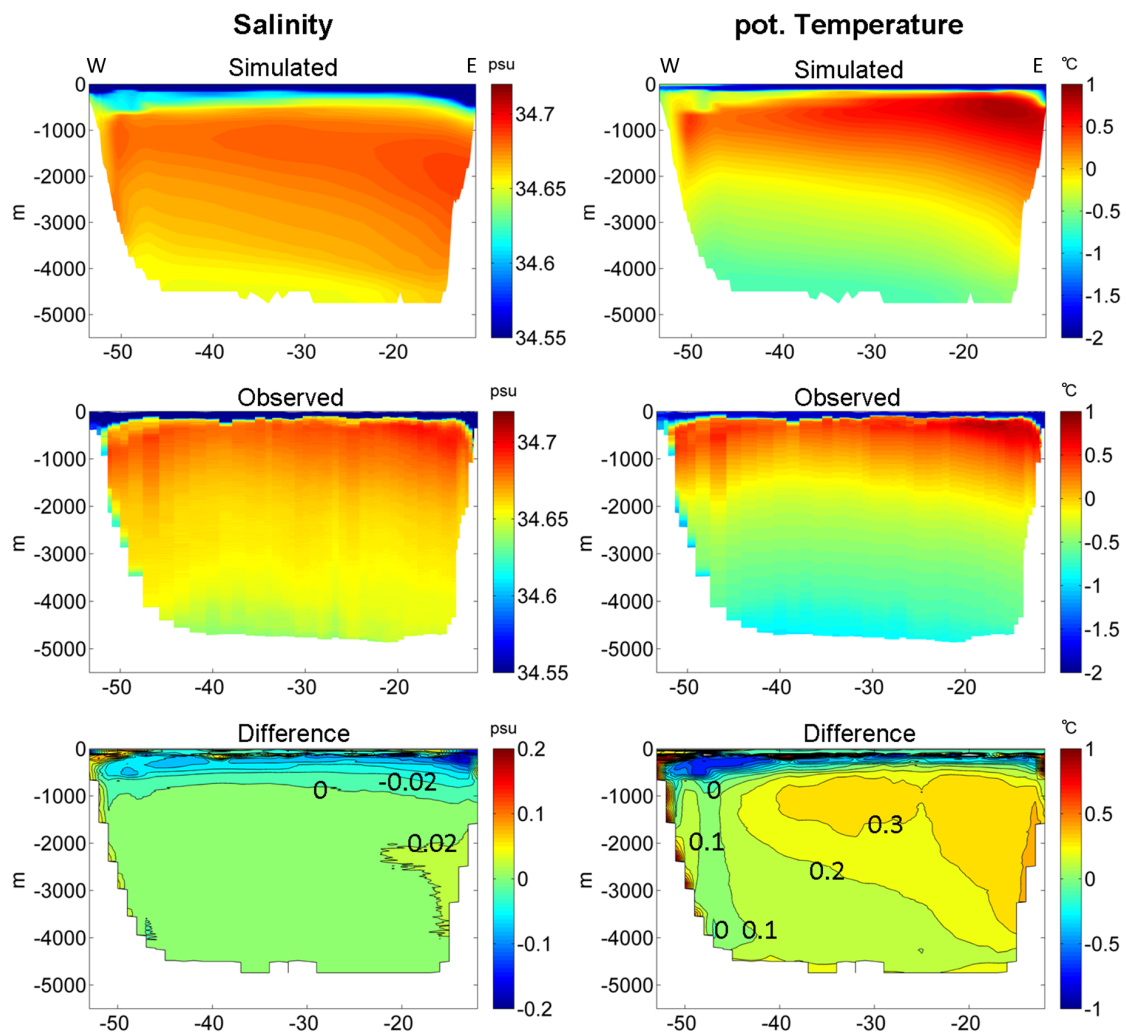


Figure 3.8: Salinity and temperature at Section S: Simulation and observation.

again rapidly and the onset of freezing, the associated brine release, and densification of the surface waters that causes deep convection restore the situation to a state very close to observations. The effect is especially visible in the 1998 profiles, since the summer of 1997/98 was characterised by an exceptionally large polynya in front of Ronne Ice Shelf that started opening already early in spring and increased over 3 months (Ackley et al., 2001).

Since this study concentrates on processes during winter, findings are not substantially affected by the shallow summer mixed layer. A comparison to winter CTD profiles is obstructed by the lack of observational data.

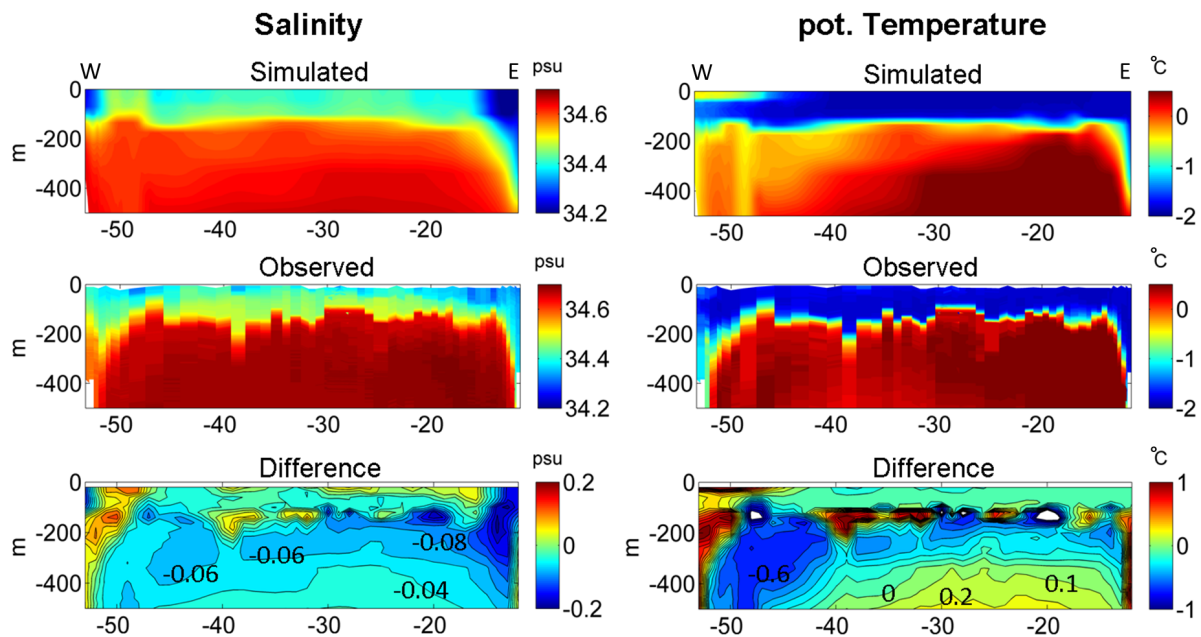


Figure 3.9: A more detailed view of salinity and temperature of the upper 500 m at Section S: Simulation and observation.

3.5 Temperature and salinity in the deep Weddell Sea

To give an impression of the model's representation of the Weddell Gyre and the water properties in the deep Weddell Sea, data from a section that connects Joinville Island located at the tip of the Antarctic Peninsula with Cape Norvegia at the eastern edge of Riiser-Larsen Isen (Figure 3.6), cutting through the western part of the Weddell Gyre, are presented. The observational data were acquired in November/December 1990 (Hellmer et al., 2011, Tables 3.2 and 3.3) and compared to a section from November 1999 of the simulation. This particular year was chosen since it is in the middle of the 20-year period used in data analysis in Chapters 4 and 5. All water masses mentioned here are defined in Section 1.2.2.

Both temperature and salinity at Section S exhibit good general agreement between simulation and observation (Figure 3.8). At the bottom we find temperatures of -0.9°C in the observations and -0.7°C in the simulation. The highest temperatures (0.8°C in both cases) are found on the eastern side of the section at depths of 200 m-400 m in the observation and 300 m-800 m in the modeled section. The simulated eastern temperature maximum of the WDW is slightly larger than observed and its western counterpart is cooler than observed.

Salinities at the bottom reach 34.64 in the observations and 34.65 in the simulation. The maximum salinities in both cases are close to 34.69 and located on the eastern side but while in the observations the maximum salinity is found right under the sharp halocline at 250 m to 800 m, the simulation features a few hundred meters of gradual increase in salinity under the thermocline and the maximum is placed at 1500 m-2500 m. Also at the lower boundary of the maximum, the observed salinity has much steeper gradients than the simulation.

The significantly colder and less saline bottom waters observed on the western continental slope are absent in the simulation. The main reason for this is the discretization of the model. The resolution is not high enough to preserve the properties of the dense water plumes. Every timestep the water entering a given element is mixed with the entire water volume of the element. The relatively small volume of dense water is therefore mixed into the WDW layer upon reaching the shelf break. This also explains the spuriously cold temperatures in the outflowing branch of WDW at depths of 150-500 m (Figure 3.9).

While the simulation during the investigated period is successful in the representation of the water masses entering the southwestern Weddell Sea, it cannot correctly reconstruct the path of the dense shelf water masses into the abyss. In Chapter 5, where the changes in water properties are discussed, I limit my considerations to processes and water masses on the continental shelf. However, an estimate of WSDW formation is added, in an effort to overcome the limitations of the simulation.

Station	Expedition	Date	Longitude	Latitude
PS18/039-1	ANTIX/2	1990-11-21	-52.9850	-63.3383
PS18/040-1	ANTIX/2	1990-11-21	-53.3350	-63.2667
PS18/041-1	ANTIX/2	1990-11-22	-52.5550	-63.4183
PS18/042-1	ANTIX/2	1990-11-22	-52.0900	-63.4917
PS18/043-1	ANTIX/2	1990-11-22	-51.3667	-63.6283
PS18/044-1	ANTIX/2	1990-11-23	-50.9250	-63.7550
PS18/045-1	ANTIX/2	1990-11-23	-50.0183	-63.8667
PS18/046-1	ANTIX/2	1990-11-24	-49.1533	-63.9500
PS18/047-1	ANTIX/2	1990-11-24	-47.5650	-64.2333
PS18/048-1	ANTIX/2	1990-11-24	-45.8100	-64.4083
PS18/049-1	ANTIX/2	1990-11-25	-44.2183	-64.6200
PS18/050-1	ANTIX/2	1990-11-25	-42.5083	-64.8200
PS18/051-1	ANTIX/2	1990-11-26	-40.7567	-65.0433
PS18/056-1	ANTIX/2	1990-11-28	-39.2967	-65.2800
PS18/057-1	ANTIX/2	1990-11-29	-37.9217	-65.4133
PS18/058-1	ANTIX/2	1990-11-29	-36.4767	-65.6383
PS18/059-1	ANTIX/2	1990-11-30	-35.4467	-65.7217
PS18/060-1	ANTIX/2	1990-11-30	-34.3500	-65.8300
PS18/061-1	ANTIX/2	1990-12-01	-33.5733	-65.9217
PS18/062-1	ANTIX/2	1990-12-01	-32.5467	-66.0550
PS18/063-1	ANTIX/2	1990-12-01	-31.7817	-66.1217
PS18/064-1	ANTIX/2	1990-12-02	-31.1450	-66.1833
PS18/065-1	ANTIX/2	1990-12-02	-30.2933	-66.2800
PS18/066-1	ANTIX/2	1990-12-02	-29.5350	-66.3617
PS18/067-1	ANTIX/2	1990-12-02	-28.7300	-66.4633
PS18/068-1	ANTIX/2	1990-12-02	-27.9817	-66.5167
PS18/069-1	ANTIX/2	1990-12-03	-27.1200	-66.6200
PS18/076-1	ANTIX/2	1990-12-05	-30.2967	-66.2900
PS18/083-1	ANTIX/2	1990-12-07	-26.3933	-66.7567
PS18/084-1	ANTIX/2	1990-12-07	-25.5567	-66.8900
PS18/086-1	ANTIX/2	1990-12-08	-24.1517	-67.2267
PS18/087-1	ANTIX/2	1990-12-08	-23.3233	-67.3650
PS18/088-1	ANTIX/2	1990-12-08	-22.5233	-67.5117
PS18/089-1	ANTIX/2	1990-12-09	-21.6617	-67.6650
PS18/090-1	ANTIX/2	1990-12-09	-20.8500	-67.8433
PS18/091-1	ANTIX/2	1990-12-09	-19.9700	-67.9883
PS18/092-1	ANTIX/2	1990-12-09	-19.3383	-68.2817
PS18/093-1	ANTIX/2	1990-12-10	-18.6183	-68.5533
PS18/094-1	ANTIX/2	1990-12-10	-17.9000	-68.8333
PS18/095-1	ANTIX/2	1990-12-10	-17.2633	-69.0767

Table 3.2: CTD-Stations used in the comparison of Section S (Section 3.5). Part I.

Station	Expedition	Date	Longitude	Latitude
PS18/096-1	ANTIX/2	1990-12-11	-16.4933	-69.3617
PS18/097-1	ANTIX/2	1990-12-11	-15.7267	-69.6583
PS18/098-1	ANTIX/2	1990-12-12	-15.2450	-69.8033
PS18/099-1	ANTIX/2	1990-12-12	-14.7033	-69.9683
PS18/100-1	ANTIX/2	1990-12-12	-14.2567	-70.1250
PS18/101-1	ANTIX/2	1990-12-12	-13.7033	-70.3083
PS18/102-1	ANTIX/2	1990-12-13	-13.5417	-70.3833
PS18/103-1	ANTIX/2	1990-12-13	-13.2950	-70.4200
PS18/104-1	ANTIX/2	1990-12-13	-13.1367	-70.4950
PS18/105-1	ANTIX/2	1990-12-13	-12.7350	-70.6383
PS18/106-1	ANTIX/2	1990-12-13	-12.3617	-70.7933
PS18/108-1	ANTIX/2	1990-12-14	-11.8367	-70.9917
PS18/109-1	ANTIX/2	1990-12-14	-11.9417	-70.9067
PS18/113-1	ANTIX/2	1990-12-15	-11.7483	-70.9933
PS18/114-1	ANTIX/2	1990-12-15	-11.7067	-71.0500
PS18/115-1	ANTIX/2	1990-12-15	-11.3867	-71.1133

Table 3.3: CTD-Stations used in the comparison of Section S (Section 3.5). Part II.

4 Heat flux and sea ice production

The following chapter presents processes at the ocean and ice surfaces. First the mean seasonal cycle is investigated. For this purpose, a reference area was defined by the introduction of a boundary line that follows the Section S (Figure 3.6) from Cape Norvegia to Joinville Island but is cut off at 67° S to eliminate the year-round occurrences of open water at the tip of the Antarctic Peninsula. This region will be referred to as Southwestern Weddell Sea (Figure 4.1).

An evaluation of the spatial distribution of heat flux and sea ice production in the winter months follows and three more regions of interest are introduced. The winter heat fluxes to the atmosphere and the share compensated by ocean cooling as well as the resulting sea ice production in those regions are presented and discussed. The chapter closes with a short summary.

4.1 Seasonal cycle in the southwestern Weddell Sea

In this section the average seasonal cycle (monthly means over the years 1990-2009) of sea ice coverage, heat and fresh water flux in the Southwestern Weddell Sea and its polynyas is presented and discussed. The monthly values depicted in Figure 4.2 were collected as daily averages over the corresponding area, which then were averaged over the 20 different years for each month.

For practical reasons, all areas with a sea ice concentration of less than 70% are called polynyas here, even though in the summer months they might be connected to the open ocean and the definition for coastal polynyas (latent heat polynyas) might not strictly apply since no ice is formed.

In summer the heat exchange with the atmosphere in the Southwestern Weddell Sea results in a substantial heat gain for the system of ocean and sea ice with a maximum of 51 W/m^2 in January (Figure 4.2, first upper panel). March, however, brings a sign change and initiates a period of high heat loss of the sea ice-ocean system to the atmosphere, which in April reaches its maximum (76 W/m^2) and thereafter slowly but steadily decreases over the winter months to turn into heat gain again in November and as such increases until January. Much

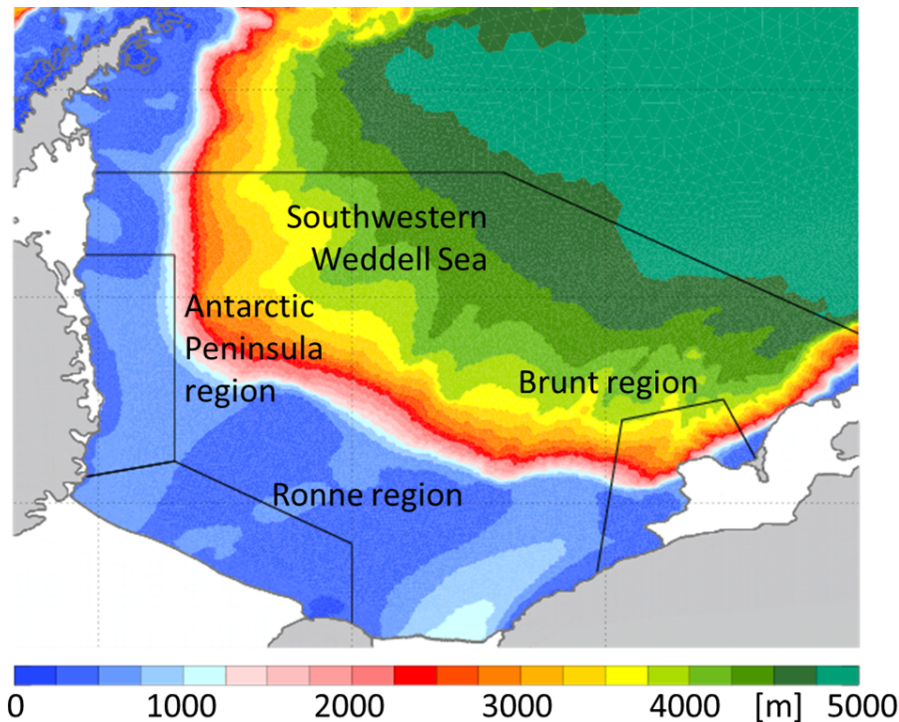


Figure 4.1: Map showing the boundaries of the Southwestern Weddell Sea and Brunt, Ronne and Antarctic Peninsula regions.

of the energy gained in summer is taken up by ice melt, but also the surface waters experience warming. In autumn, the sun's descent and decreasing air temperatures induce a sign change in the surface heat budget and large areas of open water (Figure 4.2, third upper panel) give rise to an unobstructed heat flux from the ocean to the atmosphere. During the winter, the increasing ice cover leads to a gradual decrease of the heat flux. Eventually, the increasing solar angle and the rising air temperatures cause the sign to change back in November.

Over polynyas we find the same sign changes in the course of the year but usually higher heat flux values due to the sparse sea ice cover and therefore a higher surface temperature in winter and a much lower albedo in the summer. In contrast to the basin-wide average, the heat flux in the polynya area does not peak in autumn but rises to values $>410 \text{ W/m}^2$ in the mid-winter months June-August, since here the ice cover that usually obstructs the heat flux in winter is steadily exported. The maximum downward heat flux over polynyas (164 W/m^2) is found in December, because the low albedo gives a stronger emphasis to the month with the highest insolation.

The oceanic heat flux, the heat exchange between the ocean and the sea ice and atmosphere, is negative (downward) during the summer (Figure 4.2, bottom left panel), i.e. heat

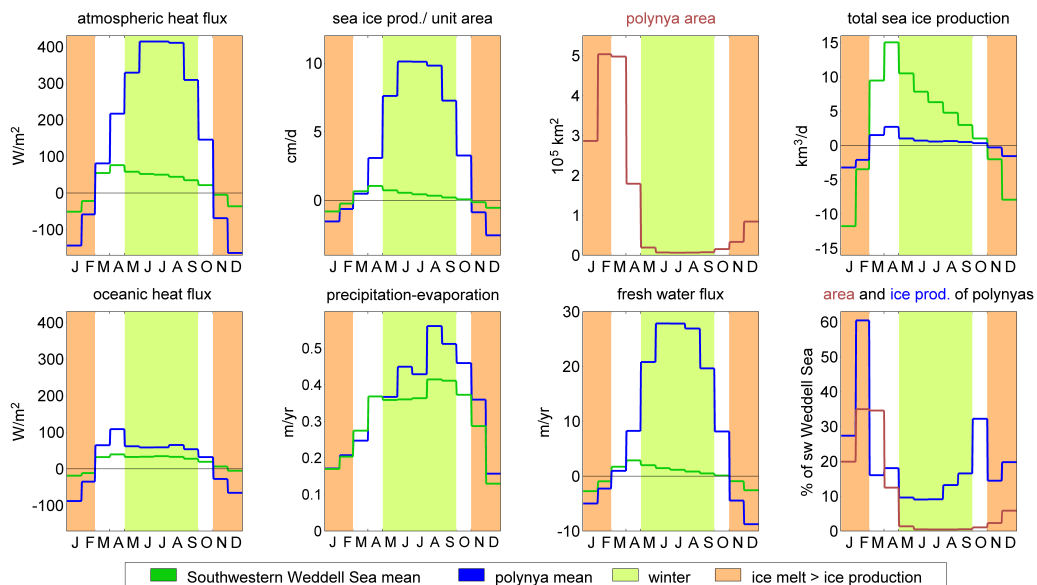


Figure 4.2: Monthly 20-year mean of atmospheric heat flux, oceanic heat flux, sea ice production, net precipitation, polynya area and upward fresh water flux in the Southwestern Weddell Sea and within its polynyas, averaged from daily values. Time period considered: 1990-2009

is gained by the ocean. The maximum is found in January, when also the heat gain from the atmosphere is highest. The onset of freezing conditions in March brings the sign change toward a persistent heat loss of the ocean with $\approx 33 \text{ W/m}^2$ until August and a maximum of 39 W/m^2 in April, when oceanic heat content gained during summer is eroded with the onset of convection. Naturally, the heat loss of the ocean is limited to the heat surplus of the surface layer (relative to its heat content at freezing point temperature). Once the surface waters are at freezing temperature, convective or advective transport of warmer water is necessary to uphold oceanic heat flux. The residual heat required to meet the atmospheric heat flux is gained by latent heat release in the process of sea ice formation. The April maximum in oceanic heat flux is the result of enhanced convection due to the maximum in atmospheric heat flux and the ensuing maximum in sea ice production. After August, the oceanic heat flux decreases slowly, but in the basin-wide mean the ocean still loses heat in November, followed by a small heat gain in December.

At polynyas the oceanic heat flux is higher than in the Southwestern Weddell Sea mean. Due to the reduced or removed ice cover the albedo of polynyas (0.1) is far lower than the albedo of ice (0.68-0.75) or snow (0.77-0.85) covering the ocean. In summer, the enhanced (downward) oceanic heat flux at polynyas is caused by the almost unhindered uptake of

shortwave radiation. In the winter months, the high heat loss to the atmosphere induces sea ice formation, which triggers convection by brine release, enabling a strong upward oceanic heat flux. Within polynyas, we find a persistent oceanic heat flux of $\approx 60 \text{ W/m}^2$ until the end of winter, again with a distinct maximum in April (108 W/m^2), when convection has started and the water still has a substantial heat content after the summer months. The decrease of oceanic heat flux in spring is more abrupt at polynyas than in the basin-wide mean and the ocean takes up heat already in November, since only a small fraction of the heat from the atmosphere is taken up by the sparse sea ice then.

The difference between atmospheric and oceanic heat flux is gained in the formation or used in the melting of sea ice. Net sea ice production of the Southwestern Weddell Sea (Figure 4.2, second upper panel) is negative during the summer with a maximum of melting in January (-0.82 cm/d). The sign turns positive for March and the rapid cooling of the atmosphere in autumn brings strong heat loss from the ocean and high ice production that reaches its maximum in April (1.04 cm/d). Due to the increasing ice cover inhibiting the ocean-atmosphere heat exchange the ice production decreases over the season until in November melting takes over again, when with the increasing solar angle the ocean experiences a net heat gain. The receding ice cover changes the albedo of the area and creates a positive feedback to the melting process.

In contrast to the basin-wide mean, the ice production rate in polynyas features a maximum in June and July (10 cm/d), closely followed by August. The highest melting rate is in December (-2.6 cm/d). The onset of freezing in polynyas does not immediately induce high freezing rates; in March the ice production in polynyas is lower than the southwestern Weddell Sea average. This is due to the warming of the polynya surface waters over summer, which is probably overestimated. Temperatures first have to be brought down to the freezing point before extensive freezing can begin. Since they are not shielded from the atmosphere by a growing layer of sea ice, polynyas feature freezing rates that peak in midwinter and reach much higher values than in the ice-covered ocean. The ratio between both rates increases over the season until it hits a high point in September with polynya freezing rates exceeding southern Weddell Sea rates by a factor of ≈ 34 .

The volume of sea ice that is formed is a product of the sea ice production per unit area and the corresponding area. While the area of the Southwestern Weddell Sea is constant and the shape of the resulting curve is the same as for the Southwestern Weddell Sea ice production per unit area, the area of its polynyas changes with the seasons (Figure 4.2, third upper panel). Due to the low albedo, heat uptake by shortwave radiation is augmented in polynya areas and leads to strong summer melting. With the advance of the spring/summer season, the polynya area increases and is often connected to the open ocean. The polynya area in

the Weddell Sea is largest in February ($5 \cdot 10^5 \text{ km}^2$) with March as a close second. After March, the polynya area decreases fast and in the months June to September varies between 6000 km^2 and 7000 km^2 . October brings a first slow but notable increase in polynya area that is amplified in the following months until, again, the maximum area is reached in February.

The volume of sea ice produced in polynyas (Figure 4.2, top right panel) is much smaller than the total volume of sea ice produced in the Southwestern Weddell Sea. The highest absolute values ($-3.2 \text{ km}^3/\text{d}$) are found in the summer's sea ice melt, when the 'polynya' area is large and the heat uptake of the open water area furthers the melting process, and the following freeze-up in autumn (April: $2.7 \text{ km}^3/\text{d}$), when the open water area still is large. From April to May the produced sea ice volume is almost cut to a third due to the drop in polynya area, despite the increase in ice production per unit area. Over the winter months follows a steady decrease, until ice starts to melt in November.

When looking at polynya sea ice production and polynya area as percentiles (Figure 4.2, bottom right panel), ice production always exceeds the areal fraction of polynyas with the exception of March. Please be reminded that the summer months show melting. March is the first month of freezing, meaning that all areas, which were left with ice concentrations below 70 % by the summer ice melt are counted as polynyas, although strictly the term might not apply. Partly, these areas were subject to substantial warming during the summer, so that the temperature first has to be lowered to the freezing point by heat transfer to the atmosphere, before ice formation can start. Thus, the areas called polynyas here exhibit a delayed refreezing in early autumn, especially since summer warming and melting appear to be overestimated by the model (cf. Section 3.4). This circumstance should also be kept in mind when looking at February, when the polynya contribution has its maximum with 60 % of the ice melt. While the characteristic in all probability is true, the extent is likely to be overstated.

In May, the polynya area has dropped to very low values (1.3 %), now describing only areas that also in the strict sense of the words classify as coastal polynyas. The relative production of sea ice is at a level of $\approx 9 \%$ and remains there for two more months while polynya area drops even farther to $\approx 0.5 \%$, where it stays until October. The fraction of polynya sea ice production increases during August and September because sea ice production of the ice-covered southwestern Weddell Sea is continually decreasing. While in October polynya areas slightly increase, which is a first sign of the arrival of spring, the polynyas still extend their relative ice production, because ice production for the entire southwestern Weddell Sea has decreased to a very low value due to the large mean ice thickness and the polynyas on average are located far south, where air temperatures are colder.

Sea ice production is the dominant process for the fresh water flux in the southwestern

Weddell Sea. The net precipitation (precipitation-evaporation, Figure 4.2, second lower panel), which is of great importance in lower latitudes, is two orders of magnitude smaller than the fresh water flux associated with sea ice production. It has its highest values in winter, when evaporation is smallest due to the low air temperatures. Also in winter polynyas feature higher values than the basin-wide mean, since here only a very small fraction of the precipitating water falls on sea ice, where it adds to the snow cover.

The seasonal cycle of the fresh water flux (Figure 4.2, third lower panel) therefore resembles the sea ice production very closely in shape. The mean over the Southwestern Weddell Sea features a maximum of 2.9 m/yr (0.79 cm/d) in April and a minimum of -2.7 m/yr (-0.74 cm/d) in January. The mean freshwater flux within the polynyas gives a maximum of 27.8 m/yr (7.6 cm/d) in June and a minimum of 8.8 m/yr (2.4 cm/d) in December. For the remainder of this Chapter, the fresh water flux will not be considered separately because the sea ice production per unit area serves as a good proxy in the winter.

During the months May to September, the areas with sea ice concentration below 70 % meet the requirements of coastal polynyas, i. e. small coastal areas are held ice-free by offshore winds and feature high heat fluxes and strong sea ice formation. In April, the polynya area is still so large that one must consider it a refreezing ocean rather than an ice-covered ocean where winds create small areas of low ice concentration. In October a small but significant increase in polynya area already announces spring. In the following sections I will therefore refer to the period from May to September when speaking of winter and restrict most observations of polynya characteristics to these 5 months.

4.2 Spatial distribution during the winter months

In the following section, maps of winter mean values of sea ice concentration, atmospheric and oceanic heat fluxes and sea ice production for the southwestern Weddell Sea are discussed. Based on the findings, three regions of interest are defined.

4.2.1 Multi-year mean fields

A map of mean winter sea ice concentration (Figure 4.3) shows most of the area of the southwestern Weddell Sea with ice concentrations between 95-100 %. The few areas that feature lower values of sea ice concentration are areas where recurrent polynyas form. Since even recurrent coastal polynyas open only episodically, usually for a few days, at no location within the southwestern Weddell Sea the concentration drops below 0.55 in the winter mean. From the tip of the Antarctic Peninsula southward very low sea ice concentrations are found. The model overestimates the extent of these polynya areas; a deficiency that is attributed to

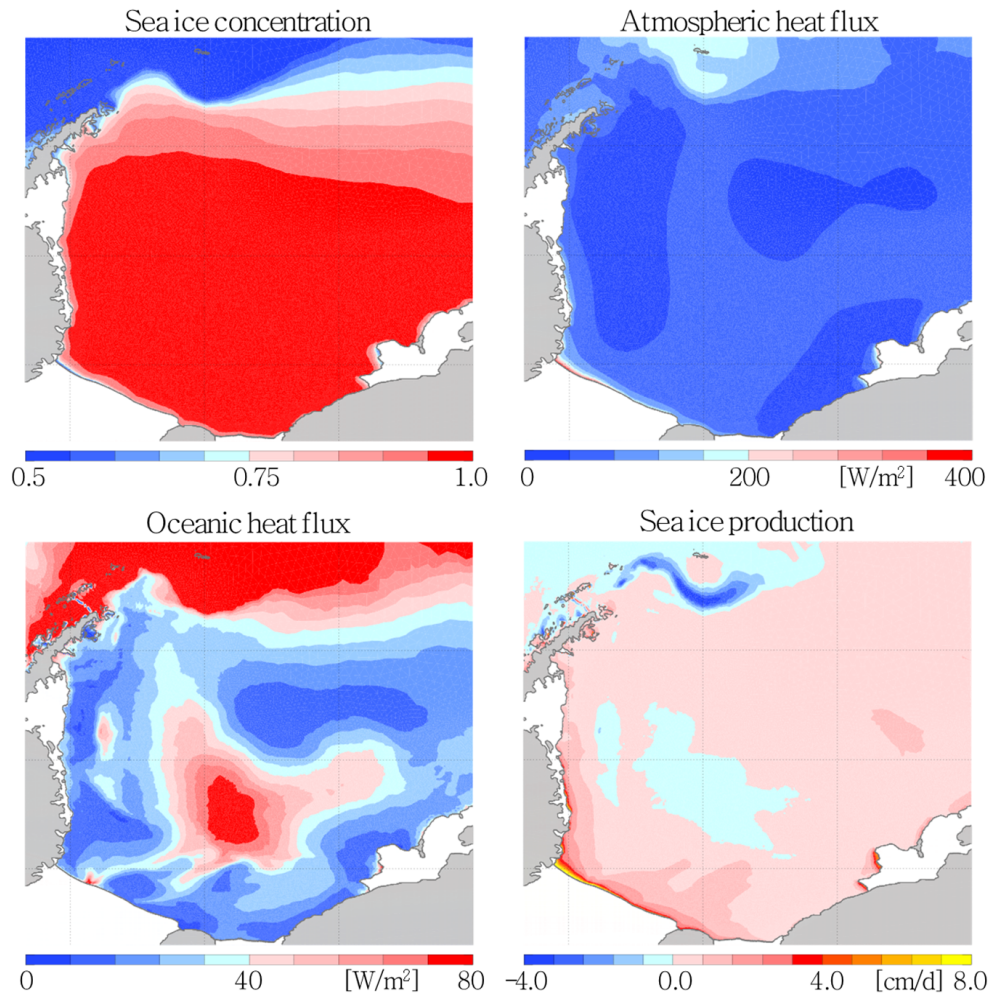


Figure 4.3: 20-year winter mean of sea ice concentration, atmospheric heat flux, oceanic heat flux and sea ice production in the southwestern Weddell Sea (May-September 1990-2009)

the fact that the NCEP/NCAR Reanalysis model, which provides the atmospheric forcing data, contains a strongly smoothed representation of the topography of the Antarctic Peninsula. Thus, wind speeds across the peninsula are overestimated (Windmüller, 1997). This underestimation of sea ice concentration along the northern end of the Antarctic Peninsula coastline was crucial in the decision to restrict the area of the Southwestern Weddell Sea to the area south of 67° S.

The southern part of the peninsula shows a somewhat narrower belt of reduced ice concentrations. This belt widens a little in the southwestern corner between the peninsula and Ronne Ice Shelf. From there along the Ronne Ice Shelf, we find the lowest ice concentration values in the southwestern Weddell Sea. The polynya activity diminishes again toward the

east and while the band continues along the shore of Berkner Island and the front of Filchner Ice Shelf it continually narrows. The coastline of Coats Land only shows very weak signs of polynya activity, but off Brunt Ice Shelf two areas of considerably reduced sea ice concentrations can be found at parts of the coastline that face to the west. We also find evidence of recurring polynyas along the front of Riiser Larsen Isen, although less intense than the polynyas at Brunt Ice Shelf.

Since the heat exchange between ocean and atmosphere is inhibited by the presence of sea ice, the atmospheric heat flux (Figure 4.3, top right panel) has a pattern very similar to the sea ice concentration. Most of the southwestern Weddell Sea loses less than 80 W/m^2 . At the coastline of the southern part of the Antarctic Peninsula and in the polynyas at Brunt Ice Shelf the heat flux is enhanced to values between 200 and 300 W/m^2 while at the western Ronne Ice Front values almost reach 400 W/m^2 as a mean heat flux in the winter months.

The oceanic heat flux (Figure 4.3, bottom left panel) features a distinct maximum ($\approx 80 \text{ W/m}^2$) near the shelf break of the southern continental shelf. This maximum, created by the atmospheric heat flux pattern, the availability of warm subsurface waters and a cyclonic wind pattern facilitating upwelling, has trails reaching onto the continental shelf along the topographic features of Berkner Bank and Belgrano Bank. These intrusions of relatively warm water ($\approx -1 \text{ }^\circ\text{C}$) onto the continental shelf lose intensity with distance from the shelf break, but where one of them reaches the area of the Ronne polynya, the enhanced atmospheric heat flux and the convection induced by sea ice production give rise to a further maximum of the oceanic heat flux, which is small in extent but intense (again $\approx 80 \text{ W/m}^2$). Another maximum ($\approx 55 \text{ W/m}^2$) is found further north off the western continental shelf and is caused by the upwelling of warmer waters at the continental slope which – like the strong maximum off the southern shelf – imprints itself as a local minimum of sea ice production.

While along the southern part of the peninsula and the Ronne Ice Front the freezing rates gradually decrease with distance from the coastline, sea ice production in front of Brunt Ice Shelf (5.6 cm/d) features sharper boundaries. We find freezing rates up to 6.5 cm/d at the peninsula and 7.5 cm/d at Ronne Ice Shelf. A small enhancement of freezing rates can be observed above Berkner Bank, which is due to the low water column depth that facilitates a faster cooling of the water column to the freezing point.

4.2.2 Regions of interest

Three regions with high polynya activity were chosen for further analysis (Figure 4.1). The Brunt region covers the eastern polynyas next to Brunt Ice Shelf. Its boundaries are defined by the corner coordinates $31^\circ \text{ W}/78^\circ \text{ S}$, $29^\circ \text{ W}/73^\circ \text{ S}$, $23^\circ \text{ W}/72.5^\circ \text{ S}$ and $21^\circ \text{ W}/74^\circ \text{ S}$.

The Ronne region encloses the front of the Ronne Ice Shelf where the highly active Ronne polynya is located. In the Ronne polynya we find the highest heat flux and sea ice production. The region's corners are given by the following coordinates: $45^\circ \text{ W} / 78.5^\circ \text{ S}$, $69.5^\circ \text{ W} / 75^\circ \text{ S}$, $55.5^\circ \text{ W} / 74^\circ \text{ S}$ and $45^\circ \text{ W} / 76^\circ \text{ S}$. The Antarctic Peninsula region comprises all polynyas along the coastline of the southern part of the Antarctic Peninsula. Its extent is given by the corners $65^\circ \text{ W} / 69^\circ \text{ S}$, $55.5^\circ \text{ W} / 69^\circ \text{ S}$, $55.5^\circ \text{ W} / 74^\circ \text{ S}$ and $62.5^\circ \text{ W} / 74.5^\circ \text{ S}$. In Section 4.3, I will present, discuss and compare mean values of polynya area, heat flux and sea ice production in these regions.

4.3 Regional characteristics

4.3.1 Polynya area

The Brunt region (Figure 4.1) has a 20-year mean polynya size of 1013 km^2 during winter (averaged over all days May-September). In the Ronne region, coastal polynyas on average cover an area of 1998 km^2 in winter, which is twice the size of the Brunt polynyas. The Antarctic Peninsula region features a mean winter polynya size of 1712 km^2 . For the entire Southwestern Weddell Sea the 20-year mean polynya area is 9000 km^2 .

Over the years 2003-2009 (chosen due to the availability of the data) a comparison of the simulated polynya area to the polynya area derived with the criterion of 70 % ice concentration from AMSR-E data (Spren et al., 2008) shows that the simulated polynya size is smaller by 40 % in the Brunt region and by 30 % in the Ronne region, while in the Antarctic Peninsula region the simulated polynyas exceed the satellite-derived area by 68 %. On a basin-wide scale the various regional differences between polynyas from the AMSR-E data and the simulation compensate each other very well (as the comparisons in Chapter 3.2 already indicated) and the simulation underestimates the observation-derived value of coastal polynya area by only 10 %.

As already mentioned, the overestimation of polynya size at the peninsula can largely be attributed to the fact that the westerly winds in the NCEP/NCAR Reanalysis across the Antarctic Peninsula are overestimated due to the coarse representation of the topography in the employed model (Windmüller, 1997; Stössel et al., 2011), while observations indicate that the wind field east of the peninsula is often dominated by barrier winds (Schwerdtfeger, 1975; Parish, 1983).

The underestimation of polynya area in the Ronne region may be related to the fact that in reality iceberg A23 shields the region from sea ice advection from the east and thus allows for more frequent and larger polynyas (Markus, 1996). Also, the coarse temporal resolution

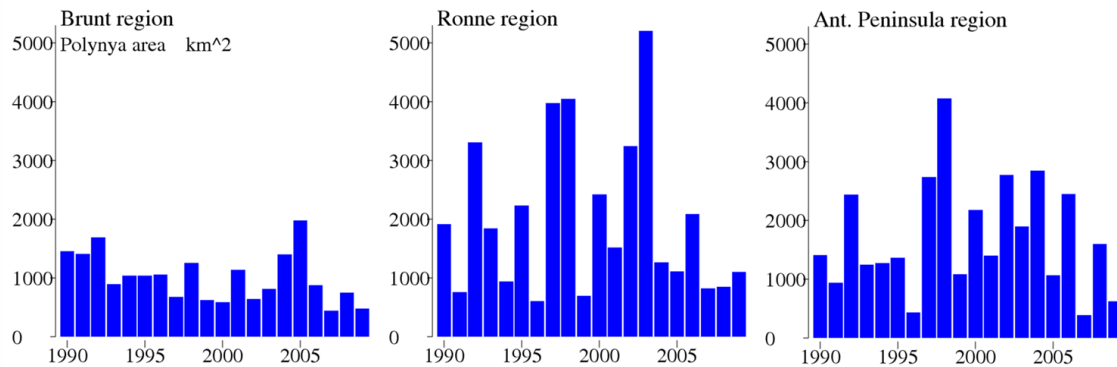


Figure 4.4: Simulated winter (May-September) mean polynya area in the three regions.

of the NCEP forcing data results in an underestimation of peak wind velocities (Ernstorf et al., 2011), which also leads to smaller polynyas at Brunt and Ronne Ice Shelf.

Interannual variability of polynya area is very pronounced (Figure 4.4). Seasonal means of half or twice the long-term mean are not uncommon. The range of polynya area in Brunt region spans from 440 to 2000 km², which is rather moderate compared to the range in Ronne region (600-5200 km²) and at the Antarctic Peninsula (390-4100 km²). However, also these are (seasonally) averaged numbers and on a daily scale values can still differ far from them. Daily values feature maxima of 8000 km² in the Brunt region and 30000 km² in both the Ronne and the Antarctic Peninsula regions.

4.3.2 Atmospheric heat flux

Multi-year mean within polynyas

During winter (May-September), the 20-year mean heat flux to the atmosphere equals 311 W/m² in the polynyas of the Brunt region. The Ronne polynyas feature a mean of 511 W/m² and in the Antarctic Peninsula region the mean winter heat flux is 364 W/m². The annual mean values (Figure 4.5, upper panels) and the standard deviations from the multiyear mean are found in Table 4.1. If all polynyas in the Southwestern Weddell Sea are considered, the mean winter heat flux to the atmosphere is 368 W/m². These mean values are calculated considering only the days when a polynya is present, thus they represent the mean flux that can be expected over a polynya in the corresponding region.

As might be expected during the winter months May-September, the shortwave radiation is the smallest of the atmospheric heat flux components. Given that we define upward fluxes to have a positive sign and the reflected upward shortwave radiation is a fraction of the downward shortwave radiation, the net shortwave radiation must always be a negative number.

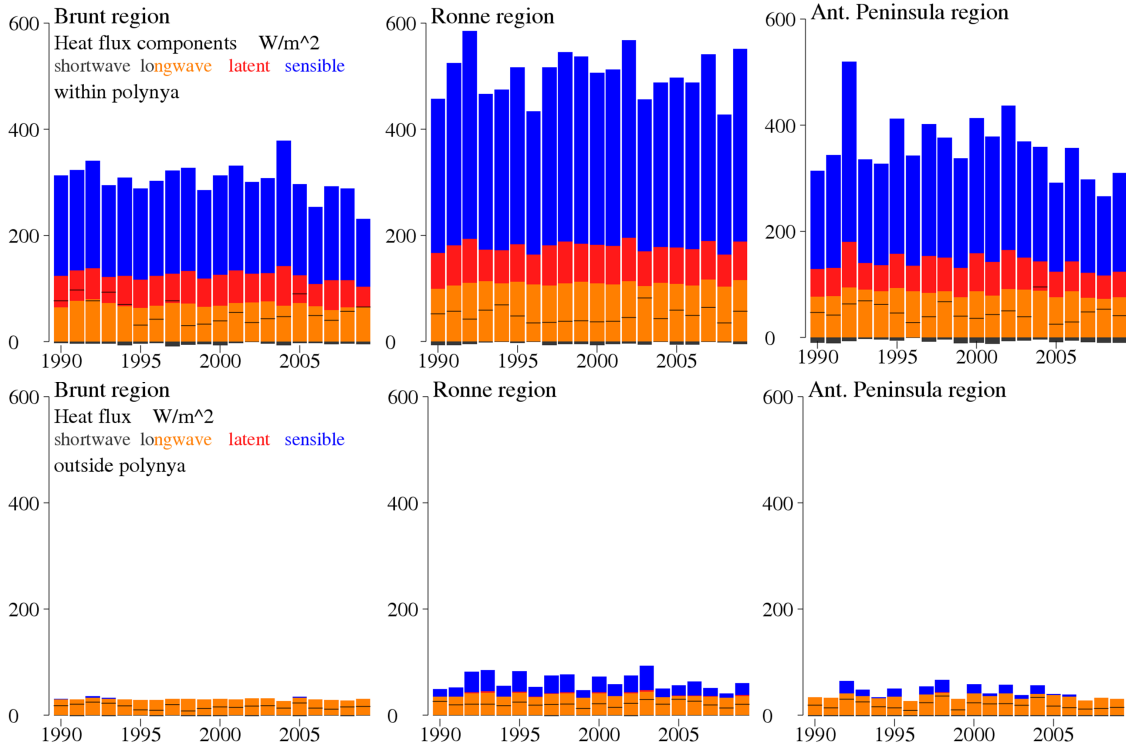


Figure 4.5: Simulated winter (May-September) mean of the atmospheric heat flux over polynyas in the three regions. The grey color represents the net shortwave radiation (negative values). Since the components are summed up and the entire column length gives the heat flux to the atmosphere, the length of the grey and yellow column parts together represents the net longwave radiation, the red part is the latent and the blue part the sensible heat flux. The small black lines mark the oceanic heat flux, i.e. the heat flux not compensated by sea ice formation but by cooling the water column.

The shortwave radiation has an average of -4.7 W/m^2 at the Brunt polynyas, -4.5 W/m^2 at Ronne polynya and -7.7 W/m^2 at the polynyas along the Antarctic Peninsula (which are located slightly further north on average). The longwave radiation features a winter mean of 74 W/m^2 over the Brunt polynyas, 114 W/m^2 over Ronne polynya and 91 W/m^2 over the Antarctic Peninsula polynyas. The latent heat flux provides a slightly smaller contribution: 55 W/m^2 in the Brunt region, 70 W/m^2 in the Ronne region and 58 W/m^2 in the Antarctic Peninsula region. The simulated 20-year winter mean of the sensible heat flux over polynyas is 181 W/m^2 in the Brunt region, 325 W/m^2 in the Ronne region and 218 W/m^2 in the Antarctic Peninsula region. The heat flux components were calculated using a mean surface temperature of the sea ice (for every single element). The total of the atmospheric heat flux was calculated using seven different ice thickness classes (average over the heat flux for seven equidistant ice thicknesses from $\frac{h_i}{7}$ to $\frac{13h_i}{7}$). Therefore, small differences ($< 5\%$)

Table 4.1: Annual and 20-year winter mean of atmospheric heat flux and ice production of the polynyas in Brunt, Ronne and Antarctic Peninsula (Ant. P.) region. Minimum and maximum values for each column are printed in bold font.

Year	atm. heat flux [W/m ²]			oceanic heat flux [W/m ²]			sea ice prod. [cm/d]			integr. ice prod. [km ³]		
	Brunt	Ronne	Ant. P.	Brunt	Ronne	Ant. P.	Brunt	Ronne	Ant. P.	Brunt	Ronne	Ant. P.
1990	324	467	323	77	52	47	7.0	11.8	7.8	17.5	35.6	13.1
1991	331	535	358	97	57	42	6.6	13.6	9.0	16.5	17.7	17.1
1992	348	590	509	77	42	63	7.7	15.6	12.7	21.9	81.6	40.6
1993	295	463	329	93	59	69	5.7	11.5	7.4	9.9	37.4	13.9
1994	314	454	329	70	69	62	6.9	10.9	7.6	12.1	21.8	14.9
1995	306	508	392	31	48	46	7.8	13.1	9.8	13.8	52.3	14.6
1996	295	443	336	42	35	28	7.2	11.6	8.8	14.2	12.6	7.3
1997	324	528	410	77	36	39	7.0	14.0	10.5	8.9	84.4	40.5
1998	328	550	389	30	38	67	8.5	14.6	9.2	18.0	88.8	47.1
1999	294	547	347	33	39	40	7.4	14.4	8.7	8.6	18.6	15.5
2000	316	511	419	39	37	36	7.9	13.5	10.9	8.2	55.4	28.6
2001	349	521	390	55	38	43	8.4	13.7	9.9	17.5	38.0	14.2
2002	308	575	442	36	45	50	7.7	15.1	11.1	9.2	80.1	38.6
2003	309	467	376	43	82	39	7.6	10.9	9.6	11.2	86.0	24.0
2004	385	500	364	47	43	95	9.6	13.0	7.7	22.8	28.3	32.5
2005	307	507	292	90	59	25	6.2	12.7	7.6	18.0	24.4	10.6
2006	264	501	365	49	49	29	6.1	12.8	9.6	10.9	46.8	24.4
2007	298	550	304	40	64	48	7.4	13.8	7.3	5.2	20.3	3.1
2008	297	437	278	57	35	53	6.8	11.4	6.4	10.0	18.5	14.1
2009	237	566	320	65	57	41	4.9	14.5	7.9	4.5	27.8	5.4
mean	311	511	364	57	49	48	7.22	13.1	9.0	12.9	43.8	21.0
stddev.	± 31	± 45	± 55	± 22	± 13	± 17	± 1.0	± 1.4	± 1.6	± 5.2	± 26.6	± 12.9

between the sum of the heat flux components and the atmospheric heat flux occur.

In all polynyas, the winter heat flux and its variability are dominated by the sensible heat transfer, which contributes 59-64 % of the total heat flux. This fraction, as well as the relative contributions of latent and radiative heat fluxes, is in very good agreement with the findings of Renfrew et al. (2002) during high-winter (June-July 1998).

The 20-year mean of heat gained by the atmosphere over the polynyas during the months May-September is $4.7 \pm 2.0 \cdot 10^{18}$ J in the Brunt region, $14.7 \pm 9.0 \cdot 10^{18}$ J in Ronne region and $7.7 \pm 4.8 \cdot 10^{18}$ J in Antarctic Peninsula region. Over the coastal polynyas of the entire Southwestern Weddell Sea, the atmosphere gains $4.0 \pm 1.6 \cdot 10^{19}$ J during the winter months. Renfrew et al. (2002) estimated the mean heat gain by the atmosphere at Ronne polynya during the freezing season for the period 1992-1998 to be $3.48 \pm 0.98 \cdot 10^{19}$ J. In their study, Renfrew et al. (2002) defined the duration of the freezing period individually for every year. For the same time frame, our simulation yields an atmospheric heat gain of

$3.76 \pm 1.14 \cdot 10^{19}$ J, which is in good agreement and underlines the importance of a careful consideration of the time frame any estimate represents. Further comparisons of our results with independent studies are found in Section 4.3.4 about sea ice production.

Multi-year mean outside polynyas

To assess the importance of polynyas compared to the ambient pack ice in terms of heat transferred to the atmosphere, the heat flux outside the polynyas in the three regions (Figure 4.5, lower panels) is calculated. For the area with ice concentrations higher than 70 % the mean winter heat flux is 30 W/m^2 in the Brunt region, 70 W/m^2 in the Ronne region and 46 W/m^2 in the Antarctic Peninsula region, which is only 10-14 % of the heat flux within polynyas, but due to the much larger area it gives an atmospheric heat gain of $8.7 \pm 1.2 \cdot 10^{20}$ J/season in the Southwestern Weddell Sea.

In the Brunt region most heat flux components are negligible outside the polynyas and the longwave radiation is responsible for almost all the heat transferred to the atmosphere with an average of 31 W/m^2 . The latent heat flux over ice gives a small negative contribution (mean: -4.0 W/m^2), which corresponds to resublimation of atmospheric humidity. In the Ronne region, due to the very low air temperatures, the sensible heat flux (mean: 26 W/m^2) is of similar magnitude as the net longwave radiation (mean: 39 W/m^2). The remaining heat flux components are negligible, however, the latent heat flux is positive (upward) here. At the Antarctic Peninsula the heat flux over high ice concentration areas is mainly due to the longwave radiation (mean: 37 W/m^2) although in years with low temperatures and strong winds the sensible heat flux can substantially add to this (mean: 9.1 W/m^2). The modelled latent heat flux transfers heat downward out of the atmosphere at a rate of 1.8 W/m^2 .

Interannual variability within polynyas

Compared to the strong interannual variability found for the polynya area (Figure 4.4), interannual variability of the atmospheric heat flux (averaged over polynya days) (Figure 4.5) is much smaller and so is the variability of the key parameters air temperature, wind speed and specific humidity (Figure 4.6). A compilation of annual maximum and minimum values, multiyear mean and standard deviation of these three forcing parameters is given in Table 4.2.

For the Brunt polynyas, we find the highest winter heat flux to the atmosphere in 2004 (385 W/m^2) and the lowest atmospheric heat flux in 2009 (237 W/m^2). Air temperature, wind speed and specific humidity feature 20-year winter means of $-20.7 \text{ }^\circ\text{C}$, 6.5 m/s and 0.83 g/kg , respectively. For 2004, neither of these exhibit extraordinary values in the winter mean

Table 4.2: Annual and 20-year winter mean of wind speed, air temperature and specific humidity in Brunt, Ronne and Antarctic Peninsula region. Minimum and maximum values for each column are printed in bold font.

Year	wind speed [m/s]			air temperature [°C]			specific humidity [g/kg]		
	Brunt	Ronne	Ant. P.	Brunt	Ronne	Ant. P.	Brunt	Ronne	Ant. P.
1990	5.36	3.99	5.79	-23.4	-32.8	-23.3	0.71	0.39	0.72
1991	5.30	3.68	5.76	-22.4	-34.5	-25.7	0.77	0.31	0.62
1992	4.77	4.84	7.98	-24.5	-36.1	-24.7	0.62	0.27	0.60
1993	3.98	4.06	4.96	-26.9	-37.1	-25.9	0.53	0.23	0.57
1994	5.08	3.99	5.12	-23.4	-33.8	-25.2	0.72	0.33	0.64
1995	4.79	4.38	6.01	-24.1	-36.0	-26.1	0.70	0.24	0.53
1996	4.80	3.96	4.24	-23.0	-33.4	-24.4	0.71	0.32	0.66
1997	4.15	4.74	6.58	-25.2	-34.0	-23.6	0.57	0.32	0.71
1998	5.27	5.02	6.79	-22.4	-32.5	-23.6	0.77	0.32	0.68
1999	4.04	3.88	4.78	-24.3	-34.2	-23.4	0.65	0.35	0.73
2000	4.11	4.49	6.03	-25.0	-34.6	-23.7	0.61	0.29	0.63
2001	5.74	4.70	6.40	-22.1	-31.7	-23.8	0.77	0.37	0.67
2002	4.20	4.94	6.91	-25.1	-34.6	-22.8	0.66	0.30	0.68
2003	4.34	5.09	6.08	-24.4	-32.8	-23.3	0.69	0.33	0.65
2004	6.24	4.14	5.99	-21.8	-31.6	-23.5	0.78	0.44	0.74
2005	4.29	3.81	5.33	-24.1	-33.0	-23.5	0.64	0.33	0.68
2006	4.45	4.51	5.60	-23.3	-34.3	-24.5	0.72	0.33	0.66
2007	4.99	4.09	4.64	-23.8	-33.5	-23.9	0.67	0.29	0.65
2008	4.94	3.88	4.81	-22.9	-30.5	-21.1	0.71	0.42	0.85
2009	3.64	4.09	4.53	-25.2	-35.2	-24.9	0.63	0.27	0.62
mean	4.72	4.31	5.72	-23.9	-33.8	-24.1	0.68	0.32	0.67
stddev.	±0.66	±0.44	±0.94	±1.3	±1.6	±1.2	±0.07	±0.05	±0.07

(-20.0 °C, 6.2 m/s and 0.87 g/kg) but the maximum in the turbulent heat flux components is easily explained when the mean of the daily product of air temperature and wind speed (Figure 4.6, bottom row) is considered, which represents the main driving parameter of the sensible heat flux (cf. Section 2.2.2, Equation 2.10). Short periods of strong winds and low temperatures leave only little trace in the means of the individual parameters, but when strong anomalies coincide, as for example in the case of cold air outbreaks, they produce a heat flux maximum that persists in the seasonal mean. Similarly, the heat flux minimum in 2009 is hard to explain by the seasonal average of air temperature (-19.5 °C) and wind speed (6.4 m/s), but shows clearly in the mean product of air temperature and wind speed. Again, short-term events dominate the seasonal mean of the atmospheric heat flux.

Of the three different regions, the Ronne polynya features the coldest air temperatures in winter with a 20-year mean of -33.3 °C, the highest wind speeds with a mean of 7.4 m/s and, mainly due to the cold temperatures, the lowest specific humidity of 0.29 g/kg. Over

the Ronne polynya the minimum heat flux in 2008 is accompanied by the second-warmest air temperatures ($-30.1\text{ }^{\circ}\text{C}$), a close-to-average wind speed (7.6 m/s) and the second-highest specific humidity (0.41 g/kg). Therefore the sensible and latent heat flux are low and together cause the atmospheric heat flux minimum. The maximum in 1992 (590 W/m^2), again, is not explained by looking at the seasonal means of the individual forcing parameters. It coincides with below-average air temperatures ($-34.4\text{ }^{\circ}\text{C}$), below-average wind speed (6.8 m/s) and below-average specific humidity (0.28 g/kg). However, a look at the mean product of air temperature and wind speed reveals a peak in 1992 that triggers the heat flux maximum.

At the polynyas in the Antarctic Peninsula region, we find the 20-year winter mean of the air temperature to be $-23.3\text{ }^{\circ}\text{C}$, the mean wind speed is 7.0 m/s and the mean specific humidity is 0.73 g/kg . The by far largest atmospheric heat flux (509 W/m^2) is in 1992. It coincides with the maximum in the Ronne region, but is more easily explained by the coincidence of minimum air temperature ($-26.1\text{ }^{\circ}\text{C}$), highest wind speed (8.7 m/s) and the minimum specific humidity (0.51 g/kg). The minimum winter heat flux to the atmosphere of 278 W/m^2 in 2008 is just as obviously caused by the warmest air temperature ($-18\text{ }^{\circ}\text{C}$), the third-lowest wind speed (5.9 m/s) and the highest specific humidity (1.07 g/kg).

Since the sensible heat flux is the main contributor to the atmospheric heat flux and the surface temperature in polynyas is bound to vary little, the mean of the daily product of air temperature and wind speed features a strong relation with the mean total atmospheric heat flux. Of course not all details correlate, but it gives a very good first estimate to the variability and individual seasonal means of the atmospheric heat flux.

4.3.3 Oceanic heat flux

Sea ice production per unit area is strongly dependent on the heat flux to the atmosphere. If no further energy is supplied, a direct proportionality is expected. However, if the ocean is not at the freezing point, part of the heat loss to the atmosphere is compensated by the ocean's heat content, thereby cooling the water column.

We know from Figure 4.3 that on the continental shelf the oceanic heat flux locally can be strong. Intrusions of Modified Warm Deep Water (Foster and Carmack, 1976; Nicholls et al., 2008, 2009) transport heat onto the shelf, which is then lost to the atmosphere by surface cooling. In general, the oceanic heat flux diminishes with distance from the shelf break; coastal polynyas, however, with their increased convection, can create substantial local maxima.

In this simulation, the average oceanic heat flux due to the erosion of oceanic heat content is 57 W/m^2 in the Brunt polynyas, 49 W/m^2 in Ronne polynya and 48 W/m^2 in the Antarctic

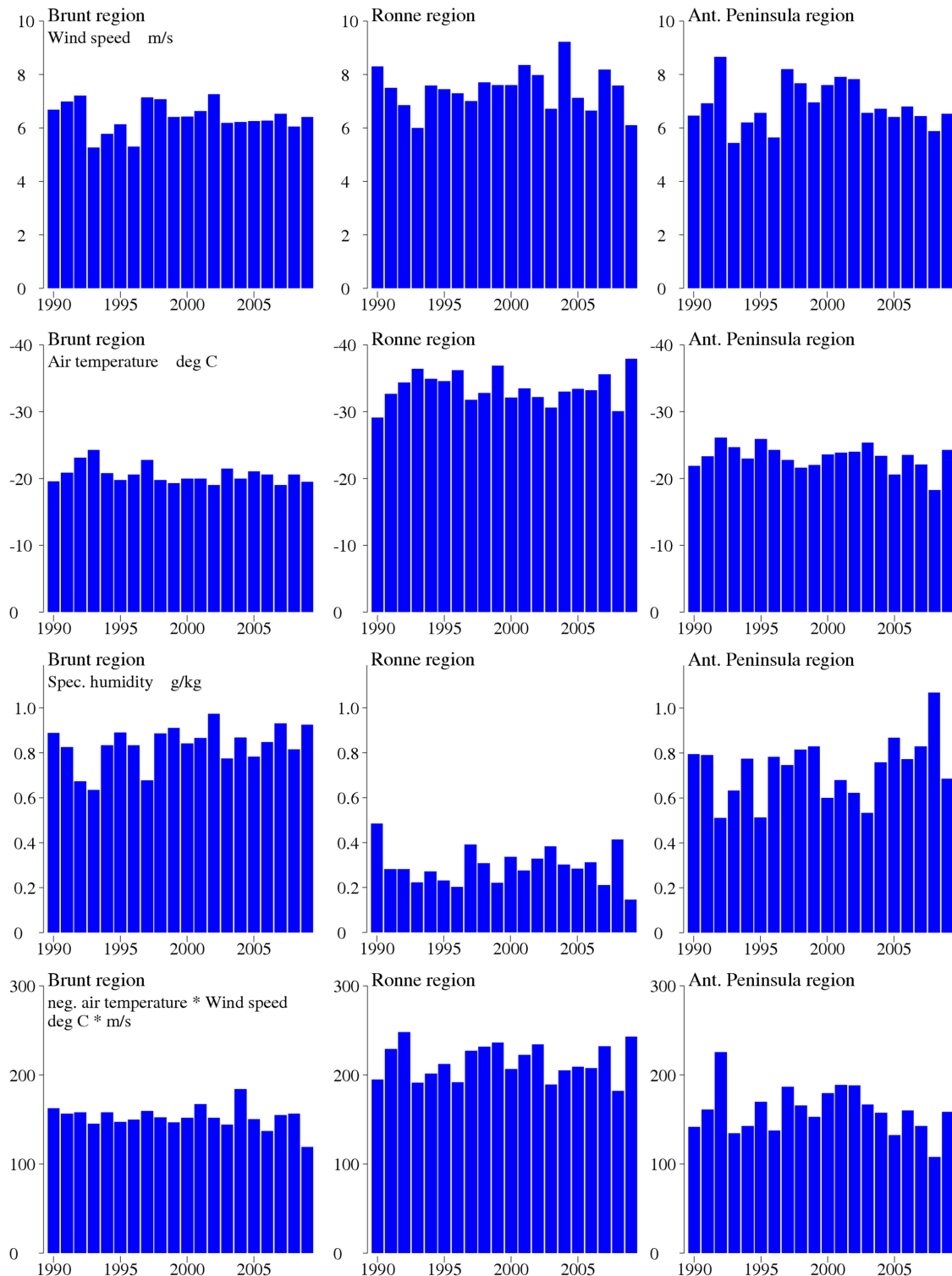


Figure 4.6: Simulated winter (May-September) mean of the main forcing components over polynyas in the three regions. Note that the y-axis of the air temperature graphs is flipped upside down.

Peninsula region (all averaged over polynya days only) (Table 4.1). The oceanic heat flux is highest in the eastern polynyas, where the coastal current enters upon the shelf, but does only slightly decrease and is still substantial in the western polynyas. The contribution of the oceanic heat flux to the atmospheric heat flux is 19 % in the Brunt polynyas, 10 % in Ronne polynya and 13 % in the Antarctic Peninsula polynyas in the long-term winter mean. So, although the absolute values of oceanic heat flux are similar for the three regions, in the Brunt region the relative contribution to atmospheric heat flux is higher by a factor of two.

Outside polynyas only 16 W/m² in Brunt region, 21 W/m² in Ronne region and 20 W/m² in Antarctic Peninsula region are due to oceanic cooling, which is 30-57 % of the total heat flux to the atmosphere outside polynyas. The fact that the oceanic heat flux is higher within polynyas than outside is easily explained by the increased convection under polynyas due to the stronger salt enrichment. The seasonal means of the oceanic heat flux of the individual years are marked with a black line in Figure 4.5. As already explained, the difference between atmospheric and oceanic heat flux is compensated by latent heat gained from sea ice production.

4.3.4 Sea ice production

The sea ice production per unit area in our simulation has a 20-year mean of 7.24 cm/d (on an average of 66 ± 17 polynya days) in the Brunt polynyas. In the Ronne polynya, the mean ice production is 13.23 cm/d (on an average of 57 ± 29 polynya days) and in the polynyas of the Antarctic Peninsula region we find 9.21 cm/d (on an average of 68 ± 23 polynya days). Since the oceanic heat supply within polynyas is a non-negligible, but small contribution to the atmospheric heat flux, minima and maxima of ice production per unit area (Figure 4.7) coincide with the minima and maxima of winter-mean atmospheric heat flux in most cases. At the Brunt polynyas, the highest mean winter ice production per unit area is in 2004 (9.6 cm/d averaged over 61 polynya days) while 1992 features the highest ice production per unit area in Ronne region (15.6 cm/d; 11 polynya days) and the Antarctic Peninsula region (12.7 cm/d; 19 polynya days). The lowest ice production in the Brunt polynyas is found in 2009 with 4.9 cm/d (mean over 86 polynya days). At the Ronne polynya, ice production minima are found for 1994, 2003, and 2008. The absolute minimum (2003) does not coincide with the smallest atmospheric heat flux: Atmospheric heat flux for 2003 is slightly higher than for 2008. Instead, 2003 stands out as the year with the highest oceanic heat flux (82 W/m², Figure 4.5) which, combined with a small heat loss to the atmosphere, limits ice production to 10.94 cm/d (22 polynya days). The Antarctic Peninsula polynyas have their lowest ice production in 2008 (6.4 cm/d; 74 polynya days), which again coincides

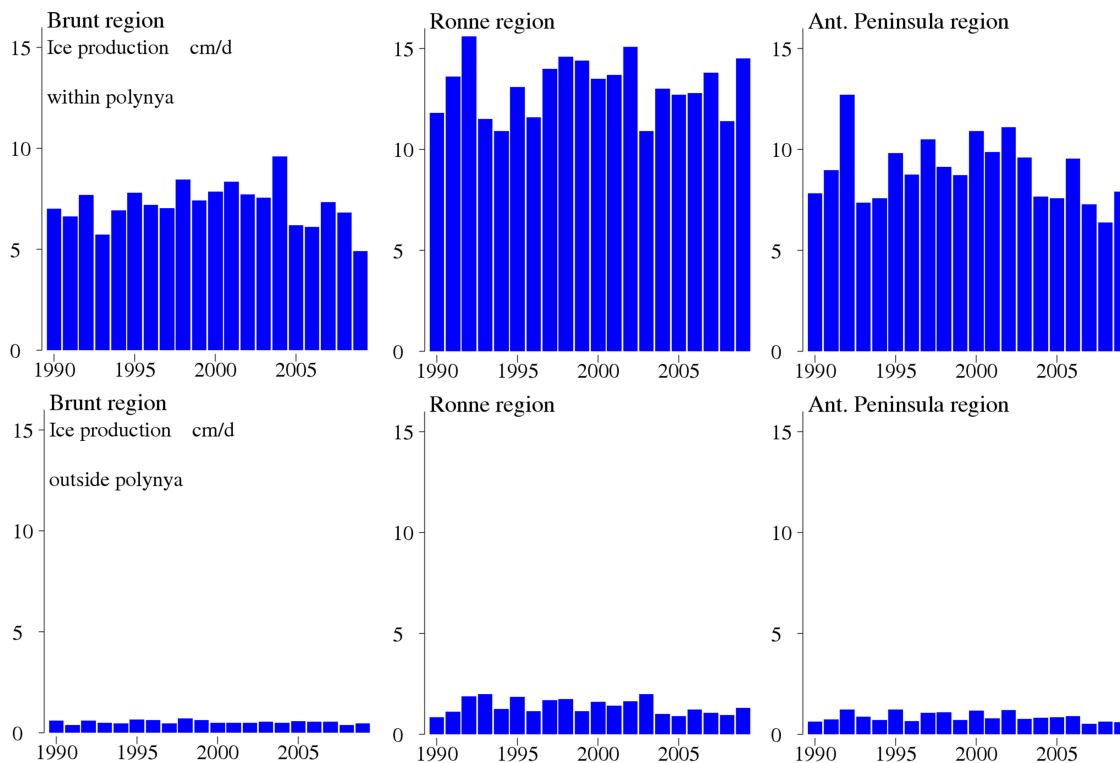


Figure 4.7: Simulated winter (May-September) mean of ice production per unit area in polynyas and outside polynyas in the three regions.

with the absolute minimum of atmospheric heat flux.

Outside the polynyas the regions feature ice production rates per unit area of 0.53 cm/d for the Brunt region, 1.39 cm/d for the Ronne region and 0.86 cm/d for the Antarctic Peninsula region. The ice production per unit area outside the polynyas is only 7 % of the ice production within polynyas in the Brunt region, 11 % in Ronne region and 9 % in the Antarctic Peninsula region.

If accumulated, the multi-year mean of ice production per winter season amounts to 12.9 km³ in the Brunt polynyas, 43.8 km³ in the Ronne polynyas and 21.0 km³ in the polynyas along the southern Antarctic Peninsula. For the entire Southwestern Weddell Sea, polynya ice production features a mean of 105 km³ which is 11 % of the total ice production of 993 km³ but originates from only 0.6 % of the area.

Maxima and minima of the production of ice volume (Figure 4.8) are strongly determined by polynya area so that only in the Brunt region, where the polynya area is least variable, the lowest (highest) annual polynya ice volume production coincides with the lowest (highest) annual ice production per unit area. In 2009 the Brunt polynyas form only 4.5 km³ of ice

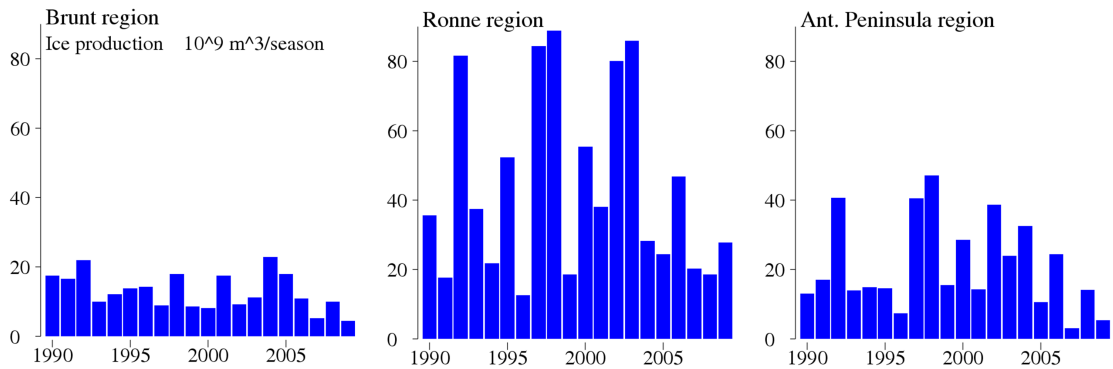


Figure 4.8: Simulated winter (May-September) mean of ice volume produced in polynyas in the three regions.

on an area of 479 km², while their highest production is 22.8 km³ in 2004 on an area of 1403 km². Both times, the coincidence with the minimum (maximum) ice production per unit area is amplified by a relatively small (large) polynya area.

For the Ronne polynya the highest accumulated ice production over the winter months occurs in 1998 (88.8 km³), when the third highest ice production per unit area coincides with the second largest polynya area (4052 km²). The minimum total ice production is found in 1996 (12.6 km³), induced by a relatively low production per area and the smallest polynya area (603 km²).

In the polynyas along the Antarctic Peninsula the smallest amount of sea ice was produced in 2007 (3.1 km³), by the second lowest sea ice production per unit area and the smallest mean polynya area of only 390 km². The maximum ice production occurred in 1998. Although the ice production per area was below average, the by far largest annual polynya extent (4079 km²) more than compensated for it.

Previous studies on the polynya sea ice formation in the Weddell Sea usually based their calculations on sea ice concentration derived from satellite observations (mostly SSM/I) and coarse global atmospheric data sets (often from ECMWF or NCEP/NCAR). The heat flux to the atmosphere that resulted from the energy budget was converted into sea ice production using the assumption that the ocean surface is permanently at freezing temperature and that the oceanic heat flux can be neglected. Our study, although still dependent on a coarse-scale atmospheric data set, is independent of the satellite observations and includes the heat flux provided by ocean cooling, which turns out to be 10-20 % of the heat flux to the atmosphere. We thus expect less ice production in our simulation than in previous studies that did not consider the ocean's heat content. Ice production rates based only on the heat flux to the atmosphere are prone to overestimate the true rates and rather give an upper limit.

Markus et al. (1998) determined the seasonal mean ice production in their southern region including Ronne polynya in the years 1992-1994 to be 87 km^3 . For the same time period our simulation yields 77 km^3 in the Ronne polynya. The numbers agree well, although study areas do not match exactly and the region of Markus et al. (1998) includes the coastline of Filchner Ice Shelf.

For the period 1992-1998, Renfrew et al. (2002) calculated a mean ice production in Ronne polynya of $24 \pm 5.1 \text{ m}$ per unit area and a total of $111 \pm 31 \text{ km}^3$ during the full freezing season, which they individually identified for every year. Using the same intervals, our simulation gives $19.3 \pm 6.2 \text{ m}$ per unit area and a total of $104 \pm 36 \text{ km}^3$. Tamura et al. (2008) found the ice production from March to October in Ronne polynya to accumulate to 85 km^3 as a mean over the years 1992-2001. For the same period our model gives 89 km^3 . The good agreement in both cases is facilitated by Renfrew et al. (2002) and Tamura et al. (2008) using a study area containing a very similar part of the coastline as our Ronne region; it also indicates the robustness of our (and their) results.

For the period of April-October 2003-2008, Drucker et al. (2011) calculated a mean accumulated ice production of $112 \text{ km}^3/\text{season}$ for the Brunt polynyas and $99 \text{ km}^3/\text{season}$ for Ronne polynya. The corresponding values from our simulation are $89 \text{ km}^3/\text{season}$ in the Brunt region and only 50 km^3 in the Ronne region. The differences can be explained by the negligence of the oceanic heat flux and the different extent of the study areas. Drucker et al. (2011) include no locations with water depth over 1000 m and their eastern region stretches farther east and includes part of the polynya forming off Riiser-Larsen Ice Shelf. Also, their southern region extends farther west including a part of the polynyas which we include in the Antarctic Peninsula region.

In general, the comparisons show good agreement, and as expected our values are slightly lower than the ice production calculated from satellite data with one exception: Only the study by Tamura et al. (2008) gives a lower sea ice production than our simulation. However, the values are very close and the uncertainties in the data sets and parameterisations used on both sides can easily explain this outcome.

4.4 Chapter summary

In this Chapter, a long-term run of FESOM forced with data from the NCEP/NCAR Reanalysis was analysed in terms of sea ice concentration, heat transfer to the atmosphere, the heat flux supplied by ocean cooling and resulting sea ice production in the southwestern Weddell Sea and its coastal polynyas during the winter months of the period 1990-2009.

The seasonal cycle of the Southwestern Weddell Sea shows melting prevalent in the

months November-February, during which time open water area increases. It is followed by the autumn freeze-up that brings the highest atmospheric and oceanic heat fluxes and the fastest sea ice production in the basin-wide mean entailing a rapid reduction of open water area. The typical winter situation is established in May and lasts until September. During these months the open water area reduces to small and transient polynyas. The atmospheric heat flux at polynyas rises to its maximum during this time, while it drops steadily in the basin-wide mean. However, due to the small extent of polynyas, the bulk of the sea ice volume produced in winter originates from the so-called 'ice-covered' ocean, although it is the leads within that ice cover that facilitate most of the ice production. During the winter months, the coastal polynyas, covering 0.6 % of the area of the Southwestern Weddell Sea, are source to 11 % of the produced ice volume within that area in the 20-year mean.

Since the net precipitation is two orders of magnitude smaller than the fresh water flux associated with sea ice production, the winter fresh water flux does not differ far from sea ice production scaled with the constant factor $0.805 = \rho_i/\rho_w \cdot (S_o - S_i)/S_i$. All results for the sea ice production in winter are therefore also valid for the winter fresh water flux.

The most active coastal polynya with the largest extent and the highest atmospheric heat flux and sea ice production is found north of Ronne Ice Shelf, other areas of high polynya activity were identified at the western fronts of Brunt Ice shelf and along the coast of the Antarctic Peninsula.

Sea ice production is mostly determined by the atmospheric heat flux, which again is strongly influenced by the sea ice concentration. However, the oceanic heat content compensates part of the heat flux to the atmosphere and in regions of upwelling even induces sea ice melt in spite of heat loss to the atmosphere. A large region with upwelling of warmer waters off the southern continental shelf break leads to warm water intrusions onto the shelf, where they locally inhibit sea ice formation and, especially upon reaching the Ronne polynya, give rise to a high oceanic heat flux.

The atmospheric heat flux over coastal polynyas during the months May-September has a 20-year mean of 313 W/m^2 in the Brunt region, 515 W/m^2 in the Ronne region and 374 W/m^2 in the Antarctic Peninsula region. The interannual variability of the atmospheric heat flux is high and usually dominated by the variability of the sensible heat flux, which is the dominant contributor also in the long-term mean. Outside polynyas, the atmospheric heat flux is mostly determined by the longwave radiation budget, but still variability is ruled by the sensible heat flux component.

The oceanic heat flux was found to be a non-negligible component of the ocean surface heat budget at these high latitudes even on the continental shelf. Maximum values were found in the easternmost region next to Brunt Ice Shelf with 57 W/m^2 in the 20-year mean

due to the warm water entering upon the shelf, but the oceanic heat flux is almost as high in both regions further west with almost 50 W/m^2 , indicating that surface cooling does not prevent above-freezing point water from reaching far onto the continental shelf at depth, which is consistent with observations presented by Nicholls et al. (2008). Therefore, 10-20 % of the atmospheric heat flux during winter at the polynyas in the southwestern Weddell Sea does not result in sea ice production but is compensated by the erosion of the ocean's heat content.

In the 20-year mean, we find a sea ice production of 7.2 cm/d at the Brunt polynyas leading to an ice volume of 12.9 km^3 per winter, 13.2 cm/d at Ronne polynya creating 43.8 km^3 per winter and 9.21 cm/d in the polynyas along the Antarctic Peninsula giving 21.0 km^3 per winter. Keeping in mind the reduction of ice formation by the oceanic heat flux, the results of the simulation compare very well with previous studies about atmospheric heat flux and sea ice production in Weddell Sea polynyas by Markus et al. (1998), Renfrew et al. (2002), Tamura et al. (2008) and Drucker et al. (2011).

Within the investigated regions, areas with a sea ice concentration higher than 70 % feature an atmospheric heat flux of only 11-14 % and a sea ice production per unit area of 7-11 % of the corresponding value within polynyas. Due to the small area of coastal polynyas in the Weddell Sea, the contribution of the much larger ice-covered ocean to heat exchange and sea ice production is prevailing on a large scale, primarily because the leads within the pack ice add up to a considerable area. Locally, however, the coastal polynyas are of great importance since here the ocean-atmosphere exchange is enhanced by an order of magnitude. The exceptionally high freezing rates in coastal polynyas substantially advance salinity enrichment, which is necessary for the production of High Salinity Shelf Water, an important ingredient for bottom water formation. This process will be discussed in the next chapter.

5 Water mass modification on the continental shelf

The surface processes associated with sea ice formation and coastal polynyas have a strong influence on the waters below. In winter, the upward heat flux cools the water at the surface to the freezing point and induces sea ice formation. The salt rejected in the freezing process is accumulated in the water. The increased density of the surface waters generates convection until stability is reinstated and the densest water is collected at the ocean floor. On the continental shelf, the dense water then spreads steered by topography and the general cyclonic circulation of the Weddell Sea until it reaches the shelf break, from where it spills, usually in pulses, down the slope. With increasing depth, the density of the surrounding waters increases reducing the density gradient and thus the angle at which the overflow plume crosses the isobaths.

In this chapter the surface freshwater budget is discussed and salinity on the continental shelf is analysed. HSSW is investigated in terms of volume and export and an estimate of how much WSDW can be formed from the exported dense shelf waters is presented. A definition of all water masses that are mentioned in this chapter is provided in Section 1.2.2.

5.1 Surface fresh water balance

The fresh water or salt balance (Equation 2.26) in the Weddell Sea is largely dominated by sea ice production and melting. Net precipitation $P - E$ becomes a relevant contribution mostly in areas where winter ice production and summer melting nearly balance each other.

The maxima of the surface fresh water flux of the southwestern Weddell Sea (Figure 5.1) are dominated by the sea ice formation in the coastal polynyas where a fresh water flux of the order 10 m/yr is not uncommon. Consequently, the pattern of the mean annual fresh water balance features a strong similarity to the map of winter sea ice production (Figure 4.3, lower right panel). The local maxima of the net precipitation only leave a faint imprint in the fresh water flux as slightly raised values; in the coastal regions hardly any influence of the net precipitation is discernible.

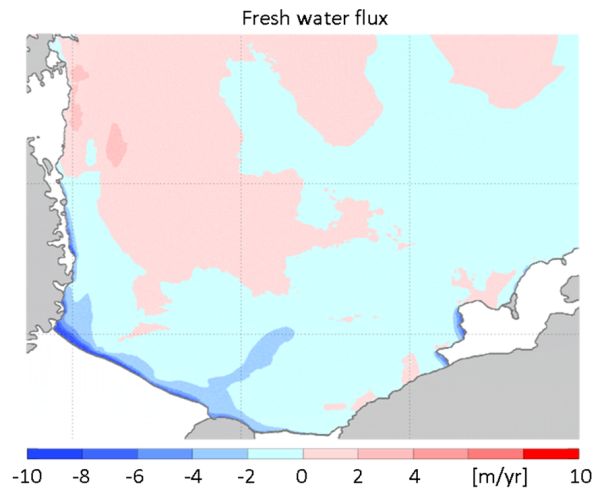


Figure 5.1: Map of mean annual surface fresh water flux.

The model assumes a constant salinity of 4 for sea ice and does not take into account the processes of salt draining out of sea ice as it ages. The salt input into the water column at locations where sea ice is formed is therefore slightly overestimated and regions where sea ice is not primarily formed but is advected into, might in reality experience slightly higher salt input than in the model.

5.2 Salinity distribution

Surface salinity in winter (Figure 5.2) is low where the water penetrates onto the shelf in the east. The Brunt polynyas produce only a small local salinity increase. Toward the west, surface salinity increases over the continental shelf and reaches a first strong maximum (> 34.7) over Berkner Bank. A slightly larger maximum is found over the trench between Berkner Bank and General Belgrano Bank, extending outward from the narrow strip along the front of Ronne Ice Shelf, where coastal polynyas occur. The saline water from these two maxima is advected north off the continental shelf to some extent, but the large area of enhanced surface salinity over the deep Weddell Sea adjacent to the continental slope is associated with the upwelling of warm and salty WDW, which is also visible in the oceanic heat flux (Figure 4.3).

The highest values of surface salinity (> 34.85) are reached where the Ronne Ice Shelf meets the Antarctic Peninsula. From here, with the exception of a narrow (and occasionally interrupted) strip along the peninsula coastline, salinities decrease toward the north until at latitudes $71\text{-}70^\circ$ S the surface salinities over the continental shelf drop rapidly. Over the deep

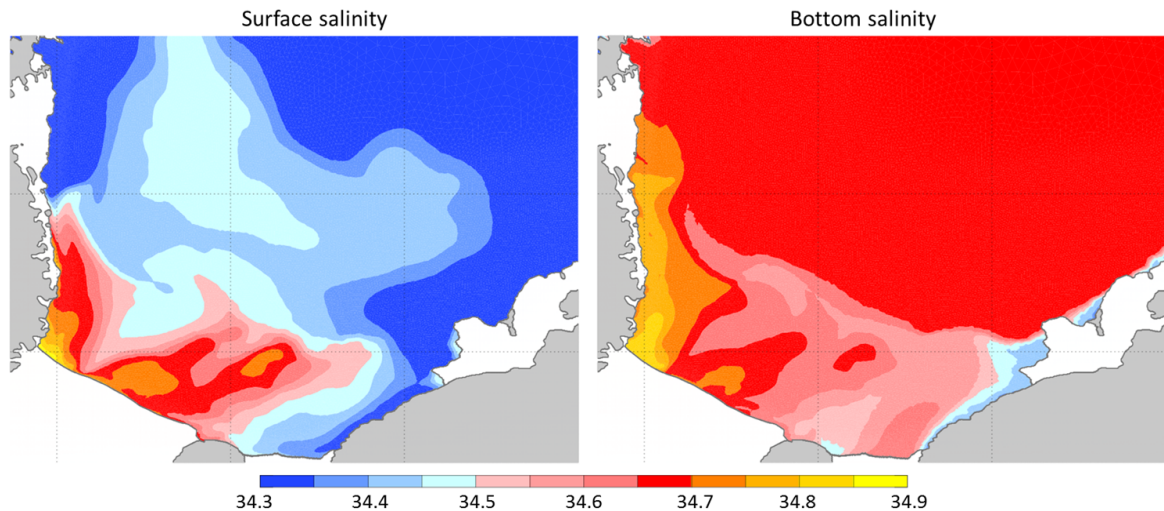


Figure 5.2: Map of mean winter surface and bottom salinity.

ocean the slightly increased surface salinities extend farther to the north.

At the bottom, we find the deep ocean covered with water of salinities between 34.65 and 34.7 (salinities decrease from WDW to WSDW and WSBW). The shallower areas of the continental shelf are again freshest in the east, however, with salinities > 34.4 they are more saline than at the surface. Salinity increases toward Filchner Trough, which is not filled with ISW in the simulation, but with the densest water (> 34.6) from the adjacent areas. (The Filchner Trough features unrealistically low salinities in the simulation, since the model geometry by neglecting ice shelf cavities does not allow the saline waters from the Ronne region to flow under the ice shelf and – as ISW – fill Filchner Trough. Consequently, no dense water plumes from the Filchner overflow are found on the continental slope in the east in the simulation. For a discussion of the consequences of the neglect of ice shelf cavities please refer to Sections 3.1.2 and 5.5.3.)

On Berkner Bank, we find an imprint of the surface maximum, but the high salinities of the surface are not met. Bottom salinities in the trench between Berkner and General Belgrano Bank are only slightly weakened compared to the surface values. This also holds true for the maximum in the southwestern corner, where bottom salinities are slightly below maximum surface values. From the corner, the substantially salt-enriched water spreads over the ocean floor and is steered northward. In the areas to the north, bottom salinities are higher than the salinities observed at the surface. North of 70° S also bottom salinities decrease on the continental shelf.

The drop in salinity over the western shelf at latitude $\approx 70^\circ$ S is connected to the moraine of Larsen C Ice Shelf which is an obstacle to further northward flow and steers the saline

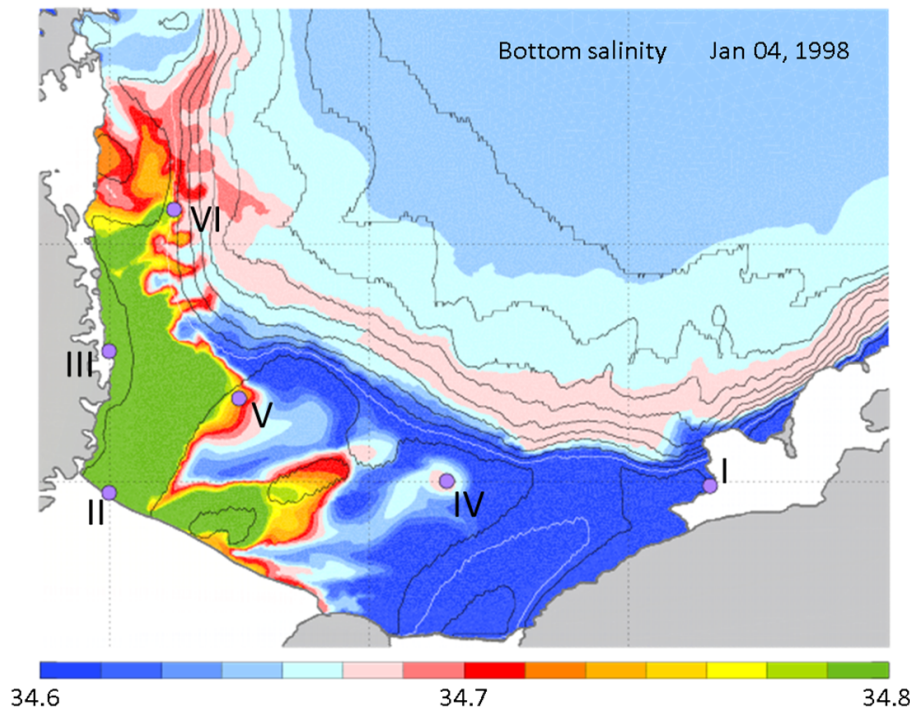


Figure 5.3: A snapshot of the bottom salinity on January 4, 1998 with depth contours in 500 m intervals (black). Additionally the 700 m isobath is drawn in light grey. The violet circles show the Locations I-VI that are referred to in Section 5.3 and Figures 5.4 and 5.5.

water east to the shelf break, where it leaves in plumes, as it was also observed by Gordon (1993). Due to their transient nature, these plumes are not visible in the long-term mean, but in daily salinity maps (Figure 5.3).

5.3 Seasonal cycle of the on-shelf waters

The local salt or freshwater addition from sea ice formation or melting is spread by advection and (turbulent) mixing, such that salinity profiles at any given location generally do not only reflect the local salt input but mostly the effect of events upstream. Six locations (Figure 5.3) were chosen to investigate how sea ice and polynya activity influence the hydrography on the continental shelf.

At Location I in front of Brunt Ice Shelf (25.25° W, 75° S) polynyas occur often and freezing rates are high. Location II is situated in front of Ronne Ice Shelf (60° W, 75.5° S), where polynya activity is strongest and salinities are highest. (It is the same location where the temperature and salinity were evaluated in Section 3.4.) Location III is close to the coastline of the Antarctic Peninsula (60° W, 72.25° S). Also here, polynya activity is high

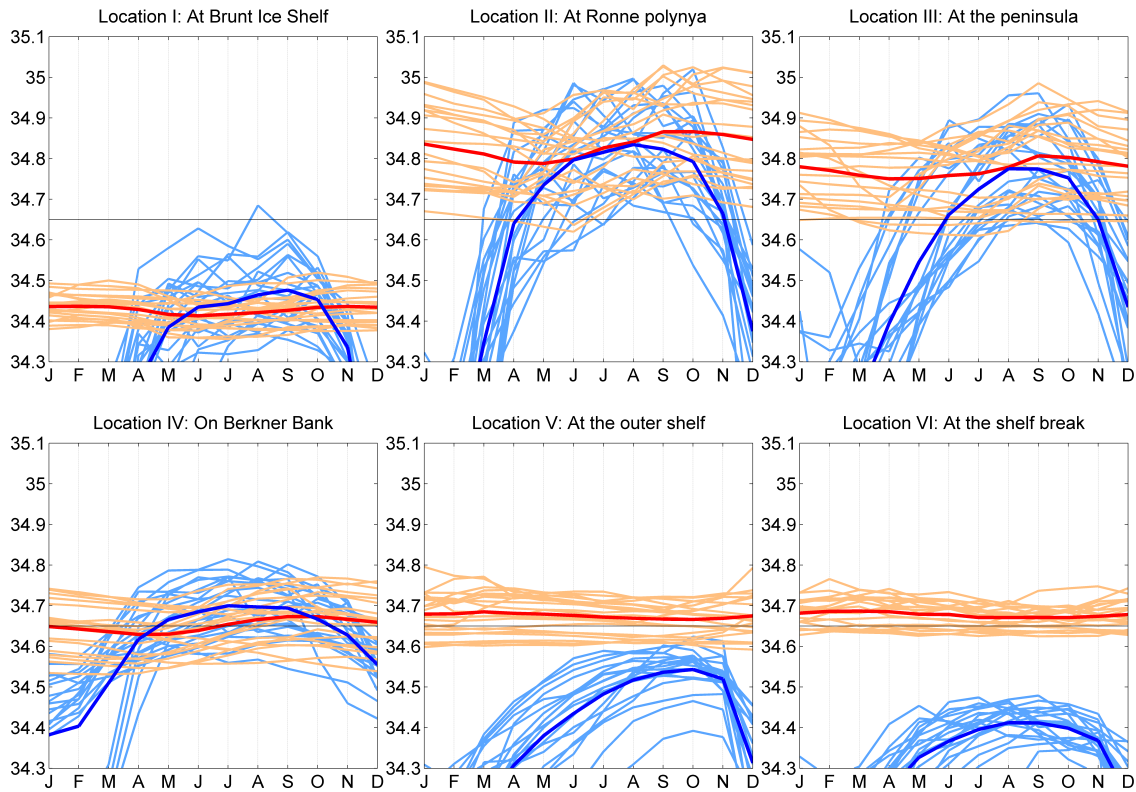


Figure 5.4: The annual cycle of surface (light blue, 20-year mean: dark blue) and bottom (orange, 20-year mean: red) salinities at Locations I-IV in the years 1990-2009. The thin black line marks the threshold value of HSSW.

and a strong influence of surface salt fluxes on the water column is expected. Location IV is placed at the salinity maximum over Berkner Bank (40.5° W, 75° S) and Location V (52.5° W, 73.25° S) is positioned in the outer shelf area on the western side of General Belgrano Bank. Location VI (56° W, 70° S) is situated at the shelf break, close to the sill in front of Larsen C Ice Shelf. At this location, the dense water that was produced in the polynyas is steered off the shelf by the east-west rise of the Larsen C moraine that blocks the northward path of the dense bottom-bound water mass.

At Location I, the shelf is only just widening. Water masses entering the shelf have relatively low salinities (Figure 5.4) and temperatures above freezing point except at the surface during winter (Figure 5.5). Even at the end of winter, salinities (with a singular exception at the surface) do not meet the criteria for HSSW, as is expected east of Filchner Trough (Carmack and Foster, 1975a). During winter, surface waters are often colder and more saline than the bottom waters, however, the surface properties do not reach the bottom by convec-

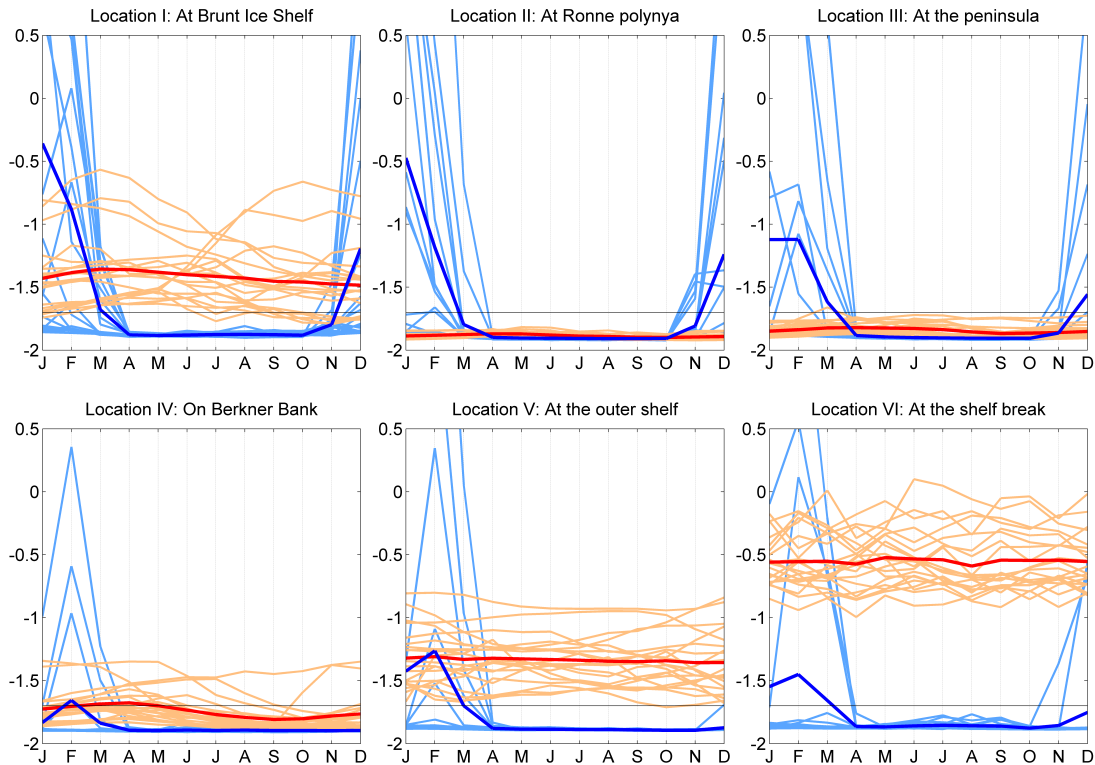


Figure 5.5: The annual cycle of surface (light blue, 20-year mean: dark blue) and bottom (orange, 20-year mean: red) temperatures at Locations I-IV in the years 1990-2009. The thin black line marks the threshold value of HSSW.

tion without being diluted by a constant advection of warmer and fresher waters originating from the Weddell Gyre at depths below 100-200 m. In the 20-year mean, the bottom salinity increases by 0.023 between June and November, but the maximum increase within one year accumulates to 0.12 (May-October 2001).

At the Ronne polynya (Location II) the bottom salinity usually is above the 34.65-threshold for HSSW and bottom temperatures are very close to the surface freezing point throughout the year. Thus, at Location II we generally find HSSW at the bottom of the water column (with rare exceptions). Surface salinities fulfill the criteria only during the winter months, when the water mass is formed by the freezing process and the water column is nearly homogeneously mixed.

In a typical year, surface temperatures are at the freezing point from April to October, while during the remaining months interannual variability is high and strongly depends on sea ice conditions. As discussed in Section 3.4, surface layer heating during summer tends to be overestimated in the simulations. Location II is far from the shelf break and the convective

processes in winter show no significant dilution. On average, the bottom salinity increases by 0.078 during the months May-September, but can increase as much as 0.32 (April-September 1992) in exceptional years.

Location III at the Antarctic Peninsula shows features similar to Location II. Usually bottom salinities meet the HSSW criterion, while salinities at the surface do so only during a short period in winter. Compared to Location II, the salinity increase in autumn and early winter is decelerated due to less sea ice production. Considering the shortness of the period during which local production of the bottom water mass occurs, and the general circulation patterns of the region, it is likely that some of the bottom water is advected from areas further south. The mean annual cycle of the bottom salinity is similar to the findings at Location II but slightly weaker, with a mean increase of 0.057 between April and September and a maximum increase of 0.27, also between April and September 1992.

On Berkner Bank (Location IV), we find a similar situation as at the Brunt polynyas. Salinities, however, are higher and temperatures lower (especially in the summer, where the often perennial ice cover keeps the surface close to the freezing point). Still, surface salinities during winter exceed bottom salinities, indicating persistent lateral mixing with fresher waters at depths of 100-200 m. Thus the bottom waters do not qualify as HSSW in all years, but in the mean year Berkner Bank becomes a source region to HSSW toward the end of the freezing season. This is facilitated by the shallow water column, which facilitates fast erosion of the ocean's heat content and thus rapid ice production and also a faster increase of salinity in the water column for a specified amount of salt added at the surface.

On the outer shelf (Location V, Figure 5.3), we find bottom salinities over the 34.65-threshold in most years and also in the 20-year mean. The bottom temperatures however (with the exception of one single monthly mean) do not meet the HSSW requirement and the mean features values between -1.3°C and -1.4°C throughout the year. The surface temperatures are close to the freezing point, often also in summer, since the area usually retains a perennial ice cover. In winter, surface salinities are at their maximum but in general do not reach the values of the bottom salinities, which is a clear indication of the bottom water (at least in part) being advected from areas with more active sea ice production.

At the shelf break (Location VI) the bottom salinity is always higher than the salinity at the surface and thus the bottom water clearly is not produced locally but advected from other areas. The bottom salinity is high while bottom temperatures in general are between -1°C and 0°C indicating a substantial – and overestimated (Section 5.4.2) – admixture of off-shelf waters.

While the bottom salinity at Locations I-IV rises during the winter months, the bottom salinity at Locations V and VI has a maximum at the end of summer and a minimum in July

(although the seasonal cycle at the bottom of the water column is very weak). This supports the hypothesis that the bottom waters at these locations are not a product of the local surface processes but are advected. The waters with the highest salinity imprint reach the shelf break roughly 4-5 months after their production in late winter.

We find that at locations where bottom temperatures are very close to the freezing point and their interannual variability is low ($\approx 0.15^\circ\text{C}$), the interannual variability of the bottom salinity is highest (≈ 0.3). The very low bottom temperatures signify that during winter the entire water column is close to the freezing point and most of the heat flux to the atmosphere has to be compensated by sea ice production, so that these are the locations of maximum salt fluxes. The variability of the atmosphere and thus of the heat flux and the sea ice production thereby imprints itself on the salinity.

At locations where more heat is supplied by admixture of warm waters, the atmospheric heat flux is compensated by the ocean's heat content to a higher degree, which leads to a higher variability of the bottom temperature ($\approx 1^\circ\text{C}$), while the influence of the atmosphere on the salinity of the water column and therefore its variability is subdued (≈ 0.15).

5.4 High Salinity Shelf Water

5.4.1 HSSW volume

As can be seen in the salinity maps (Figure 5.2), the densest shelf waters are formed at the polynyas in front of the Ronne Ice Shelf and the southern Antarctic Peninsula. To contribute to deep water formation, the dense water has to move from its production site to the shelf break and down into the abyss. A snapshot of bottom salinity (January 4, 1998) shows plumes of saline water leaving the shelf at the western shelf break between 72°N and 69°N , where the dense water is guided to the east and off the shelf by the Larsen C moraine (Figure 5.3).

The amount of HSSW present on the Weddell Sea continental shelf (Figure 5.7, middle panel) is subject to a strong seasonal cycle, caused by the processes of sea ice production and melting every year. And as in the sea ice production, we find strong variations between individual years. The annual increase of the HSSW volume, which in some years does not surpass $2 \cdot 10^4 \text{ km}^3$ but in others exceeds $6 \cdot 10^4 \text{ km}^3$, features a strong relationship with the accumulated sea ice formation in Ronne region (Figure 5.7, top panel, blue symbols).

The relation with the sea ice formation in Ronne polynya alone (Figure 5.7, top panel, green symbols) is less strong. For this there are three reasons:

- The high ice production at coastal polynyas due to their small areas can only affect a

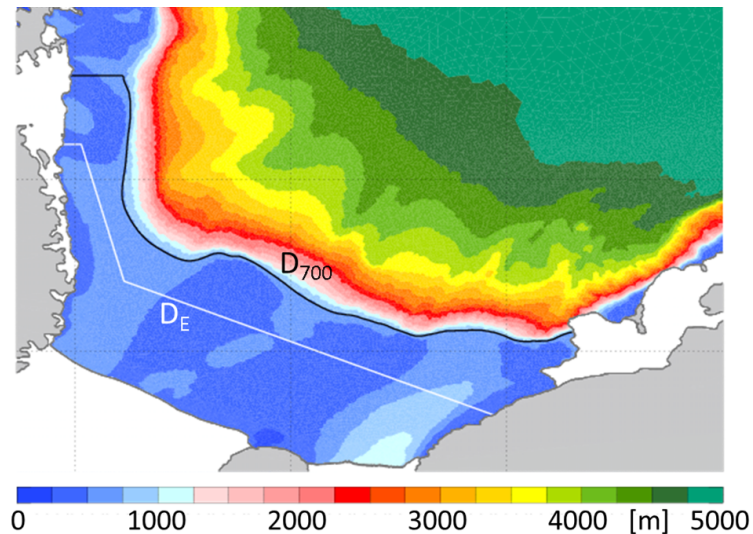


Figure 5.6: Map showing the demarcation lines D_E (white) and D_{700} (black).

limited volume of the on-shelf waters and only the regional ice production can elevate the salinity of a sufficiently large volume of water over the critical value.

- Areas with sea ice concentrations $> 70\%$ can still contribute substantially to the annual sea ice production (mostly through leads), especially in years of little polynya activity.
- For the modification of the waters on the Weddell Sea continental shelves, the Ronne region is not the only influence; the waters arrive preconditioned by the surface processes of much larger areas and those are better reflected by the regional sea ice production than in the even more local values from the Ronne polynyas.

5.4.2 HSSW export

On its way to the shelf break, the HSSW has to cross the demarcation line D_E (Figure 5.6). The line was defined such that the main source regions lie south, but the line is far enough from the shelf break to avoid the occurrence of strong mixing before the HSSW crosses the line. A second line, D_{700} , was chosen to follow the 700-m isobath (cut off at 67° S, north of the Larsen C moraine, where most of the dense water on the shelf is topographically steered to the shelf break). At 700 m depth, the dense water is already on the continental slope and slowly sinking while still following the (here northward) circulation of the Weddell Gyre.

Like the HSSW volume, the export of HSSW across the demarcation line D_E (Figure 5.7, bottom panel) features a seasonal cycle. Usually, the highest export rates occur during spring

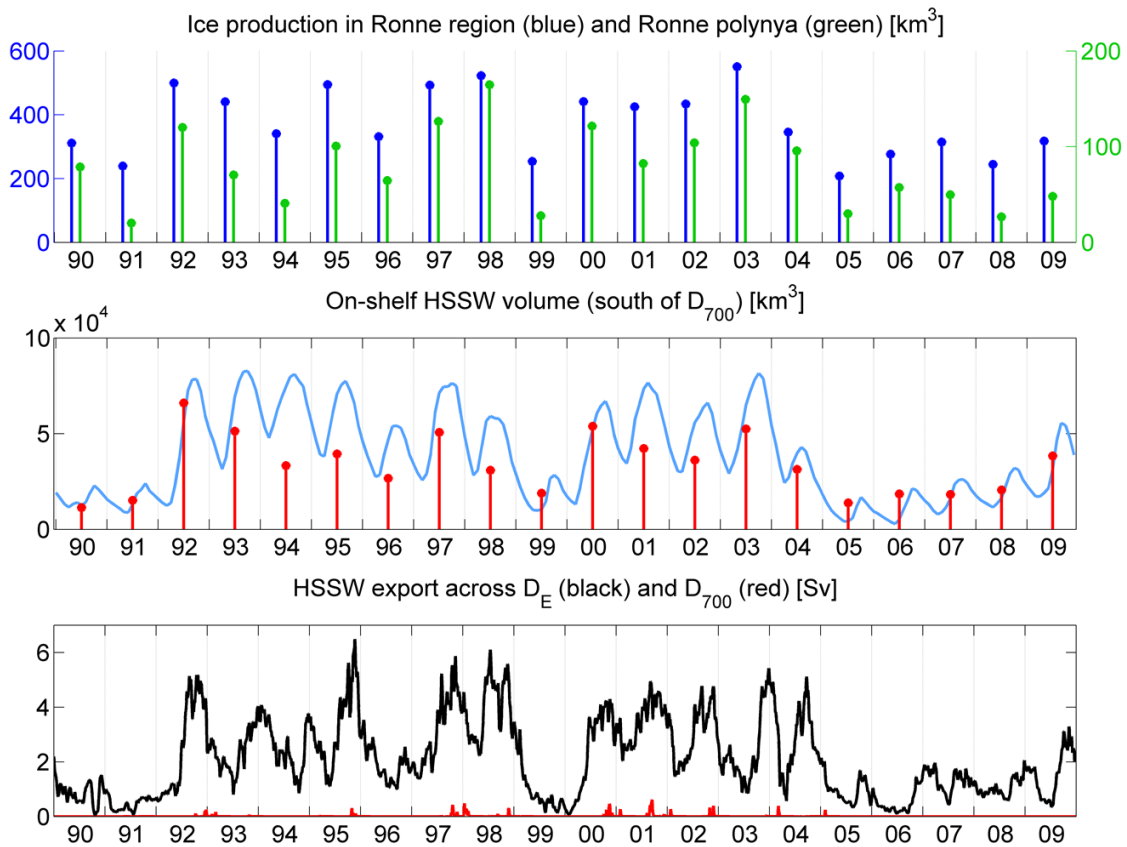


Figure 5.7: Annual accumulated sea ice production (positive contribution only) in Ronne region (blue) and Ronne polynya (green; top panel), the volume of HSSW present south of D_{700} (monthly values, light blue) and its increase during the freezing period (red; middle panel) and daily values of HSSW exported northward across D_E and D_{700} (bottom panel) during the years 1990-2009

and early summer. The seasonal cycle, however, is not very dominant. The shape of the export in individual years can differ far from the mean cycle; especially in years with small HSSW export rates.

The maximum export rates reached in any given year feature a strong correlation with the maximum of the HSSW volume reached in that year. The loss of volume in the summer months is almost entirely due to the HSSW export flux, which reaches maximum values of 6 Sv. The increase of the HSSW volume in autumn and winter results from a modification of the on-shelf water properties that is generated by ice production. During the active production of HSSW, the increase of HSSW volume is limited by the HSSW export. Still, the years of high HSSW production usually feature both high HSSW volumes and high HSSW export. In the 20-year mean 2 Sv of HSSW are exported across D_E .

Almost no water with the properties of HSSW reaches the 700m-isobath (Figure 5.7, bot-

tom panel, red line) which is consistent with observations from the Ice Station Weddell experiment (Gordon, 1998). Only in years with very high export rates across D_E , we see small amounts of HSSW exported across D_{700} (maximum rate 0.6 Sv). Although the export rates across D_E include water that might not leave the shelf but stay on the shelf long enough to get diluted again, they provide the best picture of the export of undiluted HSSW.

So far, only few studies have estimated the export of HSSW. Nicholls et al. (2009) estimate the total export of HSSW from the continental shelf to be 2.8 Sv, whereof 1.4 Sv flow into the ice shelf cavities (Foldvik et al. (2001); Nicholls et al. (2003) and an equal amount (Wepfer et al., 1996) spills over the shelf break. Considering the uncertainties that both the measurement-derived estimates and the simulation are based on they are in good agreement.

5.5 Deep water formation: An estimate

The model's resolution of the continental slope (with ≈ 9 km horizontally and 130-250 m vertically) is still too coarse to allow for the thin bottom layer of dense water to follow a realistic pathway into the abyss; instead, the dense water is mixed with the volume of each element it enters into. Due to the size of the elements the mixing processes on the slope are strongly overestimated and the dense water loses its characteristics too rapidly, which is a common problem for OGCMs (Heuzé et al., 2013).

Despite this, the formation of WSDW is estimated in this section based on a few assumptions and simplifications. A pseudo water mass, the High Salinity Mixing Partner, and a water property called formation potential are introduced for that purpose. Lastly, the influence of ice shelf cavities and ISW on the deep / bottom water formation is evaluated.

5.5.1 High Salinity Mixing Partner and formation potential

In the framework of this study, the High Salinity Mixing Partner (HSMP) is defined as a water mass that comprises all waters that have the potential to form WSDW by mixing with warmer and fresher water masses. This water mass serves as a starting point to assess the potential rate of deep water formation. In case of the end product WSDW, the salinity of HSMP has to be higher than the salinity of WSDW ($S_{HSMP} > S_{WSDW}^*$) and its temperature has to be lower than the temperature of WSDW ($T_{HSMP} < T_{WSDW}^*$). Thus, to define HSMP it is necessary to define S_{WSDW}^* and T_{WSDW}^* for which I chose typical values, such that $S_{WSDW}^* = 34.67$ and $T_{WSDW}^* = -0.25$ °C. Depictions of the definition of HSMP and the properties of the product water mass in a T-S-diagram can be found in Figure 5.8.

Being able to determine a specific volume of water that has potential to form WSDW, it is the logical next step to try to assess that potential. For this purpose I introduce an additional

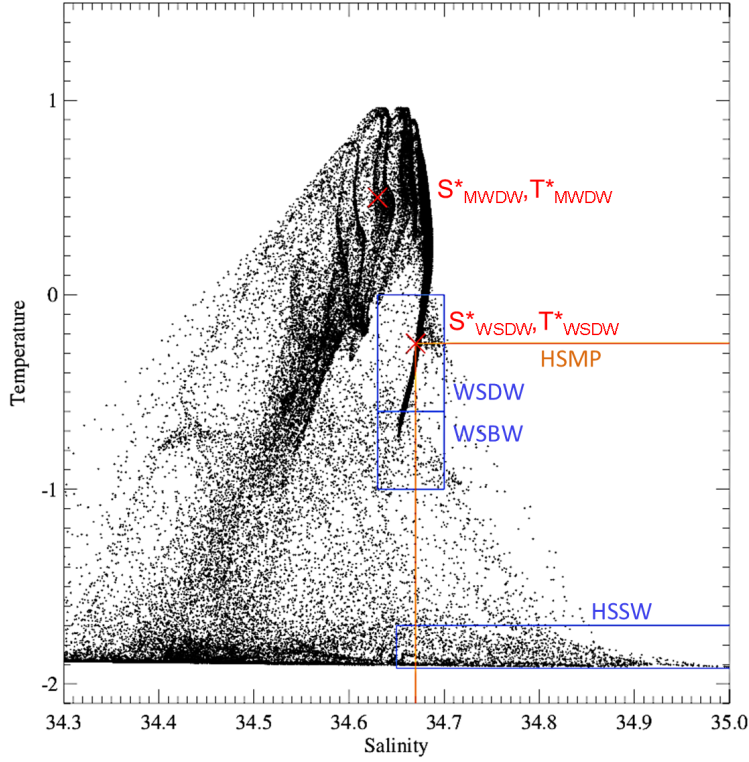


Figure 5.8: T-S-diagram illustrating the assumed mixing principle of the formation potential. Mixing partner and product water masses are marked with a red cross, while the limits of HSMP are marked with orange lines. The water masses WSDW, WSBW and HSSW are marked with blue rectangles.

property, the formation potential \mathcal{P} . It quantifies the potential of a volume of water to form a specified product water mass by mixing with another specified water mass, which in this case is slightly modified WDW with the typical values $S_{MWDW}^* = 34.63$ and $T_{MWDW}^* = 0.5^\circ\text{C}$ (Figure 5.8). In the case of a HSMP sample, the potential to form WSDW by mixing with MWDW $\mathcal{P}_{WSDW}^{MWDW}$ is given by

$$\mathcal{P}_{WSDW}^{MWDW} = \text{minimum} \left(\begin{array}{l} \mathcal{P}_T = \frac{T_{HSMP} - T_{MWDW}^*}{T_{WSDW}^* - T_{MWDW}^*} \\ \mathcal{P}_S = \frac{S_{HSMP} - S_{MWDW}^*}{S_{WSDW}^* - S_{MWDW}^*} \end{array} \right) \quad (5.1)$$

$\mathcal{P}_{WSDW}^{MWDW}$ gives the multiplication factor that states how much water with $S \geq S_{WSDW}^*$ and $T \leq T_{WSDW}^*$ can be produced from a volume of HSMP by mixing with MWDW of the specified properties. The possible mixing ratio is then given by $1 : (\mathcal{P} - 1)$. As can already be seen in the T-S diagram (Figure 5.8), temperature provides a fixed upper limit to the potential, since the temperatures of the dense water can not be lower than the freezing point.

Since \mathcal{P} is dependent on typical values for T and S of both product and mixing water mass and works with the assumption that no other mixing takes place, this number merely gives an estimate of potential WSDW formation rates. In reality, the mixing path will not be a straight line in a T - S -diagram but curved, since the original HSSW parcel will meet waters with changing properties on its way and optimal mixing ratios will hardly ever occur. Thus, in many cases the final mixing product will not meet the chosen criteria of WSDW. However, both product and mixing water mass are not limited to a single value of temperature or salinity, but can assume a certain range in temperatures and salinities. Therefore, small deviations from the assumed values T^* and S^* are allowed. Still, the obtained potential will only be fully translated into formation in an idealized environment.

5.5.2 Potential formation of WSDW

At the demarcation line D_E most of the HSMP also meets the criteria for HSSW. In the 20-year mean HSMP export (3.1 Sv) surpasses the HSSW export (1.9 Sv) by 1.2 Sv (Figure 5.9). Peak values of the HSSW export are 5-6 Sv while HSMP export can reach rates of 6-8 Sv. The product of formation potential with the export rate gives the rate of possible WSDW formation. For the HSSW we find a mean formation potential for WSDW of 2.7; the HSMP, which encompasses also water with warmer temperatures and thus loses the properties necessary to form WSDW faster, has a formation potential of 2.1. The difference in exported volume, however, causes the possible WSDW formation from HSSW with 5.1 Sv to lie well below the possible WSDW formation from HSMP with 7.6 Sv.

At the 700-m isobath D_{700} , the situation is very different from that on the shelf at D_E . Almost no transport of HSSW is present in the model but the export rate of HSMP is strongly increased (mean 5.2 Sv). During the passage of the dense water from D_E to D_{700} evidently mixing takes place and at D_{700} most of the water lost the HSSW properties but retained the potential to form WSDW. Therefore, the entrained ambient water can now also take part in the formation of WSDW and adds to the HSMP volume.

However, the formation potential of HSMP is eroded by this mixing and at D_{700} HSMP has a formation potential of only 1.4 in the 20-year mean. The potential formation rate of WSDW has increased by 0.3 Sv compared to the findings at D_E , but continued strong mixing (overestimated in the simulation due to the model inability to resolve near-bottom plumes of dense water) will quickly erode the WSDW formation potential further and ultimately leave most of the waters unable to participate in deep water formation.

At 700 m depth, as also observed at D_E , periods of high HSMP export (peak values of 14-17 Sv) and periods of very little (or no) export are alternating irregularly. A timespan of

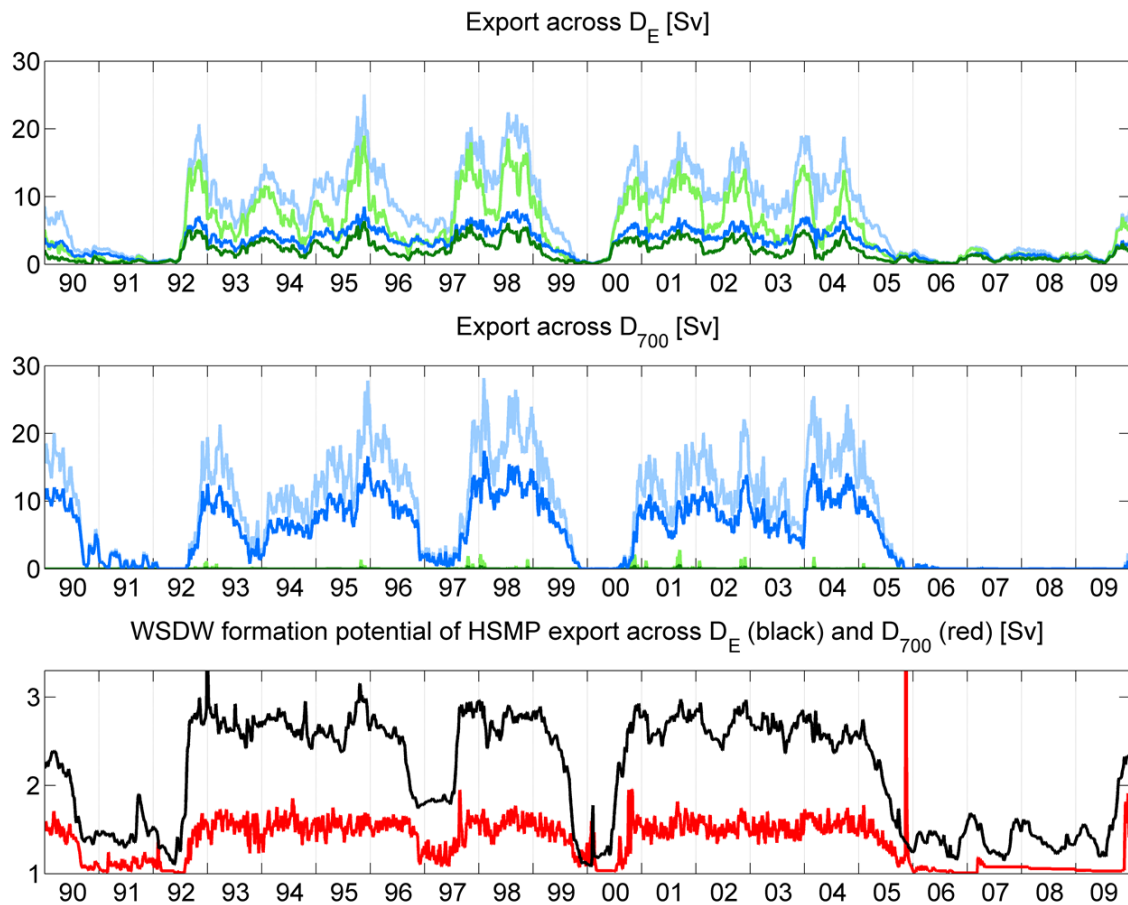


Figure 5.9: HSSW (dark green) and HSMP (dark blue) export and the corresponding potential WSDW formation (light green/light blue) at D_E (top panel) and at D_{700} (middle panel) and the WSDW formation potential of HSMP at both demarcation lines (bottom panel) during 1990-2009

1-3 months is found to elapse between dense water peak exports at D_E and corresponding peaks D_{700} . Although the possible WSDW formation rate increases between D_E and D_{700} during the high export periods, periods of low dense water exports at D_E often lead to zero-export of HSMP at D_{700} .

The WSDW formation potential of the exported dense water features a strong dependence on the export rate (and the annual maxima of the on-shelf HSSW volume). Small volumes of dense water have a very low potential to form WSDW; partly due to being affected stronger by previous mixing (the surface to volume ratio is larger), but also because little salt input on the shelf leads to both smaller volumes and less saline dense waters. Therefore, if little HSSW is present, it gets diluted fast and thus loses all potential to form WSDW. Only in large volumes it can retain the potential to form WSDW and even entrain ambient waters.

The increase in volume, however, erodes the WSDW formation potential.

At D_{700} the overestimated mixing close to the shelf break results in too small values of HSSW export and too large values of HSMP export. Simultaneously, the WSDW formation potential of HSMP is eroded too much. The stability of the product of export and potential, the potential WSDW formation, with 7.6 Sv at D_E and 7.9 Sv at D_{700} gives it some credit as an upper limit of possible WSDW formation under idealized conditions. However, the true formation rate is probably much lower, since the real mixing for many parcels of water will differ from the assumed mixing and much of the water will get diluted and not reach depths below 1500 m. Especially when the potential of the HSSW is low, usually coinciding with low HSSW export, complete dilution is probable. Setting the HSMP export to zero in the analysis during periods when the formation potential is not close to the maximum (< 2.5 at D_E and < 1.4 at D_{700}) still gives a potential WSDW formation of 5.8 Sv and 7.3 Sv, respectively.

Allowing for deviations from the assumed mixing scheme and dilution, the actual rate of WSDW (including WSBW) formation from dense waters exported directly from the continental shelves in the long term mean is likely between 4 Sv, a major fraction of the rate calculated from the HSSW export at D_E , and 6 Sv, the lowest value derived from the considerations of HSMP. However, the rate of deep water formation is not constant, and not only interannual, but also decadal changes have been observed by e.g. Fahrback et al. (2011), Purkey and Johnson (2012) and Huhn et al. (2013).

The concept of formation potential is not limited to the formation of WSDW and is easily adapted to other product water masses. However, many uncertainties are involved in the choice of typical temperature and salinity values of mixing partner and product water mass and the assumption of only the two chosen water masses mixing. While the investigation of the WSDW formation gives a rough impression of the possible consequences of the HSSW export from the continental shelf, due to the uncertainties involved, a similar consideration of the formation of e.g. WSBW will serve no further purpose and will therefore not be included.

5.5.3 Contribution by ISW formation and export

As described in Section 3.1.2, part of the HSSW that is formed in or near Ronne polynya enters under the Filchner-Ronne Ice Shelf and leaves as ISW via the Filchner Trough. Where the Filchner Trough meets the continental shelf break at 610 m, the ISW mixes with WDW and the newly formed WSDW / WSBW descends down the continental slope, partly circulating with the Weddell Gyre, partly led straight down by an underwater canyon. Two studies by Foldvik et al. (2001) and Nicholls et al. (2003) combined give an estimate of the HSSW flow under the Ronne Ice Shelf as 1.4 Sv (Nicholls et al., 2009). The ISW-overflow from the

Filchner Trough, while Carmack and Foster (1975b) thought it negligible, was estimated by Foldvik et al. (1985b) to be 0.7 Sv and later was corrected by Foldvik et al. (2004) stating it to be 1.6 ± 0.5 Sv. Since ISW is colder and less saline than HSSW and at the Filchner overflow is more likely to mix with WDW instead of MWDW, it is thought to participate in the formation of WSBW instead of WSDW (Gordon, 1998). Foldvik et al. (2004) estimated the WSBW formation rate from the Filchner outflow to be 4.3 Sv.

From Section 5.4, we know that the export of HSSW over the shelf break is largely accountable for the decrease of HSSW volume on the shelf during summer. The flow of HSSW under the ice shelf is therefore likely to reduce the export to the north over the shelf break and the southward export of 1.4 Sv must be subtracted from the total export of 2 Sv HSSW in the simulation. This would leave 0.6 Sv of HSSW escaping to the north resulting in only 1-2 Sv of deep and bottom water formation additional to the 4.3 Sv from the Filchner outflow (Foldvik et al., 2004). It should be kept in mind, that any of the figures in this calculation is subject to substantial uncertainties and the northward transport of 0.6 Sv is merely based on the assumption that the available estimates are true. Also, possible contributions to the deep water formation from source regions in front of the Larsen Ice Shelf are not included.

The resulting total deep and bottom water formation of 5-6 Sv compares well with the findings of Fahrbach et al. (1994) who estimated 1.2 Sv of WSDW and 2.6 Sv of WSBW formation from the thermohaline analysis of a Weddell Gyre section. However, our result is on the low side compared to deep and bottom water formation rates for the Weddell Sea of 10 Sv found by Hellmer and Beckmann (2001) and 9.7 Sv found by Naveira Garabato et al. (2002b). Studies conducted by Schodlok et al. (2002) and Meredith et al. (2001) found >6.4 Sv and <6.6 Sv, respectively, of WSDW leaving the Weddell Sea.

5.6 Chapter summary

In this chapter the salinity in the on-shelf water column was investigated in terms of its origin, distribution and the effect on the formation of HSSW and – using some assumptions – WSDW. The salinity on the southwestern Weddell Sea continental shelves is primarily regulated by sea ice production and melt processes. Most salt is added to the water column along the front of Ronne Ice Shelf and the southern part of the Antarctic Peninsula. At coastal polynyas, especially Ronne polynya, the high ice production rates generate a high surface salt flux into a comparatively small volume of water. Therefore the most saline waters originate from the coastline.

On the eastern part of the shelf, typically the saline water created during winter at the surface in high ice production regions does not reach the bottom undiluted and the water

column is kept at lower salinities by the advection and admixture of fresher waters, which by their heat content also prevent the temperatures of the lower water column to drop to the freezing point. During the melting period and autumn, however, bottom salinities exceed the surface values.

East of the Filchner Trough, the criteria for HSSW generally are not met. At the shallow areas of Berkner Bank, in the mean year (averaged over 1990-2009) the salinity rises over the threshold value of 34.65 during the winter months. However, within the 20-year period we find years with bottom salinities below the threshold throughout the year as well as years with values continually above the threshold.

In the areas of recurrent polynyas in front of Ronne ice Shelf and the Antarctic Peninsula coastline, bottom salinities are very high and increase over the winter months, while bottom temperatures are always close to the freezing point. During the winter the surface salinities reach values that match the bottom salinities very closely and the entire water column is nearly homogeneously mixed. Deep convection occurs and the dense water mass is replenished from the surface. With few temporary exceptions, which occur mostly in autumn, the bottom waters at the coastal polynyas in the western part of the shelf classify as HSSW. During winter and spring usually also the surface waters – and thus the entire water column – meet the HSSW criteria.

Closer to the shelfbreak, we usually find bottom waters that are more saline than the winter surface waters. These bottom waters are not formed locally but are advected from the source regions of dense water near the coast; they have already experienced notable admixture of warmer and fresher waters. While in most years salinities are still above 34.65, the temperatures are much warmer than the threshold value of HSSW. Here, bottom salinities are highest at the end of summer, which indicates an advection time scale from the dense water source regions of roughly 6 months.

HSSW usually occurs perennially in an area at and around the coastal polynyas in front of the Ronne Ice Shelf and the southern Antarctic Peninsula. The volume increases during autumn and winter, when sea ice production increases the salinity of the on-shelf water column. This increase in volume is not only due to the increasing salinities in other areas (depending on the sea ice formation and polynya activity), but also reflects an increase in the thickness of the HSSW layer up to the entire water column thickness.

During spring and summer, the export of HSSW causes the on-shelf volume of HSSW to decrease. The export typically is highest in years when also the HSSW volume is large. The increase of HSSW volume in autumn and winter is due to changing properties of the on-shelf waters caused by sea ice production. Within one freezing period the volume increase depends strongly on the regional sea ice production in the southwestern corner of the Weddell

Sea continental shelves. In years of little ice production, the maximum HSSW volume at the end of winter is $\approx 0.5 \cdot 10^4 \text{ km}^3$ while in years of high ice production volumes of $2.5 \cdot 10^4 \text{ km}^3$ are reached. Also the export rates of HSSW feature a strong variability. At the demarcation line that encompasses the southernmost part of the continental shelf (D_E in Figure 5.6), we find maximum values of 4-6 Sv in years with high HSSW volume and rates between 0 Sv and 2 Sv in years of low HSSW production. In the 20-year mean the export of HSSW equals a steady export rate of 2 Sv.

On the continental slope, the mixing processes affecting the thin bottom layer of dense water are overestimated, which is a common feature of global OGCMs (Heuzé et al., 2013). To overcome the effect of this spurious mixing the impact of shelf processes on deep water formation has been evaluated introducing the concept of a WSDW formation potential under the assumption of a very simple mixing scheme. Although there are large uncertainties, the possible WSDW formation induced by processes on the southwestern Weddell Sea continental shelf was estimated to be between 4 Sv and 6 Sv in the 20-year mean.

6 Impact of different atmospheric forcing data sets

As already discussed, coastal polynyas are highly dependent of the local wind field. Thus, the simulation of coastal polynyas strongly depends on the atmospheric forcing data. All results presented in the previous chapters were obtained from a model run forced with NCEP/NCAR Reanalysis data. This atmospheric data set has a low spatial resolution of 1.875°. Higher resolution in the atmospheric data is expected to improve the ocean model's ability to reproduce sea ice concentration and sea ice production realistically. The influence of four different atmospheric data sets on sea ice and ocean salinity is investigated in this chapter.

By courtesy of the Environmental Meteorology section of the University of Trier, namely L. Ebner and Prof. Dr. G. Heinemann, I had access to 33 months of GME data (60 km, 6-hrs resolution) and 6 months of data from two regional COSMO model implementations (15 km / 5 km, 1-hr resolution). These three atmospheric forcing data sets have been introduced with more detail in Section 2.3.

The 33-month GME run was branched-off from the NCEP run on April 1, 2007. From the GME run the two 6-month runs with COSMO forcing (COSMO-15 run and COSMO-5 run) were branched off on March 1, 2008. Since the COSMO model is a regional model, for both runs the data was nested in the global GME data set.

6.1 Polynya formation

A series of ice concentration maps from a polynya event from August 23 to August 29, 2008 illustrates the sensitivity of the simulated formation of coastal polynyas to the atmospheric forcing data set (Figure 6.1). On day 234 (not shown) none of the experiments feature any ice concentrations below 85 %; the satellite image has lower ice concentrations (down to 60 %) only in a small region in front of Ronne Ice Shelf.

On day 236 (August 23, 2008), the satellite image shows the Ronne polynya open west of 58° W. The patches of reduced ice concentration values along the Antarctic Peninsula in the AMSR-E image are almost entirely misleading and actually show the dimensions of the ice

shelves in 2008. This statement is based on the fact that these regions exhibit reduced ice concentrations in all 4 satellite images and especially that on day 242, when polynyas have formed off the Antarctic Peninsula ice shelves, the regions concerned still feature unchanged mildly reduced concentrations instead of further reductions. The coastline visible in the pictures is the coastline of the RTopo-1 data set (Timmermann et al., 2010; it appears to match the front signature visible in the satellite data quite closely.

The NCEP run on day 236 features small polynyas along the Antarctic Peninsula, primarily on the northwest-southeast running parts of the coastline due to the strong southwesterly wind prevailing at the western coastline. At the western Ronne Ice Shelf only a slight reduction of the ice concentration is visible, although offshore winds are present. The ice concentration of the GME run is much closer to the satellite image and displays a polynya on the westernmost part of the Ronne Ice Shelf, while the rest of the coastline shows no signs of polynya formation. The pattern is caused by locally very strong offshore winds with a stronger southerly component than found in the NCEP wind field. Also the band of strong winds in the GME case veers offshore at 73° S and to the north we find weak winds at the coastline. The sea ice concentrations (and the wind fields) of the COSMO-15 and COSMO-5 runs are very similar to those of the GME run. Compared to the GME wind, the COSMO data features slightly higher wind speeds at the coastline and weaker winds off-shore.

Two days later (day 238; August 25, 2008) the satellite image reveals the polynya elongated along the Ronne Ice Shelf front, but with higher ice concentration values. In the NCEP run, the offshore winds at the Ronne Ice Shelf front opened the polynya, although it does not reach as far east as the satellite data shows and has a very sharp edge combined with very low concentration values. The southwesterly offshore winds at the coast of the Antarctic Peninsula are still present but have weakened; the polynyas at the peninsula therefore are almost closed but still show a remnant reduction of the ice concentration.

The GME forced ice concentration is again closer to observations than NCEP; the polynya is elongated and its edge is more gradual. However, although the winds in the west are very weak and the strongest offshore winds are found east of 55° W, the eastern part of the polynya is underdeveloped compared to the satellite observations. The two COSMO runs both display a wind field and ice concentration similar to the GME case, but in the west the Ronne polynya is reduced in area compared to day 236 and smaller than in the GME run. Its shape is now more elongated, but except for the westernmost part of Ronne Ice Shelf its width is very narrow.

On day 240 (August 27, 2008) the satellite image shows the Ronne polynya almost closed with remnant patches of reduced sea ice concentration. At the coastline of the Antarctic Peninsula at about 72° S, a small patch of reduced ice concentration is visible. The NCEP

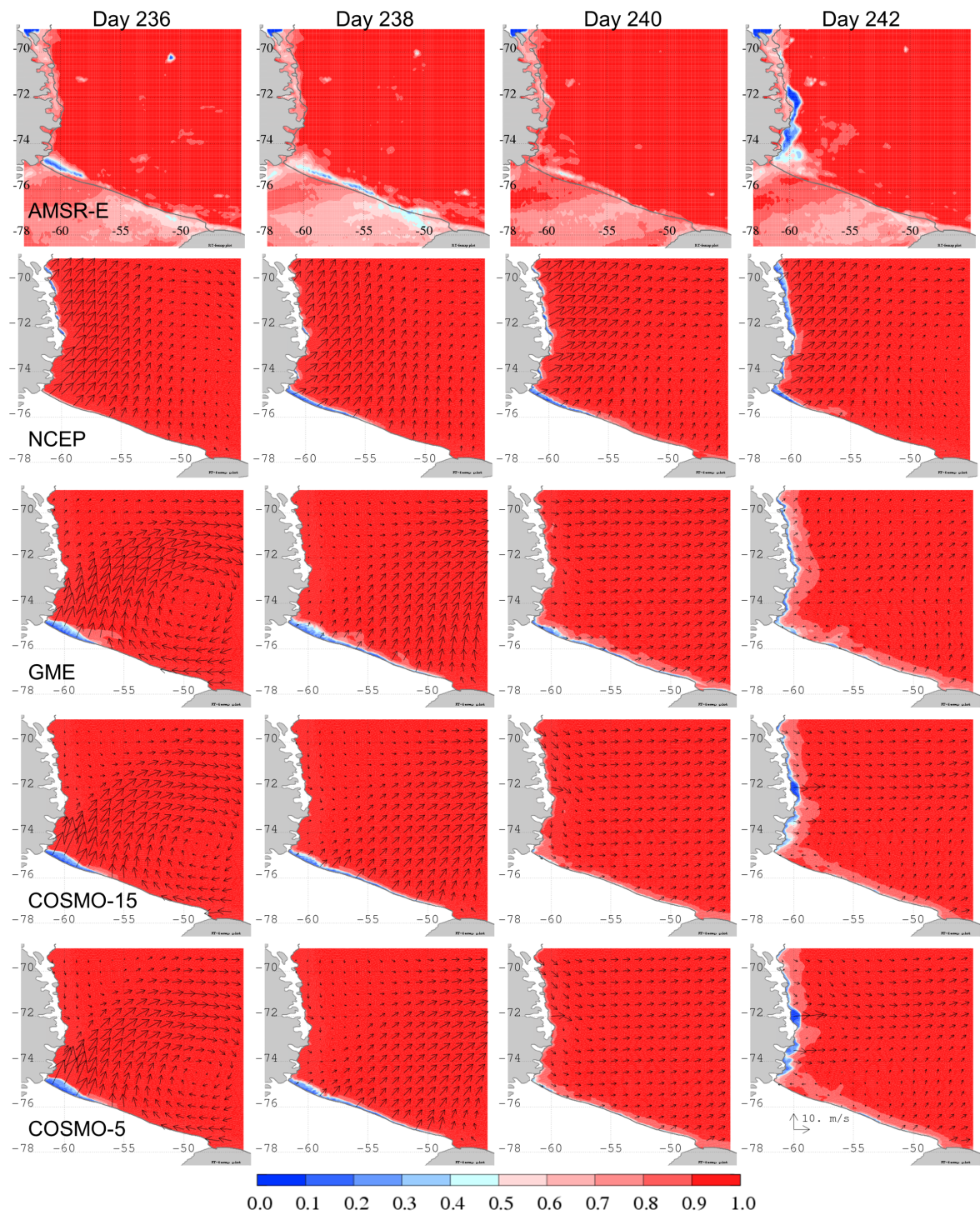


Figure 6.1: Daily mean sea ice concentration maps for four days between August 23 and August 29, 2008 from AMSR-E observations and the four model runs. For the model runs also the mean wind field of the day is displayed by the black arrows.

and GME runs both show the Ronne polynya still open. In the NCEP run, we again find an overestimated polynya activity along the Antarctic Peninsula coastline due to the strong southwesterly winds, while the GME run at the peninsula only shows an almost imperceptible narrow ribbon of slightly reduced ice concentrations created by the weak westerly winds.

Here, the COSMO results differ from the GME results and show a better performance. In agreement with satellite data, they feature only remnants of the Ronne polynya. Along the Antarctic Peninsula, like GME, but slightly more intense, the COSMO runs depict a ribbon of reduced ice concentrations. However, the COSMO winds feature local maxima at 72° S, where the strongest reduction in sea ice concentration is found in the satellite image.

The Ronne polynya is closed on the satellite image of day 242 (August 29, 2008) but along the Antarctic Peninsula (especially its southernmost part) a polynya with varying width has opened. The NCEP run shows high polynya activity at the peninsula and the adjacent part of Ronne Ice Shelf. While the ice concentration values and even the accumulated polynya area match those of the satellite picture fairly well, their shape and localisation differs due to the unvarying NCEP wind field. The GME winds at the peninsula are primarily westerly and much weaker. However, the ice concentrations in the GME run have a similar pattern as in the NCEP run, only the edges of the polynyas are much more gradual and ice concentration values at the coastline tend to be higher than in the NCEP case.

The COSMO wind fields feature westerly winds at the Antarctic Peninsula coastline of locally variable strength, which create more localised polynyas. In the COSMO-15 run, the lowest ice concentrations are found at about 72° S and two other focal points are found at about 73.5° S and 74.5° S. In the COSMO-5 run this localisation is even more pronounced; all three patches are larger and especially the southern two display lower ice concentration values. The pattern of the COSMO-5 run is very close to the satellite observations. While the northernmost polynya is very well captured, the polynya at 73.5° S is larger and has lower ice concentration values in the observations. The southernmost polynya in the observations is a large, but blurry patch of only moderately reduced ice concentrations and thus constitutes the most prominent difference between COSMO model results and satellite image. Both COSMO runs show little polynya activity at the Ronne Ice Shelf, which is in good accordance with observations.

All model runs seem to favour the westernmost part of the Ronne polynya too much. East of 58° W the Ronne polynya in all runs is very narrow, if open at all. As could be expected from the fact that the COSMO-15 run used GME data as boundary conditions and COSMO-5 uses COSMO-15 data on its boundaries, the strongest differences appear between the NCEP forcing and the GME/COSMO forcings. The coarse resolution of both NCEP and GME becomes visible especially in areas of high topographic variability like the Antarctic Penin-

sula and results in an overly smooth wind field and ribbon-shaped polynyas covering most of the coastline. The higher resolution of both COSMO model implementations becomes important to reproduce the variability of the offshore winds in this mountainous area. The steep valleys channel the buoyancy-driven winds and where they open towards the coastline, strong offshore winds can occur, while to the side in the lee of the mountains relatively weak winds are found. The high horizontal resolution of the COSMO model implementations (especially COSMO-5) allows for a good representation of these small-scale patterns and produces a sea ice concentration distribution that is very close to the satellite observations.

6.2 Mean patterns

To obtain a first idea of the large-scale differences between the forcing data sets, maps of the major forcing variables wind and air temperature and the resulting sea ice concentration and ice production per unit area are presented showing the mean over April-August in the years 2007-2009 for NCEP and GME forcing and 2008 for COSMO-15 and COSMO-5, since the data from both COSMO implementations are only available for 2008. This section investigates spatial patterns and changes thereof between years. A short quantification of differences between the runs is presented in Section 6.5.

6.2.1 Near-surface wind

The wind field over the southwestern Weddell Sea in the 5-month mean (Figure 6.2) reveals substantial differences between the forcing data sets. In the NCEP data, for all three years strong easterly to northeasterly winds dominate the area around Brunt Ice Shelf. A lesser maximum with southwesterly winds is found at the (south-)western coastline. In the space between the two maxima, the winds of the NCEP forcing are generally weak (< 4.5 m/s) over the southwestern Weddell Sea.

In contrast, in the GME forcing almost the entire area features mean wind speeds > 4.5 m/s with a tendency to increased wind speeds over the open ocean. A minimum is found in all years at the western coastline, where southerly winds occur (as is expected from observations (Schwerdtfeger, 1975; Parish, 1983)). In 2007, also the coastline of Coats Land features very weak winds. A wind speed reduction at this location is also observed in 2009, although less distinct. However, in 2008 we find a strong wind speed maximum covering the northern part of the Coats Land coastline next to Brunt Ice Shelf.

In 2008, also the GME wind speed maximum over the open ocean is exceptionally strong in both mean wind speed and vector mean. The flow connecting the two maxima results in a cyclonic pattern, the center of which is located at roughly 28° W / 72° S. Also in the NCEP

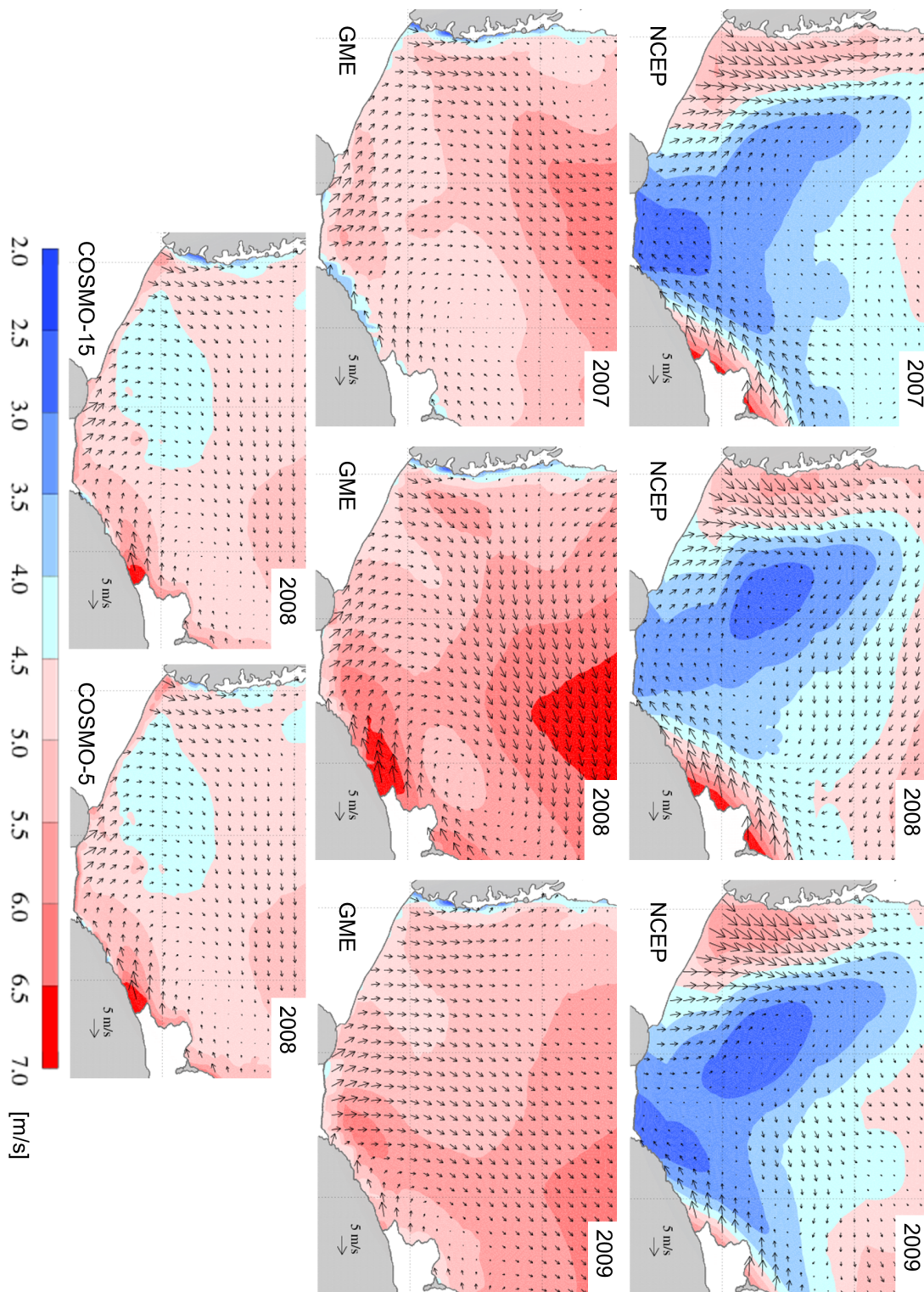


Figure 6.2: Wind field maps averaged over April-August: NCEP/NCAR Reanalysis and GME for 2007-2009 and COSMO-15 and COSMO-5 for 2008. The arrows depict the vector mean and the background colours show the mean wind speed.

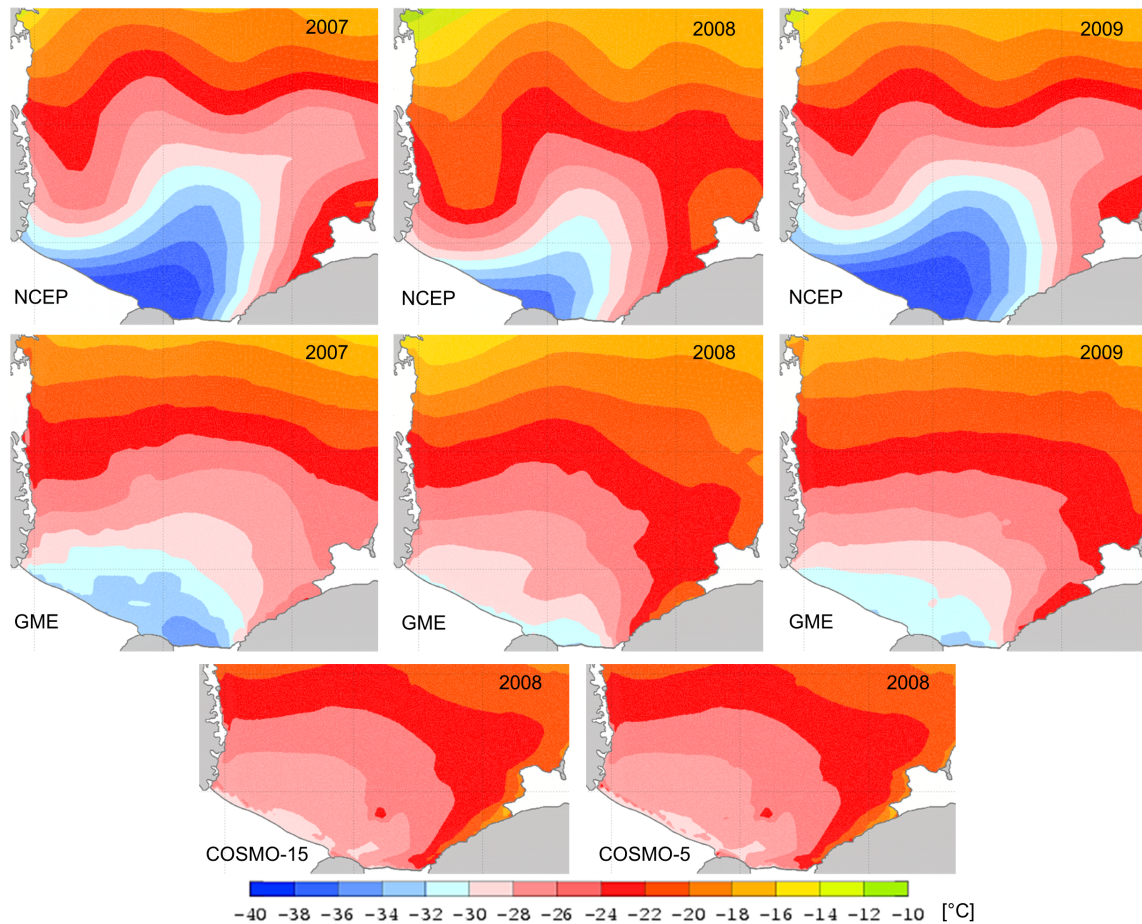


Figure 6.3: Air temperature maps averaged over April-August: NCEP/NCAR Reanalysis and GME for 2007-2009 and COSMO-15 and COSMO-5 for 2008.

data, the year 2008 features a cyclonic wind pattern, but it is weaker, larger in extent, and its center is located further west ($\approx 43^\circ \text{ W} / 73^\circ \text{ S}$).

The distinctions, which set the 2008 wind field apart, may very well be connected to the La Niña/positive Southern Oscillation Index (SOI) event in this year. The strengthening of cyclonic air flow in the southwestern Weddell Sea agrees well with the local wind anomalies pattern Kwok and Comiso (2002) found for a positive SOI scenario.

The two COSMO data sets feature almost identical wind fields. The pattern is also very similar to the GME wind pattern, the mean wind speeds however are significantly lower in almost all of the area, except for narrow stretches along the fronts of the Filchner and Ronne Ice Shelves.

6.2.2 Air temperature

For the air temperatures (Figure 6.3), the large scale distributions in NCEP and GME forcing are similar with warm air temperatures in the north, which decrease toward a minimum near Berkner Island. Along the eastern coast we find comparatively warm air temperatures (often with a gradient in northward direction). However, in the NCEP data strong undulations are visible, (which are probably related to the spectral method used for calculation in the NCEP/NCAR Reanalysis model,) while the GME temperatures feature a much smoother picture. Also, the minimum in the NCEP temperatures is more pronounced and located to the west of Berkner Island, while we find it to the east of the island and less pronounced in the GME data. In both data sets, 2008 is the warmest of the three years, as is expected during a La Niña / positive SOI event (Kwok and Comiso, 2002; Yuan, 2004).

The two COSMO implementations, again, have very similar results and the pattern resembles the pattern of the GME temperatures. However, the minimum at the southern ice shelf front is slightly less pronounced than in the GME data and located west of Berkner Island. Also, the air at and downstream of the Brunt polynyas (and the polynya at Riiser-Larsen Ice Shelf) experienced warming from the open water areas and local temperature maxima are visible. A southward indent of elevated temperatures in the COSMO air temperature fields, which is also visible in the GME data, is connected to the signature of the grounded iceberg A23 and the surrounding polynyas.

In both COSMO data fields and less pronounced in the GME air temperatures, we find a narrow stretch of very cold air temperatures in front of e.g. Ronne Ice Shelf, (where it is best visible, but not limited to) adjoined by small local maxima of the temperature. This feature is spurious and results from the use of different land masks in the atmospheric and oceanic models. The cold temperatures mark areas, where the atmospheric model still assumes the presence of an ice shelf and the small temperature maxima indicate the presence of polynyas at the ice shelf front.

6.2.3 Sea ice concentration

In the AMSR-E measurements of sea ice concentration (Figure 6.4), the most striking features are the Ronne polynya, the iceberg A23 with the fast ice bridge (best visible in 2008), and the polynyas in front of Brunt Ice Shelf. The presence of A23 and its influence on the surrounding sea ice make it impossible to decide which forcing performs better in the area of the Filchner Ice Shelf. Unfortunately, this is the area where the sea ice concentrations differ most between the model runs. While in the NCEP run in all three years only a very weak and narrow reduction in the sea ice concentration is visible in front of Filchner Ice Shelf due

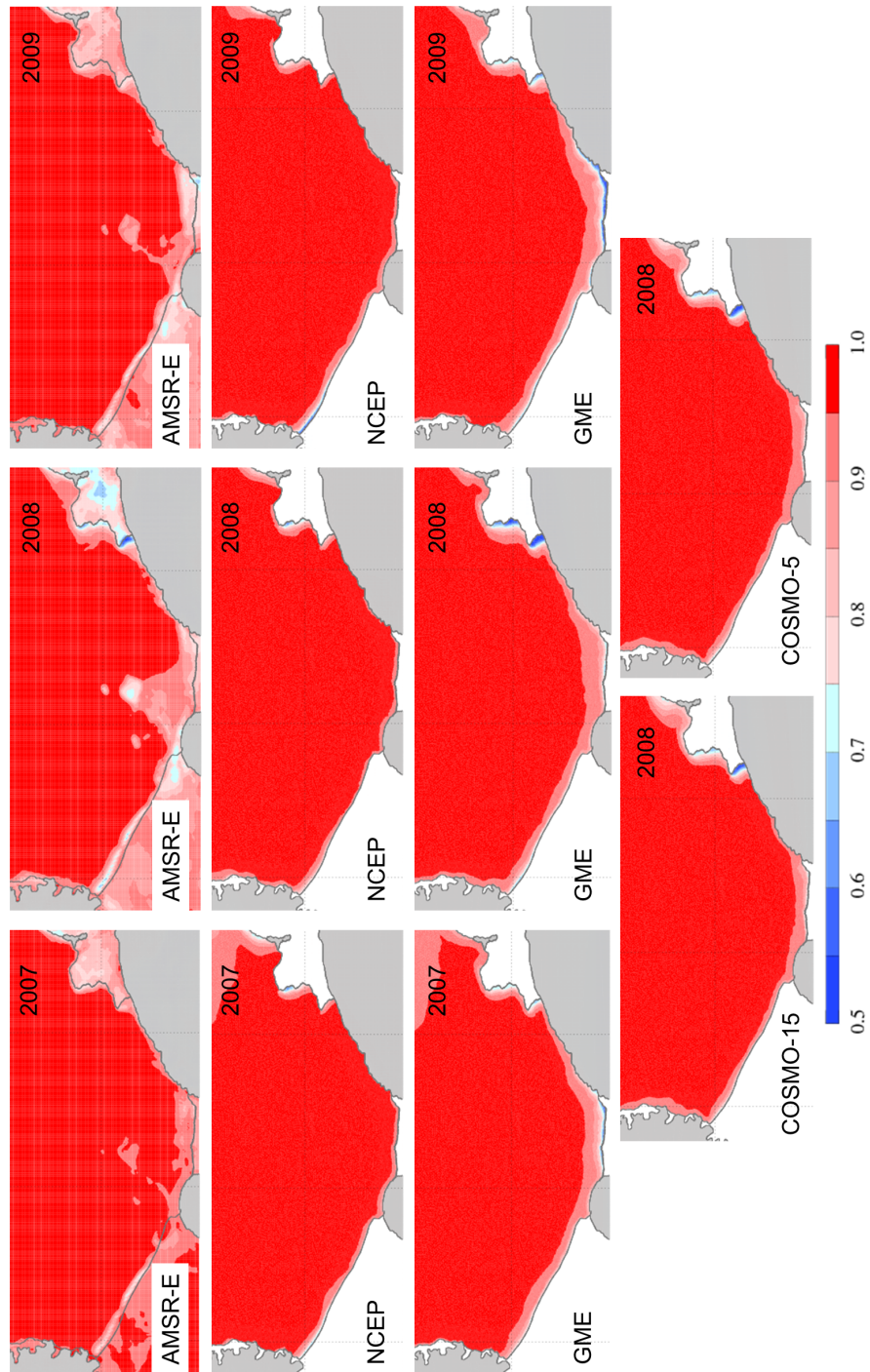


Figure 6.4: Sea ice concentration maps averaged over April-August: AMSR-E observations, NCEP and GME runs for 2007-2009 and COSMO-15 and COSMO-5 runs for 2008. Since the ice shelf fronts are subject to change, the drawn coastline may differ from the actual coastline in the depiction of satellite data (top panels).

to the weak winds, the GME run features the widest and (except in 2008) strongest polynya signature here, which is created by the strong southeasterly winds in this area (Section 6.2.1).

The Ronne polynya in the NCEP run is widest at its western border and narrows toward the east. This is similar to the signature in the satellite observations, while the GME forcing creates a belt of reduced sea ice concentrations of almost invariable width along the Ronne Ice Shelf front, that continues and widens in front of Filchner Ice Shelf and slowly narrows at the Coats Land coastline. However, while the NCEP run often overestimates the gradient of the sea ice concentration at the Ronne polynya, GME features values similar to the satellite measurements.

The eastern polynyas show little interannual variability in the NCEP run (except for a slight weakening in 2009). In the GME run – while overestimating polynya activity – interannual variations are reproduced well (weakest polynyas in 2007, strongest in 2008). Also the often blurred shape of the polynya areas is recreated in the GME run, although not always matching the observations in the details.

In 2008, the COSMO runs yield the best fit to the AMSR-E observations. The sea ice concentrations in both COSMO runs are very similar. The most prominent difference is found at the Antarctic Peninsula coastline, where COSMO-5 matches observations slightly better (and also the NCEP run features a remarkable agreement with the AMSR-E data in this region). Although both COSMO runs underestimate the Ronne polynya width, the eastern polynyas are very well recreated with a strong signature of the southern Brunt polynya and a less active northern Brunt polynya. Even the blurred western edge of the Riiser-Larsen polynya can be found in both the satellite observations and the COSMO runs. Along Filchner Ice Shelf the COSMO runs feature a pattern similar to the GME run, however, it is significantly reduced in extent and intensity. The higher wind speeds in the COSMO data compared to GME data at the Filchner and Ronne Ice Shelf fronts (Figure 6.2) leave no visible trace in the sea ice concentrations.

6.2.4 Sea ice production

In the NCEP run, the highest freezing rates are found at the Ronne polynya (Figure 6.5), followed by the northern Brunt polynya. The GME run features the southern Brunt polynya with higher freezing rates than the northern Brunt polynya and besides Ronne polynya an additional maximum in front of Filchner Ice Shelf. Between years, the relative importance of those regions shifts in the GME run (2007: maxima at Filchner Ice Shelf front and southern Brunt polynya, 2008: maxima at Brunt polynyas, 2009: maximum at Ronne polynya), while in the NCEP run, the relations seem stable and only overall intensity changes (minimum in

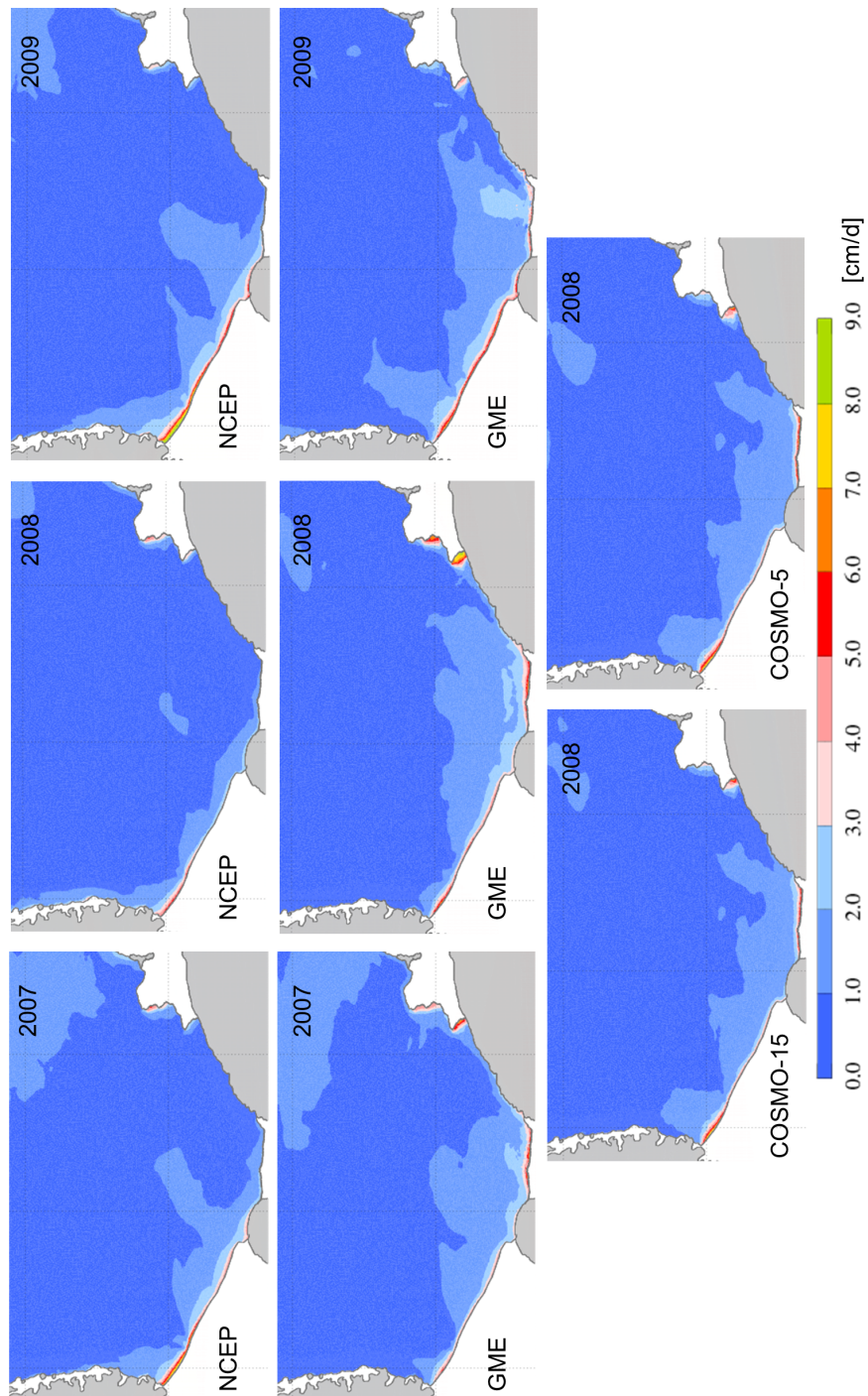


Figure 6.5: Sea ice production maps averaged over April-August: NCEP and GME runs for 2007-2009 and COSMO-15 and COSMO-5 runs for 2008.

2008, maximum in 2009). The only exception in the NCEP run are the western polynyas at the Antarctic Peninsula coastline, which feature maximum ice production in 2008.

These differences can be shortly summed up by stating that most of the sea ice production in the NCEP run occurs on the western part of the continental shelf (connected to Ronne polynya) and in the GME run (except in 2009) it occurs on the eastern part of the shelf at the Brunt polynyas and in front of Filchner Ice Shelf.

The two COSMO runs again yield very similar results. The distribution of the ice production also resembles the results of the GME run, however, while the Ronne polynya west of General Belgrano Bank (ca. 55° W) features higher freezing rates than in the GME run all areas east of 55° W have lower sea ice production, especially the Brunt polynyas. As a result, we find the highest freezing rates at Ronne polynya in the COSMO runs and a more evenly distributed sea ice production along the coastline than in the NCEP or GME runs.

6.3 Bottom salinity and HSSW

During autumn and winter the sea ice production exerts a strong influence on the on-shelf waters by accumulating salt in the water column. Thus, the differences in ice production are propagated to changes in salinity. Over the months April-August, the salinity on the continental shelf increases and, in general, we find the strongest increase in bottom salinity over the shallowest part of the coastline in front of Berkner Island and the eastern part of Ronne Ice Shelf (Figure 6.6). In the NCEP run, also the outer part of the Berkner Bank and the Ronne Depression (except in 2008) feature maxima of bottom salinity increase. With the exception of small areas at the Antarctic Peninsula coastline, the rest of the continental shelf experiences no major salinity increase at the bottom.

The GME run, as seen before in other variables, has more variability in the patterns between years. In 2007, we find similarities to the NCEP run; the bottom salinity increase over Berkner Bank, however, is much stronger, and in the Ronne Depression the change is slightly weaker. Also, we find a substantial increase of the bottom salinity under the southern Brunt polynya and a small local maximum at the southwestern end of the Coats Land coastline.

In 2008, the strong sea ice production along the entire coastline from the Brunt Ice Shelf to the Ronne Ice Shelf in the GME run causes a substantial increase in the bottom salinity on most of the eastern continental shelf. We find maxima at the Brunt polynyas and high values along the eastern slope of Filchner Trough. Again, there is a small maximum at the southwestern end of the Coats Land coastline. The area at the coastline crossing Berkner Bank features an exceptionally high bottom salinity increase and in the west we find a moderate

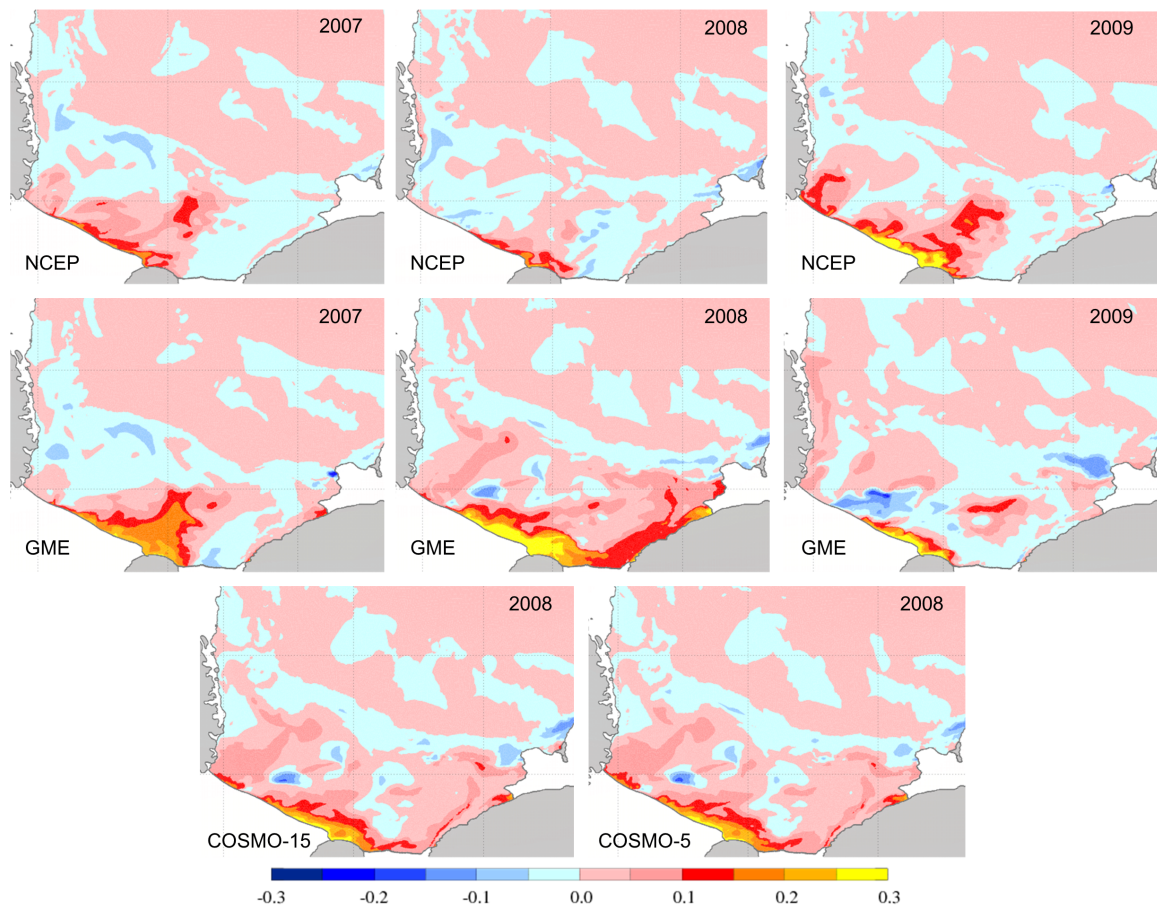


Figure 6.6: Maps of the increase of the bottom salinity between April and August: NCEP and GME runs for 2007-2009 and COSMO-15 and COSMO-5 runs for 2008.

maximum stretching from the Ronne Depression along the western side of General Belgrano Bank to the shelf break.

In 2009, the bottom salinity changes in the GME run are low in most areas of the shelf. Only at the shallow coastline over Berkner Bank, we find a very high salinity increase, but it remains restricted to a relatively small area. Furthermore, there are several small local maxima, the most prominent of which is located at the eastern slope of Berkner Bank and several of these maxima are aligned along the western coastline from Ronne Depression to the southern edge of Larsen C Ice Shelf.

The changes in the bottom salinity in the COSMO runs again result in almost identical patterns. As the distribution of the sea ice production already indicated, the COSMO results show a pattern of salinity changes similar to the GME run, but reduced in the eastern parts

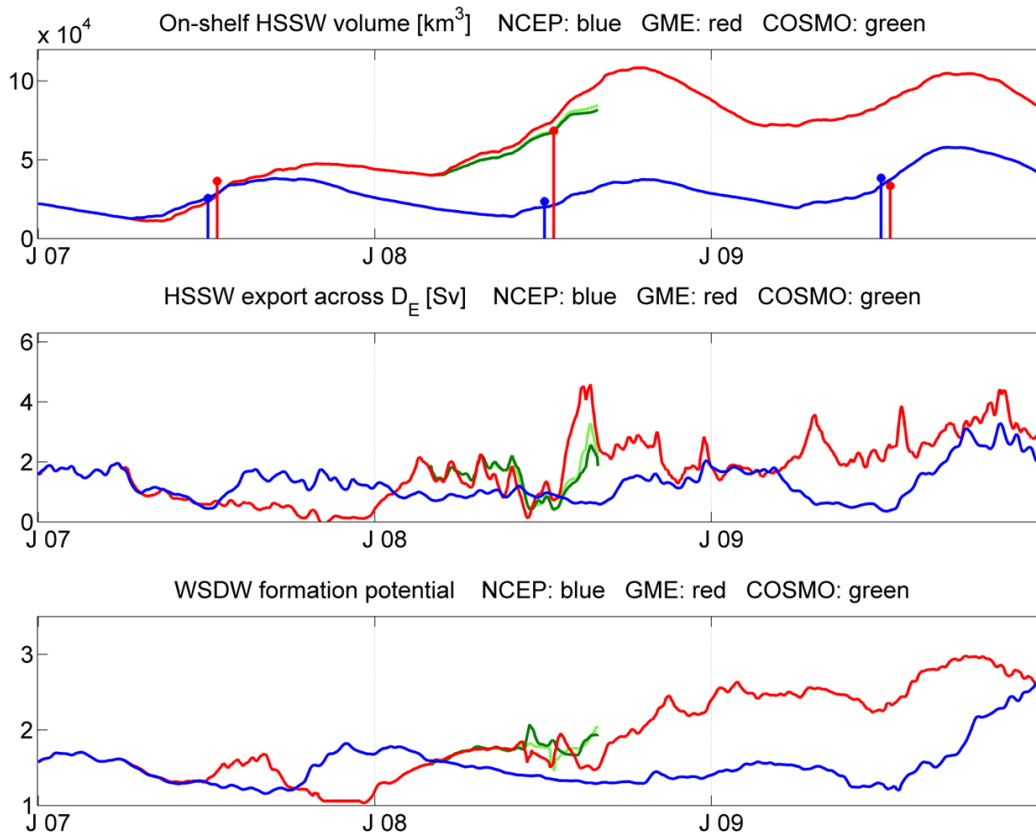


Figure 6.7: On-shelf HSSW volume and seasonal increase (vertical lines; top panel), HSSW export across D_E (Figure 5.6; middle panel) and WSDW formation potential of the exported HSSW (bottom panel) in the NCEP (blue), GME (red), COSMO-15 (dark green) and COSMO-5 (light green) model runs over 2007-2009.

and enhanced in the Ronne Depression. Especially the strong increase of bottom salinity on the eastern flank of Filchner Trough and at the Brunt polynyas is reduced to more moderate maxima and consequently the eastern part of the shelf features lower values.

The changes in salinity have a direct influence on the production of HSSW. In 2007 and 2009 the volume increase of HSSW (Figure 6.7, top panel) is similar in the NCEP and GME runs; in 2008, however, the HSSW volume develops very differently between the runs. Out of the three years, the NCEP run features the lowest production of HSSW ($2.4 \cdot 10^4 \text{ km}^3$) in 2008, while the GME run has a maximum production ($6.8 \cdot 10^4 \text{ km}^3$) in the same year. With the initial volume difference from the previous summer season, this results in a difference of $7.1 \cdot 10^4 \text{ km}^3$ in HSSW volume, most of which ($\approx 4.5 \cdot 10^4 \text{ km}^3$) is maintained over the course of the following year. In the COSMO runs the HSSW volume features a similar behaviour as in the GME run, but the increase is slightly less steep, which is consistent with the smaller

ice production in these experiments.

Since in 2007 much of the HSSW in the GME run is produced near Berkner Island, it has to be advected far to the west and north, before reaching the western shelf break where most HSSW leaves the continental shelf. The export of HSSW in the GME experiment therefore drops to almost zero at the end of the year (Figure 6.7, middle panel) and causes the HSSW volume to increase even late in the year. In 2008, HSSW production occurs extensively in the eastern part of the shelf and also in the west over the Ronne Depression. The HSSW volume reaches very high values and covers most of the shelf, export recommences and the rates increase rapidly at the end of July and peak in August with a maximum of 4.6 Sv. Thereafter, the HSSW export drops again, but in 2009 HSSW export rates feature an increasing trend.

The HSSW export in the NCEP run during most of the three-year period features maxima of ≈ 2 Sv and minima of ≈ 0.5 Sv, alternating in a rugged seasonal cycle. In the spring of 2009, however, export maxima of 3.5 Sv are reached. In the mean, this gives an export rate of 1.3 Sv for the NCEP run, while the GME run yields a higher mean export of 1.7 Sv. The HSSW export rates of the COSMO during the first half of the experiment feature higher export rates than the GME run, however in the second half their values stay below the GME results. Unfortunately, the time series are too short to derive specific conclusions on the behaviour on longer time scales.

The changes of the WSDW formation potential (Section 5.5.1) of the exported HSSW in both NCEP and GME simulations displays rough similarities to those of the HSSW export rates (Figure 6.7, bottom panel). In the GME run, it drops to very low values during 2007, but increases over the years 2008 and 2009 to values of ≈ 3.0 (October 2009). In the NCEP run, the WSDW formation potential of the exported HSSW fluctuates between values of 1.2 and 1.8 for most of the three years until in the second half of 2009 it increases to reach values ≥ 2.6 at the end of the year.

The mean potential WSDW formation is the product of HSSW export and WSDW formation potential. In the GME run high export rates coincide with a high formation potential during half of the time considered, which yields a mean potential WSDW formation of 3.8 Sv, while the NCEP run with mostly moderate values of the potential only gives 2.1 Sv of WSDW formation. The WSDW formation potential in the COSMO runs after the first months differs from the GME results featuring a tendency to higher values.

6.4 Polynya events and variability

To investigate the short term variability of the different atmospheric data sets, a comparison of areal means in the Ronne region in the period April-August 2008 is presented in this

section. The Ronne region (Figure 4.1) was chosen, because it was identified as the most active and therefore most influential polynya region of the southwestern Weddell Sea in the long-term run (Sections 4 and 5) as well as in previous studies (e.g. Markus et al., 1998).

We generally find anomalies of wind direction, wind speed, air temperature and polynya area occurring consistently over all four data sets (Figure 6.8), but the magnitude of anomalies differs strongly. The NCEP data exhibits the least day-to-day variation in the wind direction (Figure 6.8, top left panels). A southerly component is persistent during the investigation period, usually combined with a weak westerly component (180° - 220° wind direction). In the GME wind field the spread of directions is larger. The range from 120° - 270° is well covered (with an emphasis on $\approx 200^{\circ}$), but also northerly and northeasterly directions occur occasionally (distinctly more often than in the NCEP data). The COSMO wind fields display more variability than the NCEP winds, but still more focused directions than the GME winds. The main direction is southwesterly (180° - 240°) but also southeasterly (mainly $\approx 150^{\circ}$) and northeasterly directions (mainly $\approx 60^{\circ}$) are common, while northwesterly winds are very rare.

Polynyas in all experiments open on days when wind directions from the southwest prevail, with one exception in the NCEP run, when on day 214 a small polynya opens at wind direction 285° (westerly) with the regional mean at 300° . This polynya, however, is an extension of an opening along the Antarctic Peninsula that reaches south into the Ronne region. Apart from this event, in the NCEP run opening wind directions between 210° - 230° are found. The local wind at the polynya formation site always features a stronger westerly component than the regional mean. In the GME run, polynyas are created at a similar but wider range of wind directions (190° - 240°), while the COSMO runs feature polynyas opening at wind directions between 200° and 230° .

It seems that in order to create polynyas in the Ronne region, the NCEP forcing needs a slightly stronger westerly component in the wind than the other data sets. This is probably due to the large scale wind field in 2008 (Figure 6.2), where in the GME and COSMO runs the southwesterly winds drive the ice out of the Weddell Sea basin, while in the NCEP run the mean wind field does not favour polynya formation similarly. Together with the fact that strong westerly components are rare in the NCEP wind, this causes the polynyas to be very infrequent in the NCEP case with only 55 polynya days (Table 6.1). The GME run has the most frequent polynyas with 101 days and the two COSMO runs feature 85 days (COSMO-15) and 86 days (COSMO-5) of polynyas. The size of the created polynyas is generally largest in the GME run. Over the investigation period the daily polynya area has a mean of 790 km^2 in the NCEP case, 1800 km^2 for the GME run and 1000 km^2 (1200 km^2) with COSMO-15 (COSMO-5) forcing.

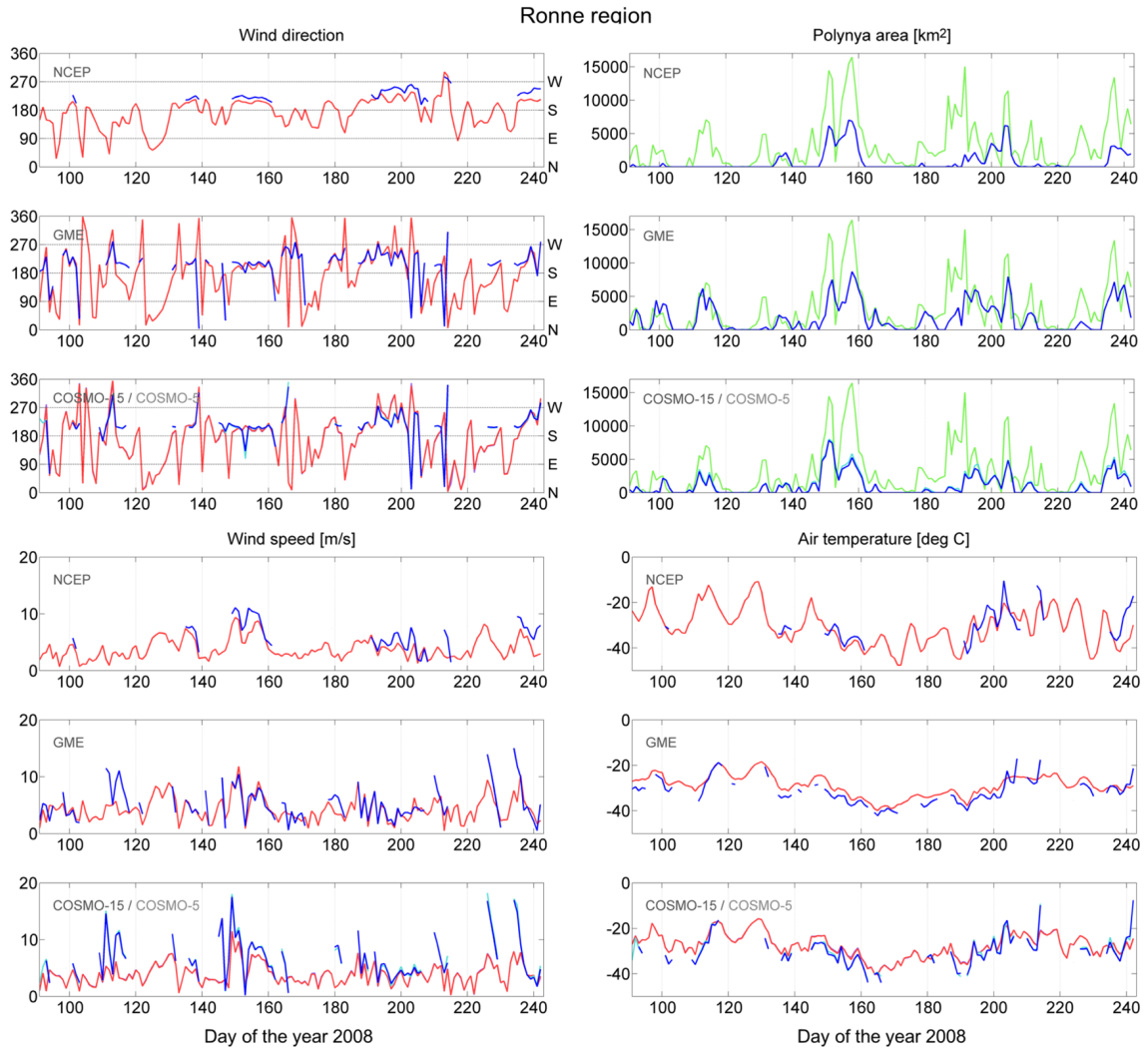


Figure 6.8: Wind direction, polynya area, wind speed and air temperature in the Ronne region for April-August 2008; regional mean (red) and mean over the polynya area (blue; only when polynya is open). The green line (identical in all top right panels) marks the polynya area derived from AMSR-E data. all time series are based on daily mean values.

A comparison with the polynya area from the satellite images (Figure 6.8, top right panels) reveals that all model runs substantially underestimate the polynya area in the Ronne region. The smallest root mean square (rms) error is achieved by the GME run (3000 km²). The COSMO runs yield rms errors of 3500 km² (COSMO-15) and 3400 km² (COSMO-5), and the NCEP results are farthest from the observations with an rms error of 3700 km². It must be kept in mind that the size of the polynyas alone does not give information about the ice concentrations within the polynya and the resulting surface fluxes. As could be seen in Figure 6.1, the AMSR-E images often show sea ice concentration between 30 % and 70 % in the area of Ronne region, while the model tends to create either high sea ice concentrations > 80 % or very low ice concentrations < 30 %. The resulting ice formation is therefore likely to be much more realistic than the comparison of polynya area might suggest.

The (small) difference in polynya area between the COSMO runs is primarily due to the often (but not always) higher wind speed of the COSMO-5 data (Figure 6.8, bottom left panel). For the regional mean wind speed, anomalies are generally stronger in the GME data than with NCEP forcing. Over the polynyas, however, the GME forcing usually has lower wind speeds than both COSMO runs and occasionally than the NCEP run.

With regard to air temperatures (Figure 6.8, bottom right panels), the NCEP forcing shows the highest variability. It features the overall maximum as well as the overall minimum temperatures. In the NCEP case, we find locally higher temperatures at polynyas, in the GME and COSMO runs, however, the temperatures over the polynyas are generally lower than the regional mean. This is an artefact caused by the use of different land masks in the atmospheric and oceanic models (see also Section 6.2.2) and causes a bias to higher values in the sea ice production.

Of the four experiments analysed here, the regional mean sea ice production per unit area (Figure 6.9, left panels, red lines) is lowest in the NCEP run. The GME run on average has higher values than the COSMO-5 results, which in turn feature a slightly higher sea ice production per unit area than the COSMO-15 results. Neither the regional mean nor the polynya sea ice production per unit area of the Ronne region feature a seasonal signal over the investigation period.

The NCEP forcing episodically induces high ice production per unit area over polynyas in the Ronne region (maximum: 25 cm/d on day 155; mean heat flux to the atmosphere over polynyas: 456 W/m², thereof 420 W/m² from latent heat release). However, due to the small number of polynya days, this only accumulates to the production of 18 km³ of ice during the investigation period, which is 11 % of the total ice production within Ronne region in the NCEP run.

The GME run also has a maximum rate of 25 cm/d (day 227) but the area-weighted mean

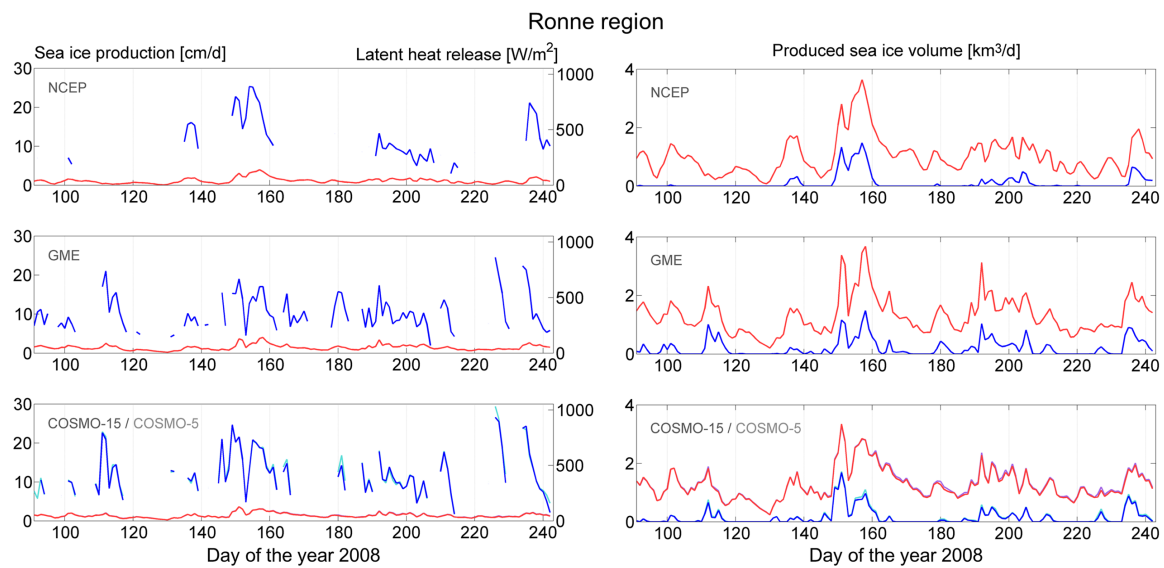


Figure 6.9: Sea ice production per unit area (or corresponding latent heat release) and accumulated sea ice production in the Ronne region for April-August 2008; regional mean (red) and mean over the polynya area (blue; only when polynya is open).

over the polynyas (11.3 cm/d; mean atmospheric heat flux over polynyas: 396 W/m², thereof 363 W/m² from latent heat release) is lower than the corresponding value of the NCEP run (14.7 cm/d). However, the GME forcing yields approximately twice as many polynya days and the large area (cf. Figure 6.8) leads to an accumulated sea ice production of 32 km³ (16 % of the regional ice production).

The COSMO runs feature the highest polynya sea ice production per unit area, (maxima: 27 cm/d in the COSMO-15 run and 29 cm/d in the COSMO-5 run, both on day 227) induced by a high atmospheric heat flux over the polynyas (mean: 470 W/m² in COSMO-15 and 476 W/m² in COSMO-5, thereof 430 W/m² and 438 W/m², respectively, from latent heat release). The COSMO-15 run yields 23 km³ of ice production in the polynyas of Ronne region, slightly surpassed by the COSMO-5 run with 25 km³, which corresponds to 12 % (COSMO-15) and 13 % (COSMO-5) of the total regional production. The total sea ice production found in the NCEP and COSMO runs features a remarkable agreement. The slightly higher sea ice production in the COSMO runs is probably due to the cold air temperatures we find at the Ronne Ice Shelf front in these forcings.

Kwok and Comiso (2002) found low sea ice production in the Weddell Sea to coincide with positive SOI events (due to a larger scale anomaly that increases the northerly component of the basin-scale wind field). Their studies, however, are also based on data from the

Ronne region		pol. days	pol. area		wind	air temp.	ice prod.	polynya ice production		
			km ²	%	m/s	°C	cm/(d·m ²)	cm/(d·m ²)	km ³	%
2007	NCEP	72	1100	1.2	4.6	-34.8	1.5	16.3	28	13
	GME	84	1400	1.5	4.8	-31.6	1.3	11.6	25	13
2008	NCEP	55	790	0.9	4.3	-30.3	1.1	14.7	18	11
	GME	101	1800	2.0	5.1	-28.9	1.4	11.3	32	16
	COSMO-15	85	1000	1.1	4.6	-27.7	1.4	14.3	23	12
	COSMO-5	86	1200	1.3	4.6	-27.6	1.4	14.4	25	13
2009	NCEP	84	1500	1.6	4.7	-35.7	1.7	17.3	40	16
	GME	114	2300	2.5	5.0	-30.4	1.8	12.0	43	17

Table 6.1: Number of polynya days and mean values of polynya area (averaged over the entire period), wind speed, air temperature and ice production in the Ronne region for the period April to August in the years 2007-2009. Polynya area is also given in percent of the region's area and polynya sea ice production is given in percent of the region-wide ice production.

Antarctic Peninsula region		pol. days	pol. area		wind	air temp.	ice prod.	polynya ice production		
			km ²	%	m/s	°C	cm/(d·m ²)	cm/(d·m ²)	km ³	%
2007	NCEP	38	120	0.1	5.0	-24.6	0.56	9.8	1.7	2.0
	GME	37	320	0.3	4.8	-24.8	0.50	4.6	2.2	2.8
2008	NCEP	51	1200	1.1	5.2	-21.8	0.66	6.9	12	12
	GME	54	960	0.9	5.0	-24.1	0.41	2.8	4.1	6.4
	COSMO-15	30	860	0.8	4.6	-23.5	0.53	2.2	3.1	3.6
	COSMO-5	30	840	0.8	4.6	-23.4	0.55	2.5	3.3	3.6
2009	NCEP	51	610	0.6	5.1	-25.4	0.64	5.9	5.4	5.4
	GME	29	560	0.5	5.0	-24.2	0.62	4.8	4.1	4.2

Table 6.2: Number of polynya days and mean values of polynya area, wind speed, air temperature and ice production in the Antarctic Peninsula region for the period April to August in the years 2007-2009. Polynya area is also given in percent of the region's area and polynya sea ice production is given in percent of the region-wide ice production.

NCEP/NCAR Reanalysis. The differences we find in the La Niña/positive SOI year 2008 between the different atmospheric data sets give rise to the question whether the anomalies found by Kwok and Comiso (2002) are robust against a change of the data set.

6.5 Quantitative overview

In this section, a summarized overview of the most important variables is presented in tables for four regions: the Ronne region, the Antarctic Peninsula region, where the spatial resolution of the forcing data is expected to be of great influence due to the rough topography of the coast, the Coats Land region (Figure 6.10, where the ocean is not bordered by ice shelves and the influence of katabatic winds is expected, and the entire region of the Southwestern

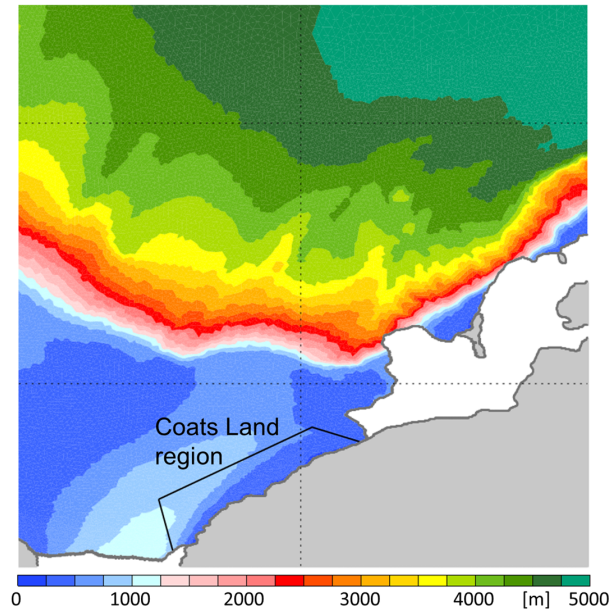


Figure 6.10: The boundaries of Coats Land region.

Weddell Sea.

The Coats Land region is considered more interesting than the Brunt polynyas when comparing results of different forcing data sets, because here mountains border the coastline without a separating ice shelf. Therefore, katabatic winds originating from the higher regions cross the coastline with little deceleration and the resolution of the atmospheric model is thought crucial for the representation of katabatic winds. It is therefore expected and seen in Section 6.2 that the four model runs yield different results. The boundaries of the Coats Land region are defined by the corner coordinates $37.44^\circ \text{ W} / 77.22^\circ \text{ S}$, $29.40^\circ \text{ W} / 75.84^\circ \text{ S}$, $22.17^\circ \text{ W} / 76.64^\circ \text{ S}$ and $36.67^\circ \text{ W} / 78.24^\circ \text{ S}$.

The overview of the mean values of the most important quantities in the Ronne region (Table 6.1) shows that 2008 (discussed in detail in the previous section) is the year with the largest differences between NCEP and GME forcing. In 2007 and 2009, we generally find a much better agreement between the NCEP and GME results than in 2008. Only the polynya sea ice production per unit area of the NCEP run is even higher than in 2008 because of the higher wind speeds.

In the Antarctic Peninsula region (Table 6.2), NCEP and GME forcing agree well except in the year 2008. However, even in 2008 both runs result in more frequent and larger coastal polynyas than the high-resolution COSMO data sets. We already found in Section 6.1 (Figure 6.1) that both coarser forcing data sets have difficulties to create coastal polynyas realis-

Coats Land region		pol. days	pol. area		wind m/s	air temp. °C	ice prod. cm/(d·m ²)	polynya ice production		
			km ²	%			cm/(d·m ²)	km ³	%	
2007	NCEP	10	24	0.1	4.0	-27.0	0.58	4.9	0.2	0.9
	GME	84	670	3.3	4.3	-27.1	1.2	6.5	6.6	18
2008	NCEP	16	37	0.2	4.6	-25.0	0.56	5.0	0.3	1.6
	GME	118	900	4.4	6.2	-22.7	1.6	8.1	11	22
	COSMO-15	85	300	1.5	5.4	-21.8	0.83	6.9	3.2	12
	COSMO-5	83	360	1.8	5.6	-21.7	0.90	7.1	4.0	14
2009	NCEP	4	34	0.2	3.4	-30.0	0.62	4.1	0.2	1.3
	GME	132	1400	6.6	5.2	-24.6	0.80	4.7	9.6	39

Table 6.3: Number of polynya days and mean values of polynya area, wind speed, air temperature and ice production in the Coats Land region for the period April to August in the years 2007-2009. Polynya area is also given in percent of the region's area and polynya sea ice production is given in percent of the region-wide ice production.

tically at the Antarctic Peninsula coastline due to the rough topography. Since in 2008 the sea ice production per unit area is highest in the NCEP run, especially within the polynyas, during the period April-August 2008 the polynya ice production in the NCEP run yields a multiple of the volume found in the GME run, which in turn is higher than but agrees comparatively well with the results of the COSMO runs.

In the Coats Land region (Table 6.3), the NCEP run features hardly any polynyas, because the mean wind field (Figure 6.2) in this region is parallel to the coast (causing ice drift toward the coastline) and also has the lowest variability compared to the other atmospheric data sets. In the GME run, we find frequent and very large polynyas at the Coats Land coastline (Figure 6.4) facilitated by the more easterly mean winds and the higher variability of the wind direction. In the Coats Land region a strong influence of katabatic winds is expected and high resolution in the atmospheric model is thought essential for a realistic reproduction of katabatic winds (Jourdain and Gallée, 2011). The COSMO runs, which fulfill this requirement best, feature polynyas less frequent and smaller than the GME run and the resulting polynya ice volume is much smaller than in the GME run. It is therefore assumed that the polynya formation and sea ice production in the Coats Land region is overestimated in the GME run.

For the entire area of the Southwestern Weddell Sea (Table 6.4) many regional differences compensate each other and most variables feature only small differences between the different forcing data sets. The very large 'polynya area' in 2007 includes areas of open water, that are remnants of the summer season and have not yet been ice-covered in April. The NCEP run by a clear margin features the lowest wind speeds and therefore typically the smallest and least frequent polynyas. However, while also the regional sea ice production per unit area is

Southwestern Weddell Sea		pol. days	pol. area		wind m/s	air temp. °C	ice prod. cm/(d·m ²)	polynya ice production			
			km ²	%				cm/(d·m ²)	km ³	%	
2007	NCEP	137	33000	2.3	4.1	-27.1	0.65	2.6	129	9.1	
	GME	140	31000	2.2	5.2	-25.7	0.75	3.0	143	8.8	
2008	NCEP	140	6900	0.48	4.2	-23.6	0.48	7.0	74	7.0	
	GME	147	9800	0.67	5.7	-23.4	0.54	6.8	101	8.6	
	COSMO-15	148	9300	0.65	4.8	-22.7	0.50	4.8	67	6.2	
	COSMO-5	145	8500	0.59	5.0	-22.7	0.52	5.6	72	6.4	
2009	NCEP	147	8800	0.61	4.0	-26.9	0.57	5.7	76	6.1	
	GME	152	13000	0.92	5.5	-24.2	0.61	5.2	105	7.9	

Table 6.4: Number of polynya days and mean values of polynya area, wind speed, air temperature and ice production in the Southwestern Weddell Sea for the period April to August in the years 2007-2009. Polynya area is also given in percent of the region's area and polynya sea ice production is given in percent of the region-wide ice production.

the lowest, the NCEP run often has the highest freezing rates in its polynyas. In 2008, the polynya-produced ice volume of the NCEP run is even slightly larger than the ice volumes produced in the COSMO runs. The GME run stands out due to the highest wind speeds and the largest polynyas, resulting in all years in the highest sea ice volume produced in polynyas and in the entire region.

6.6 Chapter summary

To investigate the impact of differences in the atmospheric forcing data on the extent of coastal polynyas, sea ice production and on-shelf water properties in the southwestern Weddell Sea, simulations using atmospheric forcing data from GME and two configurations of the regional COSMO model were branched off from the NCEP-forced reference simulation. GME and NCEP forcing fields and results were compared for three consecutive autumn/winter periods (April-August 2007-2009); COSMO data was available for the comparison only for 2008.

Comparisons with satellite images of the sea ice concentration show that both COSMO forcings perform very well; differences between the COSMO runs occur only in details, but the higher-resolved COSMO-5 data set has a slight advantage. Especially next to mountainous topography, high resolution in the forcing data is necessary to reproduce the channelled wind flow and create polynyas with a realistic shape. However, in a comparison of the polynya area (neglecting shape and sea ice concentrations apart from the threshold value) in the Ronne region in 2008, the GME run achieved the best match with the AMSR-E observations. While the NCEP forced run tends to underestimate polynya size (with exception

of the Antarctic Peninsula region), the GME run seems to overestimate polynya formation (especially on the eastern part of the shelf). The most striking difference between the two coarser data sets is found in front of Filchner Ice Shelf, where the effects of the iceberg A23 prevent a clarifying comparison to satellite data.

The mean wind field reveals substantial differences between the forcings. At the coastline of the Antarctic Peninsula, where the NCEP forcing features a wind speed maximum with southwesterly wind directions, the GME data feature weak southerly winds. Also at the Brunt Ice Shelf the NCEP wind speed has a maximum, while the GME data – except in 2008 – features reduced wind speeds. In general, however, GME features the strongest winds of all data sets.

An evaluation of variability shows that all major short-term events are found in all four atmospheric data sets. However, the NCEP wind field shows the least variability, while the NCEP air temperatures feature the highest fluctuations on time scales of several days. In the mean, NCEP features the coldest air temperatures and those of the COSMO forcings are warmest. Over the polynyas, however, the NCEP data features higher values than in the surrounding area, but GME and COSMO forcings in some areas feature spurious colder air temperatures due to differences in the land masks of atmosphere and ocean model.

The sea ice formation, which is highest in coastal polynyas and therefore very dependent on the wind field, is most active in the GME run. The most notable difference to the NCEP run is the strong activity on the eastern part of the continental shelf. Also, in the COSMO runs we find substantial ice production in the east, but less than in the GME run; the ice formation of the COSMO runs at the westernmost part of Ronne Ice Shelf is higher than in both NCEP and GME runs (since NCEP features exceptionally little polynya activity in 2008).

The year 2008 is not a typical year, but is affected by a La Niña / positive SOI event. While in the GME run the largest polynyas are formed and consequentially ice production is high, the NCEP forcing features the least activity in this year. In both data sets, we can see a strengthened cyclonic flow in the mean wind field, however, in the GME data it is located far east and causes strong southwesterly winds over the central open ocean that drive the sea ice north and out of the basin, while in the NCEP forcing its center is further west and sea ice drift out of the basin is not supported.

If 2008 is not considered, NCEP and GME forcing agree well in Ronne region, while e.g. at the Coats Land coastline the differences (NCEP: almost no polynyas, GME: large polynyas) are persistent. In a basin-scale consideration, most of the local differences in sea ice formation compensate each other and the results from the different atmospheric forcings agree well.

For the ocean's salinity not only the quantity but also the distribution of sea ice formation is of importance. The area in front of Berkner Island and the western Ronne Ice Shelf, due to its shallow water column, always features the highest increase in salinity. In the NCEP run, the Ronne Depression and the outer part of Berkner Bank usually are further maxima of salinity increase, while in the GME run we find patterns changing between years. In 2008, we find a very low salinity increase in the NCEP run, while the GME run features a strong salinity increase not only in the eastern areas between Brunt Ice Shelf and Berkner Bank, but also along the Ronne Ice Shelf front and in Ronne Depression. Compared to the GME pattern, the COSMO runs feature less salinity increase in the eastern regions, but an amplified salinity increase in the area of the Ronne Depression.

In consequence, the HSSW volume increases strongly in 2008 in the GME experiment, but only little in the NCEP simulation, while in 2007 and 2009 the increase in HSSW volume is similar in both cases. However, the strong increase of HSSW volume in the GME experiment in 2008 affects the total HSSW volume present on the shelf (and thus the salinity) in the subsequent years. The export of HSSW is higher with GME forcing and its variations differ strongly from the export found in the NCEP simulation. The mean export for the three year period is 1.3 Sv in the NCEP simulation and 1.7 Sv in the GME experiment. A consideration of the WSDW formation potential reveals that the HSSW in the GME experiment can sustain stronger mixing and potentially form 3.8 Sv of WSDW, while the potential WSDW formation in the NCEP run is only 2.1 Sv.

7 Conclusions and outlook

In this study, the coastal polynyas in the southwestern Weddell Sea were investigated during the winter season in the time period from 1990 to 2009 using a suite of simulations conducted with the finite-element sea ice-ocean model FESOM. The formation and size of coastal polynyas was evaluated and their contribution to the heat flux and sea ice production of the southwestern Weddell Sea was quantified. Their influence on the salinity on the continental shelf as well as volume and export of HSSW were assessed and the possible formation of WSDW was estimated. The robustness of the simulation forced with NCEP/NCAR Reanalysis data against changes in the forcing was tested by comparisons with shorter, branched-off experiments using atmospheric data from the GME and COSMO models.

We find the typical winter situation, where small coastal areas are held open by offshore winds and high heat fluxes and strong sea ice formation occurs, during the months May-September. In the long-term run with NCEP forcing, the most active polynyas in the Weddell Sea are located in the east at Brunt Ice Shelf, in the south in front of Ronne Ice Shelf, and in the west along the southern part of the Antarctic Peninsula coastline. In the 20-year winter mean, the Ronne polynya is largest with 2000 km², the Antarctic Peninsula coastline features polynyas of 1700 km², while at the Brunt Ice Shelf we find 1000 km² of polynyas. The interannual variability, however, is very high and the dependence on the forcing data (above all the wind field) is strong. In the 33-month run with GME forcing, also the front of Filchner Ice Shelf and the coastline of Coats Land feature high polynya activity due to differences in the wind field in this higher-resolution data set.

At the coastal polynyas, we find a heat flux to the atmosphere which in the 20-year winter mean exceeds the heat flux at the surrounding ice-covered areas by a factor of 7-9. It is highest in the Ronne polynya, where the mean over the five winter months gives 510 W/m², while the mean in the polynyas at the Brunt Ice Shelf yields 310 W/m². At the Antarctic Peninsula coastline we find 370 W/m² in the reference simulation. In the winter mean over 60 % of the atmospheric heat flux at coastal polynyas is due to the sensible heat flux. With its dependence on the product of air temperature and wind speed the sensible heat flux is also the dominant factor for the variability of the atmospheric heat flux. In the ice-covered areas, the variability of the heat flux to the atmosphere is also strongly influenced by the sensible

heat flux, but the major contributor in the winter mean is the longwave radiation.

The erosion of the ocean's heat content compensates for 10-20 % of the atmospheric heat flux at coastal polynyas. The high oceanic heat flux at coastal polynyas (50-60 W/m²) is made possible by year-round intrusions of Modified Warm Deep Water onto the shelf and the vertical convection that is generated by the surface salinity increase due to sea ice production. In ice-covered areas, the oceanic heat flux is lower (16-20 W/m²), but contributes to the total atmospheric heat flux at a much higher percentage.

The major part of the atmospheric heat flux at coastal polynyas (80-90 %) is compensated by the latent heat gained in sea ice formation. We find 20-year winter mean ice production rates of 7-13 cm/d per unit area in the polynyas of the three most active regions, which are 9-14 times higher than the mean ice production rates of the surrounding ice-covered areas. The sea ice volume produced in coastal polynyas is the product of ice formation rate and polynya area, which gives it a high interannual variability and a strong dependence on the forcing.

The southwestern coastal polynyas (especially Ronne polynya) are the source regions of the densest shelf waters, and the regional sea ice production in the southwestern corner is the most influential factor for the on-shelf HSSW volume in the NCEP simulation. This is different in the GME experiment, where much more sea ice is produced in the eastern region between Brunt Ice Shelf and Berkner Island. Thus, the influence of the eastern region on the salinity of the on-shelf waters is substantially higher and we find HSSW also in regions further east and thus in larger volumes. However, in reality today the formation of coastal polynyas in front of Filchner Ice Shelf is largely prevented by the presence of iceberg A23, and thus the regions east of Berkner Bank are currently not likely to be of large influence on the salinity of the on-shelf waters.

The export of HSSW generally is correlated with the on-shelf HSSW volume. Thus it is influenced by the seasonal cycle, but even more by the interannual variability. In the NCEP run, maximum export rates of 6 Sv were observed, the 20-year mean, however, is 2 Sv. In comparison, the GME run yields higher export rates due to a larger HSSW volume, which is primarily due to the differences caused by the 2008 wind fields.

Since the resolution on the continental slope of this implementation of FESOM is not sufficiently high to allow for the dense water to descend into the deep Weddell Sea, the model does not provide direct information about deep and bottom water formation. To overcome this shortcoming, a pseudo water mass, the High Salinity Mixing Partner, is introduced and an additional property, the WSDW formation potential, is defined. On the basis of several assumptions, an estimate for WSDW formation fueled by water mass modification on the Weddell Sea continental shelf gives 4-6 Sv as a long term mean.

The deep water formation in the GME experiment is higher than in the NCEP simulation due to higher export rates of HSSW, which also has a higher WSDW formation potential. These differences are very strongly influenced by the representation of 2008's La Niña/positive SOI event, which shows substantial differences between the NCEP and the GME runs. While both data sets feature an enhanced cyclonic pattern in the local wind field, the cyclonic gyre in the GME data is located farther east and facilitates sea ice drift out of the Weddell Sea and thus polynya formation. In the NCEP case, the central location of the gyre causes more coast-parallel winds, which do not support polynya formation.

The COSMO data sets are unfortunately only available for 6 months in 2008 and received their boundary conditions from the GME data. However, the results of the COSMO runs are closer to the results from the NCEP simulation in Ronne region. In Coats Land region, the NCEP-forced run probably underestimates polynya formation, but also the COSMO forcing, which has a high resolution, but is not entirely independent of the GME data, yields much lower polynya areas and sea ice formation rates than the GME forcing. In the basin-wide consideration the produced sea ice volume agrees very well between NCEP and COSMO runs.

Contrary to our expectations, we do not find a consistent improvement of the results when going from low-resolution forcing to high-resolution forcing. Instead, the two runs with coarser forcing typically give two extreme values between which we find the runs with the high-resolution COSMO forcing. The results of the COSMO-5 run match the satellite sea ice concentrations in 2008 best, but a general decision whether the NCEP or the GME forcing is a better data set can not be made on the basis of the three years available. The region off Filchner Ice Shelf, where the most prominent differences between the two data sets occur, is unfortunately not comparable to satellite measurements, since the iceberg A23 strongly influences the sea ice drift in that region, but is not represented in the model.

A logical next step after this study would be a more precise quantification of deep and bottom water formation. To simulate the transformation of dense shelf water into WSDW or WSBW a model geometry with very high resolution close to the ocean floor on the continental slope is necessary. This is probably best accomplished with topography-following σ -layers, where the resolution can be increased specifically in the lowermost levels while in other areas computation time can be reduced. With such a model, also much could be learned about the quantity, properties and pathways of water leaving the Weddell Sea.

Another interesting aspect is the contribution of ISW outflow to the deep and bottom water formation. The introduction of ice shelf cavities to the high-resolution model would allow for the simulation of the modification of HSSW into ISW and help quantify the ISW transport out of the Filchner Trough and – with sufficient resolution on the continental slope –

formation rates of WSBW and WSDW.

Furthermore, the knowledge about the on-shelf processes in the Weddell Sea would be increased by the addition of tides in the model. Here, a short-term study (and a comparison with the results of this study) would probably suffice, but it would require a forcing data set with an adequately high temporal resolution (as e.g. the regional COSMO model in this study).

The large differences found in the atmospheric fields of the southwestern Weddell Sea between the GME and the NCEP data set, although they are analysis and reanalysis products, are largely owed to the sparsity of data. Generally, all endeavors to model the Weddell Sea region, both oceanographic and atmospheric, would benefit substantially from the continued acquisition of measurements in the region.

8 Acknowledgements

This thesis was written at Alfred-Wegener-Institut Helmholtz-Zentrum für Polar- und Meeresforschung in the Climate Dynamics research group. My thanks go to Deutsche Forschungsgemeinschaft for the financing of my work as part of project 'Ice-ocean-atmosphere interactions in the western Weddell Sea: Coastal polynyas, cyclones and bottom water formation' in SPP 1158 under grant number TI 296/5.

I express my thanks to Prof. Dr. P. Lemke for his support and supervision and reviewing of this thesis and I am very grateful to Prof. Dr. G. Heinemann for the friendly and successful collaboration and his readiness to assess this thesis.

I give my thanks to Ralph Timmermann for his advice and support and many discussions and to Lars Ebner for his help and collaboration.

I would like to thank Thomas Hollands and Wolfgang Dierking for their productive collaboration and inspiration.

My thanks go to Hartmut Hellmer and Jens Schröter for giving me advice and support, to Qiang Wang and Sergey Danilov for help to get acquainted with the model and to Agnieszka Beszczynska-Möller for giving me the opportunity to participate in the ARKXXVII/1 cruise with RV Polarstern.

I would like to thank NOAA Climate Diagnostics Center, Boulder, USA, for the provision of the NCEP/NCAR Reanalysis data via the website <http://www.cdc.noaa.gov>, Lars Ebner and Prof. Dr. G. Heinemann for the supply of GME and COSMO data sets, and Hannelore Witte and Wolfgang Dierking for the preparation and supply of ULS data.

Finally, I would like to extend my gratitude to all my colleagues, especially Sandra-Esther Brunnabend, Claudia Wekerle, Grit Freiwald, Laura Jensen, Vibe Schourup-Kristensen, Xuezhong Wang, and Madlen Gebler for help, discussions, coffee and cake.

"Difficulties are just things to overcome, after all."

Sir Ernest H. Shackleton

List of Variables and Abbreviations

Variables

A	sea ice concentration
A_h	horizontal momentum diffusion coefficient
A_v	vertical momentum diffusion coefficient
C	cloud factor
C	relative cloud cover
c^*	empirical factor in ice strength
$c_{d,ao}$	atmosphere / ocean drag coefficient
$c_{d,io}$	ice / ocean drag coefficient
c_e	transfer coefficient of latent heat
$c_{h,io}$	heat transfer coefficient
$c_{p,o}$	specific heat of water at constant pressure
D_A	sea ice concentration change
D_D	divergence
D_{h_i}	thermodynamic sea ice growth rate
D_{h_s}	snow layer growth rate
D_S	horizontal shear strain rate
D_T	horizontal tension strain rate
η	shear viscosity
\mathcal{E}	Young's modulus
E	evaporation
ϵ	strain tensor
ϵ_a	emissivity of the atmosphere
ϵ_s	emissivity of the ice / ocean surface
e	yield rate axis ratio
$e_{v,a}$	vapor pressure in the air
f	Coriolis parameter

\mathcal{F}^S	salt flux
\vec{F}_u	non-linear advection
γ	angular zenith distance
\vec{g}	gravitational acceleration
H	water column height
H_S	sea surface elevation
h_i	sea ice thickness
h_s	snow layer thickness
K_h	horizontal diffusion coefficient
K_v	vertical diffusion coefficient
\vec{k}_v	vertical unit vector
L_e	latent heat of evaporation (of water)
L_f	latent heat of fusion (of water)
m	mass of ice (and snow) per unit area
M_{da}	molar mass of dry air
M_w	molar mass of water
\mathcal{P}	formation potential
P	precipitation
P_i	ice strength
P^*	empirical factor in ice strength
p	baroclinic pressure anomaly
p_a	sea level atmospheric pressure
Q	ocean surface heat flux
Q_{ao}	atmosphere / ocean heat flux
Q_l	latent heat flux
Q_{lw}	longwave heat flux
Q_{oi}	ice / ocean heat flux
Q_{ow}	oceanic heat flux in open water areas
Q_{sw}	shortwave heat flux
q	specific humidity
q_s	saturated surface specific humidity
ρ	density
ρ_0	mean sea water density
ρ_a	air density
ρ_i^*	assumed constant sea ice density
ρ_o	ocean surface density

ρ_o^*	assumed constant ocean surface density
ρ_s^*	assumed constant snow density
ρ_w	fresh water density
S	salinity
S^*	salinity chosen to represent a water mass
\mathcal{S}_0	solar constant
S_i	salinity of sea ice
S_o^*	ocean surface salinity
σ	internal stress tensor
σ_B	Stefan-Boltzmann constant
T	potential temperature
T^*	potential temperature chosen to represent a water mass
T_a	air temperature
T_f	freezing point temperature
T_o	ocean surface temperature
t	time
$\vec{\tau}_{ai}$	wind stress
$\vec{\tau}_{ao}$	atmosphere / ocean stress
$\vec{\tau}_{io}$	ice / ocean stress
$\vec{\tau}_o$	ocean surface stress
\vec{u}	threedimensional ocean velocity
u	zonal velocity
u_*	friction velocity
\vec{u}_{10}	(horizontal) 10-m wind velocity
\vec{u}_h	horizontal ocean velocity
\vec{u}_i	(horizontal) velocity of the sea ice
\vec{u}_o	(horizontal) ocean surface velocity
v	meridional velocity
w	vertical velocity
x	zonal distance
y	meridional distance
ζ	bulk viscosity
z	vertical distance

Abbreviations

AABW	Antarctic Bottom Water
ACC	Antarctic Circumpolar Current
AMSR-E	Advanced Microwave Scanning Radiometer for Earth Observing System
ASW	Antarctic Surface Water
AVHRR	Advanced Very High Resolution Radiometer
ca.	circa
CDW	Circumpolar Deep Water
cf.	compare
COSMO	Model of the COnsortium for Small-scale MOdelling
DWD	Deutscher Wetterdienst; German meteorological service
e.g.	for example
ECMWF	European Centre for Medium-Range Weather Forecasts
ESW	Eastern Shelf Water
FEM	Finite Element Method
FEOM	Finite Element Ocean Model
FESIM	Finite Element Sea Ice Model
FESOM	Finite Element Sea ice-Ocean Model
GME	Global Model Europe
HSMP	High Salinity Mixing Partner
HSSW	High Salinity Shelf Water
i.e.	that is
ISW	Ice Shelf Water
LCDW	Lower Circumpolar Deep Water
MWDW	Modified Warm Deep Water
NCEP	NCEP/NCAR Reanalysis
NOAA	National Oceanic and Atmospheric Administration
rms	root mean square
SOI	Southern Oscillation Index
SPP	Schwerpunktprogramm
SSH	sea surface height
SSM/I	Special Sensor Microwave Imager
UCDW	Upper Circumpolar Deep Water
WDW	Warm Deep Water

WSDW Weddell Sea Deep Water
WW Winter Water

List of Tables

2.1	Depths of the horizontal z-layers of the model's implementation.	37
3.1	CTD-Stations used in the on-shelf comparison	57
3.2	CTD-Stations used in the comparison of Section S. Part I.	62
3.3	CTD-Stations used in the comparison of Section S. Part II.	63
4.1	Regional winter mean heat flux and sea ice production	76
4.2	Regional winter mean wind speed, air temperature and specific humidity . .	78
6.1	Forcing comparison in Ronne region	124
6.2	Forcing comparison in Antarctic Peninsula region	124
6.3	Forcing comparison in Coats Land region	126
6.4	Forcing comparison in the Southwestern Weddell Sea	127

List of Figures

1.1	Map of the Weddell Sea	17
1.2	Pathways of the Weddell Sea waters	19
1.3	Water masses of the Weddell Sea	21
2.1	Surface grid and bathymetry	35
2.2	Surface grid and bathymetry in the southwestern Weddell Sea	36
2.3	COSMO coverage	40
3.1	Multi-year mean of sea ice concentration March / September	47
3.2	Polynya event in November 1992	48
3.3	Polynya event in May / June 2008	49
3.4	Sea ice thickness measured by ULS and simulated	53
3.5	Ronne Ice Shelf front on May 6, 2000	56
3.6	Locations of temperature and salinity profiles	57
3.7	Observed and simulated temperature and salinity profiles	58
3.8	Salinity and temperature at Section S	59
3.9	Salinity and temperature at Section S: upper 500 m	60
4.1	Southwestern Weddell Sea and Brunt, Ronne and Antarctic Peninsula regions	66
4.2	Mean seasonal cycle of ice production and surface fluxes	67
4.3	Winter mean maps of the southwestern Weddell Sea surface fluxes	71
4.4	Regional winter mean polynya area	74
4.5	Regional winter mean heat flux	75
4.6	Regional winter mean of main forcing fields	80
4.7	Regional winter mean sea ice production per unit area	82
4.8	Regional winter mean integrated sea ice production	83
5.1	Fresh water balance	88
5.2	Map of winter surface and bottom salinity	89
5.3	Bottom salinity snapshot and Locations I-VI	90

LIST OF FIGURES

5.4	Surface and bottom salinities at Locations I-IV	91
5.5	Surface and bottom temperatures at Locations I-IV	92
5.6	Map showing the demarcation lines D_E (white) and D_{700} (black).	95
5.7	HSSW volume and export	96
5.8	T-S-diagram illustrating the mixing principle of the formation potential	98
5.9	HSSW and HSMP export	100
6.1	Polynya event in August 2008: Forcing comparison	107
6.2	Comparison of mean wind fields April-August	110
6.3	Comparison of mean air temperatures April-August	111
6.4	Comparison of mean sea ice concentrations April-August	113
6.5	Comparison of mean sea ice production April-August	115
6.6	Comparison of bottom salinity increase during April-August	117
6.7	Comparison of HSSW during 2007-2009	118
6.8	Atmospheric variables and sea ice concentration in Ronne region	121
6.9	Sea ice production in Ronne region	123
6.10	Coats Land region	125

Bibliography

- Ackley, S., Geiger, C., King, J., Hunke, E., and Comiso, J. (2001). The Ronne polynya of 1997/98: Observations of air-ice-ocean interaction. *Annals of Glaciology*, 33(1):425–429.
- Andreas, E. L. and Cash, B. A. (1999). Convective heat transfer over wintertime leads and polynyas. *J. Geophys. Res.*, 104(C11):25,721–25,734.
- Andreas, E. L., Claffy, K. J., and Makshtas, A. P. (2000). Low-level atmospheric jets and inversions over the western Weddell Sea. *Boundary-Layer Meteorology*, 97(3):459–486. doi:10.1023/A:1002793831076.
- Arrigo, K. R., Robinson, D. H., Worthen, D. L., Dunbar, R. B., DiTullio, G. R., VanWoert, M., and Lizotte, M. P. (1999). Phytoplankton community structure and the drawdown of nutrients and CO₂ in the Southern Ocean. *Science*, 283:365–367.
- Baldauf, M., Förstner, J., Klink, S., Reinhardt, T., Schraff, C., Seifert, A., and Stephan, K. (2011). Kurze Beschreibung des Lokal-Modells Kürzestfrist COSMO-DE (LMK) und seiner Datenbanken auf dem Datenserver des DWD. Technical report, Deutscher Wetterdienst, Offenbach, Germany. 75 pages.
- Barber, D. G. and Massom, R. A. (2007). A bi-polar assessment of modes of polynya formation. In Smith, W. O. and Barber, D. G., editors, *Polynyas: Windows to the World's Oceans*, pages 1–54. Elsevier, Amsterdam. (ISBN-13: 978-0444529527).
- Bindoff, N., Williams, G., and Allison, I. (2001). Sea-ice growth and water-mass modification in the Mertz Glacier polynya, East Antarctica, during winter. *Annals of Glaciology*, 33:399–406.
- Carmack, E. and Foster, T. (1975a). Circulation and distribution of oceanographic properties near the Filchner Ice Shelf. *Deep-Sea Research*, 22:77–90.
- Carmack, E. and Foster, T. (1975b). On the flow of water out of the Weddell Sea. *Deep-Sea Research*, 22:711–724.

- Carter, L., McCave, I., and Williams, M. J. (2008). Chapter 4 Circulation and water masses of the Southern Ocean: A review. In Florindo, F. and Siegert, M., editors, *Antarctic Climate Evolution*, volume 8 of *Developments in Earth and Environmental Sciences*, pages 85–114. Elsevier. doi:10.1016/S1571-9197(08)00004-9.
- Cavalieri, D., Parkinson, C., Gloersen, P., and Zwally, H. J. (2008). *Sea ice concentrations from Nimbus-7 SMMR and DMSP SSM/I passive microwave data, Jan. 79 - Jun. 06*. National Snow and Ice Data Center, Boulder, Colorado, USA. Digital media.
- Cavalieri, D. J. and Martin, S. (1985). A passive microwave study of polynyas along the Antarctic Wilkes Land coast. In Jacobs, S., editor, *Oceanology of the Antarctic Continental Shelf, Antarctic Research Series 43*, pages 227–252. AGU, Washington, D. C. doi:10.1029/AR043p0227.
- Comiso, J. C. (1995). SSM/I sea ice concentrations using the Bootstrap algorithm. Technical report, NASA Ref. Publication 1380. 49 pages.
- Comiso, J. C. and Gordon, A. L. (1998). Interannual variability in summer sea ice minimum, coastal polynyas and bottom water formation in the Weddell Sea. In Jeffries, O., editor, *Antarctic Sea Ice: Physical Processes, Interactions and Variability*, pages 293–315. Antarct. Res. Ser., vol. 74, AGU, Washington, D. C. doi:10.1029/AR074p0273.
- Cunningham, S. A., Alderson, S. G., King, B. A., and Brandon, M. A. (2003). Transport and variability of the Antarctic Circumpolar Current in Drake Passage. *J. Geophys. Res.*, 108(C5):8084. doi:10.1029/2001JC001147.
- Danilov, S., Kivman, G., and Schröter, J. (2004). A finite element ocean model: Principles and evaluation. *Ocean Modelling*, 6:125–150.
- Deacon, G. (1937). The hydrology of the Southern Ocean. *Discovery Reports*, 15. 124 pages.
- Deacon, G. E. R. (1979). The Weddell Gyre. *Deep-Sea Research I*, 26A:981–995.
- Doms, G., Förstner, J., Heise, E., Herzog, H.-J., Raschendorfer, M., Schrodin, R., Reinhardt, T., and Vogel, G. (2005). A description of the nonhydrostatic regional model LM. Part II: Physical parameterization. Technical report, Deutscher Wetterdienst, Offenbach, Germany. 118 pages.
- Doms, G. and Schättler, U. (2002). A description of the nonhydrostatic regional model LM. Part I: Dynamics and Numerics. Technical report, Deutscher Wetterdienst, Offenbach, Germany. 134 pages.

- Drucker, R., Martin, S., and Kwok, R. (2011). Sea ice production and export from coastal polynyas in the Weddell Sea. *Geophys. Res. Letters*, 38(L17502). doi:10.1029/2011GL048668.
- Ernstorf, T., Schröder, D., Adams, S., Heinemann, G., and Timmermann, R. (2011). Impact of atmospheric forcing data on simulations of the Laptev Sea polynya dynamics using the sea-ice ocean model FESOM. *J. Geophys. Res.*, 116(C12038). doi:10.1029/2010JC006725.
- Fahrbach, E. and Beckmann, A. (2001). Weddell Sea circulation. In Steele, J. H., Thorpe, S. A., and Turekian, K. K., editors, *Encyclopedia of ocean sciences*, pages 3201–3208. Academic Press.
- Fahrbach, E., Hoppema, M., Rohardt, G., Boebel, O., Klatt, O., and Wisotzki, A. (2011). Warming of deep and abyssal water masses along the Greenwich meridian on decadal time scales: The Weddell gyre as a heat buffer. *Deep Sea Res. II: Topical Stud. in Oceanogr.*, 58:2509–2523. doi:10.1016/j.dsr2.2011.06.007.
- Fahrbach, E., Hoppema, M., Rohardt, G., Schröder, M., and Wisotzki, A. (2004). Decadal-scale variations of water mass properties in the deep Weddell Sea. *Ocean Dyn.*, 54:77–91. doi:10.1007/s10236-003-0082-3.
- Fahrbach, E., Rohardt, G., and Krause, G. (1992). The Antarctic Coastal Current in the southeastern Weddell Sea. *Polar Biology*, 12:171–182.
- Fahrbach, E., Rohardt, G., Schröder, M., and Strass, V. (1994). Transport and structure of the Weddell Gyre. *Ann. Geophysicae*, 12:840–855.
- Fiedler, E. K., Lachlan-Cope, T. A., Renfrew, I. A., and King, J. C. (2010). Convective heat transfer over thin ice covered coastal polynyas. *J. Geophys. Res.*, 115(C10051). doi:10.1029/2009JC005797.
- Fischer, H. (1995). Vergleichende Untersuchungen eines optimierten dynamisch-thermodynamischen Meereismodells mit Beobachtungen im Weddellmeer. *Berichte zur Polarforschung 166*. Alfred-Wegener-Institut, Bremerhaven.
- Foldvik, A. and Gammelsrød, T. (1988). Notes on Southern Ocean hydrography, sea-ice and bottom water formation. *Palaeogeography, Palaeoclimatology, Palaeoecology*, 67(1-2):3–17.

- Foldvik, A., Gammelsrød, T., Nygaard, E., and Østerhus, S. (2001). Current measurements near Ronne Ice Shelf: Implications for circulation and melting. *J. Geophys. Res.*, 106:4463–4477.
- Foldvik, A., Gammelsrød, T., Østerhus, S., Fahrbach, E., Rohardt, G., Schröder, M., Nicholls, K. W., Padman, L., and Woodgate, R. A. (2004). Ice shelf water overflow and bottom water formation in the southern Weddell Sea. *J. Geophys. Res.*, 109(C02015). doi:10.1029/2003JC002008.
- Foldvik, A., Gammelsrød, T., and Tørresen, T. (1985a). Circulation and water masses on the southern Weddell Sea shelf. In Jacobs, S., editor, *Oceanology of the Antarctic Continental Shelf. Antarctic Research Series 43*. American Geophysical Union, Washington, D. C. doi:10.1029/AR043p0005.
- Foldvik, A., Gammelsrød, T., and Tørresen, T. (1985b). Hydrographic observations from the Weddell Sea during the Norwegian Antarctic Research Expedition 1976/77. *Polar Research*, 3:177–193.
- Foster, T. D. and Carmack, E. C. (1976). Frontal zone mixing and Antarctic Bottom Water formation in the southern Weddell Sea. *Deep Sea Res.*, 23(4):301–317.
- Gill, P. and Thiele, D. (1997). A winter sighting of killer whales (*Orcinus orca*) in Antarctic sea ice. *Polar Biol.*, 17(5):401–4.
- Gordon, A. L. (1966). Potential temperature, oxygen and circulation of bottom water in the Southern Ocean. *Deep-Sea Research*, 13:1125–1138.
- Gordon, A. L. (1978). Deep Antarctic convection west of Maud Rise. *J. Phys. Oceanogr.*, 8:600–612.
- Gordon, A. L. (1993). Weddell Sea exploration from ice station. *Eos Trans. AGU*, 74(11):121–126. doi:10.1029/93EO00260.
- Gordon, A. L. (1998). Western Weddell Sea thermohaline stratification. In Jacobs, S. and Weiss, R., editors, *Ocean, Ice and Atmosphere: Interactions at the Antarctic Continental Margin*, pages 215–240. Antarct. Res. Ser., vol. 75, AGU, Washington, D. C.
- Gordon, A. L., Visbeck, M., and Huber, B. (2001). Export of Weddell Sea Deep and Bottom Water. *J. Geophys. Res.*, 106(C5):9005–9017.
- Gouretski, V. V. and Danilov, A. I. (1993). Weddell gyre: structure of the eastern boundary. *Deep Sea Research I*, 40(3):561–582. doi:10.1016/0967-0637(93)90146-T.

- Grosfeld, K., Schröder, M., Fahrbach, E., Gerdes, R., and Mackensen, A. (2001). How iceberg calving and grounding change the circulation and hydrography in the Filchner Ice Shelf-ocean system. *J. Geophys. Res.*, 106:9039–9055.
- Haine, T. W. N., Watson, A. J., Liddicoat, M. I., and Dickson, R. R. (1998). The flow of Antarctic Bottom Water to the southwest Indian Ocean estimated using CFCs. *J. Geophys. Res.*, 103(C12):27637–27653.
- Heinemann, G. (2008). The polar regions: a natural laboratory for boundary layer meteorology – a review. *Meteorologische Zeitschrift*, 17(5):589–601. doi:10.1127/0941-2948/2008/0327.
- Hellmer, H. H. and Beckmann, A. (2001). The Southern Ocean: a ventilation contributor with multiple sources. *Geophys. Res. Letters*, 28:2927–2930.
- Hellmer, H. H., Huhn, O., Gomis, D., and Timmermann, R. (2011). *Physical oceanography during POLARSTERN cruise ANT-IX/2 on section SR04*. Alfred Wegener Institute for Polar and Marine Research, Bremerhaven. doi:10.1594/PANGAEA.735277.
- Heuzé, C., Heywood, K. J., Stevens, D. P., and Ridley, J. K. (2013). Southern Ocean bottom water characteristics in CMIP5 models. *Geophysical Research Letters*, 40. doi:10.1002/grl.50287.
- Huhn, O., Rhein, M., Hoppema, M., and van Heuven, S. (2013). Decline of deep and bottom water ventilation and slowing down of anthropogenic carbon storage in the Weddell Sea, 1984–2011. *Deep Sea Res. I: Oceanogr. Res. Papers*, 76:66–84. doi:10.1016/j.dsr.2013.01.005.
- Hunke, E. C. and Comeau, D. (2011). Sea ice and iceberg dynamic interaction. *J. Geophys. Res.*, 116(C05008). doi:10.1029/2010JC006588.
- Hunke, E. C. and Dukowicz, J. K. (1997). An elastic-viscous-plastic model for sea ice dynamics. *J. Phys. Ocean.*, 27:1849–1868.
- Hunke, E. C. and Lipscomb, W. H. (2010). CICE: The Los Alamos Sea Ice Model, Documentation and Software User's Manual, version 4.1, la-cc-06-012. Technical report, Los Alamos National Laboratory, Los Alamos, USA. 76 pages.
- Huybrechts, P. (2002). Sea-level changes at the LGM from ice-dynamic reconstructions of the Greenland and Antarctic ice sheets during the glacial cycles. *Quaternary Science Reviews*, 21(1-3):203–231. doi:10.1016/S0277-3791(01)00082-8.

- Jackett, D. R. and McDougall, T. J. (1995). Stabilization of hydrographic data. *Journal of Atmospheric and Oceanic Technology*, 12:381–389. doi:10.1029/2000JC000720.
- Jenkins, A. (2006a). *Physical oceanography during cruise ROPEX at CTD station ROPEX_084-1*. British Antarctic Survey, Cambridge. doi:10.1594/PANGAEA.527727.
- Jenkins, A. (2006b). *Physical oceanography during cruise ROPEX at CTD station ROPEX_085-1*. British Antarctic Survey, Cambridge. doi:10.1594/PANGAEA.527728.
- Jenkins, A. (2006c). *Physical oceanography during cruise ROPEX at CTD station ROPEX_086-1*. British Antarctic Survey, Cambridge. doi:10.1594/PANGAEA.527729.
- Jenkins, A., Holland, D. M., Nicholls, K. W., Schröder, M., and Østerhus, S. (2004). Seasonal ventilation of the cavity beneath Filchner-Ronne Ice Shelf simulated with an isopycnic coordinate ocean model. *J. Geophys. Res.*, 109(C01024). doi:10.1029/2001JC001086.
- Jourdain, N. C. and Gallée, H. (2011). Influence of the orographic roughness of glacier valleys across the Transantarctic Mountains in an atmospheric regional model. *Climate Dynamics*, 36(5-6):1067–1081. doi:10.1007/s00382-010-0757-7.
- Kalnay, E., Kanamitsu, M., Kistler, R., Collins, W., Deaven, D., Gandinand, L., Iredell, M., Saha, S., White, G., Woollen, J., Zhu, Y., Chelliah, M., Ebisuzaki, W., Higgins, W., Janowiak, J., Mo, K., Ropelewski, C., Wang, J., Leetmaa, A., Reynolds, R., Jenne, R., and Joseph, D. (1996). The NCEP/NCAR 40-year reanalysis project. *Bulletin of the American Meteorological Society*, 77:437–471.
- Klatt, O. (2002). Interpretation von FCKW-Datensätzen im Weddellmeer. *Dissertation*. University of Bremen, Bremen, Germany. http://webdoc.sub.gwdg.de/ebook/diss/2003/sub-bremen/dissertations/E-Diss295_a.pdf.
- König-Langlo, G. and Augstein, E. (1994). Parameterization of the downward long-wave radiation at the earth's surface in polar regions. *Meteorol. Zeitschrift*, 3(6):343–347.
- Kottmeier, C. and Engelbart, D. (1992). Generation and atmospheric heat exchange of coastal polynyas in the Weddell Sea. *Boundary-Layer Meteorology*, 60:207–234.
- Kottmeier, C. and Sellmann, L. (1996). Atmospheric and oceanic forcing of Weddell Sea ice motion. *J. Geophys. Res.*, 101(C9):20809–20824.
- Kusahara, K., Hasumi, H., and Tamura, T. (2004). Modeling water mass formation in the Mertz Glacier Polynya and Adélie Depression, East Antarctica. *J. Geophys. Res.*, 109(C11003). doi:10.1029/2004JC002441.

- Kusahara, K., Hasumi, H., and Tamura, T. (2010). Modeling sea ice production and dense shelf water formation in coastal polynyas around East Antarctica. *J. Geophys. Res.*, 115(C10006). doi:10.1029/2010JC006133.
- Kwok, R. and Comiso, J. (2002). Southern Ocean climate and sea ice anomalies associated with the Southern Oscillation. *J. of Climate*, 15:487–501.
- Laevastu, T. (1960). Factors affecting the temperature of the surface layer of the sea. *Commentat. Phys.-Math.*, 25. 136 pages.
- Lambrecht, A., Sandhäger, H., Vaughan, D., and Mayer, C. (2007). New ice thickness maps of Filchner-Ronne Ice Shelf, Antarctica, with specific focus on grounding lines and marine ice. *Antarctic Science*, 19(4):521–532.
- Leppäranta, M. (1983). A growth model for black ice, snow ice, and snow thickness in subarctic basins. *Nordic Hydrology*, 14:59–70.
- Locarnini, R. A., Whitworth III, T., and Nowlin Jr., W. D. (1993). The importance of the Scotia Sea on the outflow of Weddell Sea Deep Water. *Journal of Marine Research*, 51:135–153.
- Majewski, D., Liermann, D., Prohl, P., Ritter, B., Buchhold, M., Hanisch, T., Paul, G., Wergen, W., and Baumgardner, J. (2002). The operational global icosahedral-hexagonal gridpoint model GME: Description and high-resolution tests. *Monthly Weather Review*, 130:319–338.
- Majewski, D. and Ritter, B. (2002). Das Global-Modell GME. *Promet*, Jahrg. 27(Nr. 3/4):111–122. Deutscher Wetterdienst, Offenbach, Germany.
- Makinson, K., Holland, P. R., Jenkins, A., Nicholls, K. W., and Holland, D. M. (2011). Influence of tides on melting and freezing beneath Filchner-Ronne Ice Shelf, Antarctica. *Geophys. Res. Lett.*, 38(L06601). doi:10.1029/2010GL046462.
- Makinson, K. and Nicholls, K. W. (1999). Modeling tidal currents beneath Filchner-Ronne Ice Shelf and on the adjacent continental shelf: their effect on mixing and transport. *J. Geophys. Res.*, 104(NO. C6):13,449–13,465. doi:10.1029/1999JC900008.
- Makinson, K. and Schröder, M. (2004). Ocean processes and seasonal inflow along Ronne Ice Front. In Smedsrud, L. H., editor, *Forum for Research into Ice Shelf Processes (FRISP)*, pages 11–16. Bjerknes Center for Climate Research, Bergen, Norway.

- Makinson, K., Schröder, M., and Østerhus, S. (2006). Effect of critical latitude and seasonal stratification on tidal current profiles along Ronne Ice Front, Antarctica. *J. Geophys. Res.*, 111(C03022). doi:10.1029/2005JC003062.
- Markus, T. (1996). The effect of the grounded tabular icebergs in front of the Berkner Island on the Weddell Sea ice drift as seen from satellite passive microwave sensors. In *IGARSS '96: Remote sensing for a sustainable future*, pages 1791–1793. IEEE Press, Piscataway, N.J.
- Markus, T. and Burns, B. A. (1995). A method to estimate sub-pixel scale coastal polynyas with satellite passive microwave data. *J. Geophys. Res.*, 100:4473–4487. doi:10.1029/2000JC000720.
- Markus, T., Kottmeier, C., and Fahrbach, E. (1998). Ice formation in coastal polynyas in the Weddell Sea and their impact on oceanic salinity. In Jeffries, O., editor, *Antarctic Sea Ice: Physical Processes, Interactions and Variability*, pages 273–292. Antarct. Res. Ser., vol. 74, AGU, Washington, D. C. doi:10.1029/AR074p0273.
- Martinson, D. G., Killworth, P. D., and Gordon, A. L. (1981). A convective model for the Weddell Polynya. *J. Phys. Oceanogr.*, 11:466–488.
- Massom, R. A., Harris, P. T., Michael, K. J., and Potter, M. J. (1998). The distribution and formative processes of latent-heat polynyas in East Antarctica. *Annals of Glaciology*, 27:420–426.
- Mathiot, P., Jourdain, N. C., Barnier, B., Gallée, H., Molines, J. M., Sommer, J., and Penduff, T. (2012). Sensitivity of coastal polynyas and high-salinity shelf water production in the Ross Sea, Antarctica, to the atmospheric forcing. *Ocean Dynamics*, 62(5):701–723.
- Maykut, G. A. (1977). Estimates of the regional heat and mass balance of the ice cover. In *A Symposium on Sea Ice Processes and Models*, volume I, pages 65–74. University of Washington, Seattle.
- Mensch, M., Bayer, R., Bullister, J. L., Schlosser, P., and Weiss, R. F. (1996). The distribution of tritium and CFCs in the Weddell Sea during the mid-1980s. *Progress in Oceanography*, 38:377–415.
- Meredith, M., Watson, A. J., Van Scoy, K. A., and Haine, T. W. N. (2001). Chlorofluorocarbon-derived formation rates of the deep and bottom waters of the Weddell Sea. *J. Geophys. Res.*, 106:2899–2919.

- Morales Maqueda, M. A., Willmott, A. J., and Biggs, N. R. T. (2004). Polynya dynamics: A review of observations and modelling. *Review of Geophysics*, 42(RG1004). doi:10.1029/2002RG000116.
- Naveira Garabato, A. C., Heywood, K. J., and Stevens, D. P. (2002a). Modification and pathways of Southern Ocean deep waters in the Scotia Sea. *Deep-Sea Research I*, 49:681–705.
- Naveira Garabato, A. C., McDonagh, E. L., Stevens, D. P., Heywood, K. J., and Sanders, R. J. (2002b). On the export of Antarctic Bottom Water from the Weddell Sea. *Deep-Sea Research II*, 49:4715–4742.
- Nicholls, K. W., Boehme, L., Biuw, M., and Fedak, M. A. (2008). Wintertime ocean conditions over the southern Weddell Sea continental shelf, Antarctica. *Geophys. Res. Letters*, 35. L21605, doi:10.1029/2008GL035742.
- Nicholls, K. W., Østerhus, S., Makinson, K., Gammelsrød, T., and Fahrbach, E. (2009). Ice-ocean processes over the continental shelf of the southern Weddell Sea, Antarctica: A review. *Rev. Geophys.*, 47(3):23. RG3003, doi:10.1029/2007RG000250.
- Nicholls, K. W., Padman, L., Schröder, M., Woodgate, R. A., Jenkins, A., and Østerhus, S. (2003). Water mass modification over the continental shelf north of Ronne Ice Shelf, Antarctica. *J. Geophys. Res.*, 108(C8):3260. doi:10.1029/2002JC001713.
- Nihashi, S. and Ohshima, K. I. (2001). Relationship between ice decay and solar heating through open water in the Antarctic sea ice zone. *J. Geophys. Res.*, 106(C8):16767–16782.
- Nowlin Jr., W. D., Whitworth III, T., and Pillsbury, R. D. (1977). Structure and transport of the Antarctic Circumpolar Current at Drake Passage from short-term measurements. *J. Phys. Oceanogr.*, 7:788–802.
- Nowlin Jr., W. D. and Zenk, W. (1988). Westward bottom currents along the margin of the South Shetland Island Arc. *Deep Sea Research*, 35(2):269–301.
- Ohshima, K. I., Yoshida, K., Shimoda, H., Wakatsuchi, M., Endoh, T., and Fukuchi, M. (1998). Relationship between the upper ocean and sea ice during the Antarctic melting season. *J. Geophys. Res.*, 103(C4):7601–7615.
- Orsi, A., Nowlin Jr., W. D., and Whitworth III, T. (1993). On the circulation and stratification of the Weddell Gyre. *Deep-Sea Research I*, 40:169–203.

- Orsi, A., Whitworth III, T., and Nowlin Jr., W. D. (1995). On the meridional extent and fronts of the Antarctic Circumpolar Current. *Deep-Sea Research II*, 44(1–2):23–49.
- Orsi, A. G. J. and Bullister, J. (1999). Circulation, mixing and production of Antarctic Bottom Water. *Progress in Oceanography*, 43:55–109.
- Overland, J. E. and Guest, P. S. (1991). The Arctic snow and air temperature budget over sea ice during winter. *J. Geophys. Res.*, 96:4651–4662.
- Owens, W. B. and Lemke, P. (1997). Sensitivity studies with a sea ice-mixed layer-pycnocline model in the Weddell Sea. *J. Geophys. Res.*, 95(C6):9527–9538.
- Pacanowski, R. C. and Philander, S. G. H. (1981). Parameterization of vertical mixing in numerical models of the tropical oceans. *Journal of Physical Oceanography*, 11:1443–1451.
- Padman, L., Robertson, R., and Nicholls, K. (1998). Modelling tides in the southern Weddell Sea: updated model with new bathymetry from ROPEX. *Filchner-Ronne Ice Shelf Program, Report No. 12*, pages 65–73. Alfred Wegener Institute, Bremerhaven, Germany.
- Parish, T. R. (1983). The influence of the Antarctic Peninsula on the wind field over the western Weddell Sea. *J. Geophys. Res.*, 88(C4):2684–2692. doi:10.1029/JC088iC04p02684.
- Park, Y.-H., Charriaud, E., Craneguy, P., and Kartavtseff, A. (2001). Fronts, transport and Weddell Gyre at 30° E between Africa and Antarctica. *J. Geophys. Res.*, 106(C2):2857–2879.
- Parkinson, C. L. and Washington, W. M. (1979). A large-scale numerical model of sea ice. *J. Geophys. Res.*, 84 (C1):311–337.
- Pease, C. H. (1987). The size of wind-driven coastal polynyas. *J. Geophys. Res.*, 92(C7):7049–7059. doi:10.1029/JC092iC07p07049.
- Purkey, S. and Johnson, G. (2012). Global contraction of Antarctic bottom water between the 1980s and 2000s. *J. Climate*, 25:5830–5844. doi:10.1175/JCLI-D-11-00612.1.
- Raddatz, R. L., Asplin, M. G., Candlish, L., and Barber, D. G. (2011). General characteristics of the Atmospheric Boundary Layer over a flaw lead polynya region in winter and spring. *Boundary-Layer Meteorology*, 138:321–335. doi:10.1007/s10546-010-9557-1.
- Renfrew, I. A. and King, J. C. (2000). A simple model of the convective internal boundary layer and its application to surface heat flux estimates within polynyas. *Boundary-Layer Meteorology*, 94:335–356. doi:10.1023/A:1002793831076.

- Renfrew, I. A., King, J. C., and Markus, T. (2002). Coastal polynyas in the southern Weddell Sea: Variability of the surface energy budget. *J. Geophys. Res.*, 107(C6):3063. doi:10.1029/2000JC000720.
- Rintoul, S. (1998). On the origin and influence of Adélie Land Bottom Water. In Jacobs, S. and Weiss, R., editors, *Ocean, Ice and Atmosphere: Interactions at the Antarctic Continental Margin, Antarctic Research Series 75*, pages 151–171. American Geophysical Union, Washington, DC. (ISBN-13: 978-0444529527).
- Rintoul, S. R. and Sokolov, S. (2001). Baroclinic transport variability of the Antarctic Circumpolar Current south of Australia (WOCE repeat section SR3). *J. Geophys. Res.*, 106(C2):2815–2832.
- Robertson, R., Padman, L., and Egbert, G. D. (1998). Tides in the Weddell Sea. In *Oceanology of the Antarctic Continental Shelf, Antarctic Research Series 75*. American Geophysical Union, Washington, DC.
- Rohardt, G. and Harms, S. (2010). *Physical oceanography during POLARSTERN cruise ANT-XVI/2*. Alfred Wegener Institute for Polar and Marine Research, Bremerhaven. doi:10.1594/PANGAEA.735530.
- Scambos, T., Bohlander, J., and Raup, B. (1996). *Images of Antarctic ice shelves. May 6, 2000*. Boulder, Colorado, USA: National Snow and Ice Data Center. Digital media. http://nsidc.org/data/iceshelves_images/.
- Schodlok, M. P., Hellmer, H. H., and Beckmann, A. (2002). On the transport, variability and origin of dense water masses crossing the South Scotia Ridge. *Deep Sea Research II*, 49(21):4807–4825. doi:10.1016/S0967-0645(02)00160-1.
- Schröder, M. (2010). *Physical oceanography during POLARSTERN cruise ANT-XII/3*. Alfred Wegener Institute for Polar and Marine Research, Bremerhaven. doi:10.1594/PANGAEA.742581.
- Schwerdtfeger, W. (1975). The effect of the Antarctic Peninsula on the temperature regime of the Weddell Sea. *Mon. Weather Rev.*, 1031:45–51.
- Semtner Jr., A. J. (1976). A model for the thermodynamic growth of sea ice in numerical investigations of climate. *J. Phys. Ocean.*, 6(3):379–389.
- Sievers, H. A. and Nowlin Jr., W. D. (1984). The stratification and water masses at Drake Passage. *J. Geophys. Res.*, 89(C6):10489–10514.

- Silva, T. A. M., Bigg, G. R., and Nicholls, K. W. (2006). Contribution of giant icebergs to the Southern Ocean freshwater flux. *J. Geophys. Res.*, 111(C03004). doi:10.1029/2004JC002843.
- Smith, S. D., Muench, R. D., and Pease, C. H. (1990). Polynyas and leads: An overview of physical processes and environment. *J. Geophys. Res.*, 95(C6):9461–9479.
- Spreen, G., Kaleschke, L., and Heygster, G. (2008). Sea ice remote sensing using AMSR-E 89 GHz channels. *J. Geophys. Res.*, 113(C02S03). doi:10.1029/2005JC003384.
- Steele, M., Morley, R., and Ermold, W. (2001). PHC: A global ocean hydrography with a high quality Arctic Ocean. *J. Climate*, 14:2079–2087.
- Steppeler, J., Doms, G., Schättler, U. and Bitzer, H. W., Gassmann, A., Damrath, U., and Gregoric, G. (2003). Meso-gamma scale forecasts using the nonhydrostatic model LM. *Meteorology and Atmospheric Physics*, 82(1-4):75–96.
- Stössel, A., Zhang, Z., and Vihma, T. (2011). The effect of alternative real-time wind forcing on Southern Ocean sea ice simulations. *J. Geophys. Res.*, 116(C11021). doi:10.1029/2011JC007328.
- Tamura, T., Ohshima, K. I., Markus, T., Cavalieri, D. J., Nihashi, S., and Hirasawa, N. (2007). Estimation of thin ice thickness and detection of fast ice from SSM/I data in the Antarctic Ocean. *J. Atmos. Oceanic Technol.*, 24:1757–1772.
- Tamura, T., Ohshima, K. I., and Nihashi, S. (2008). Mapping of sea ice production for Antarctic coastal polynyas. *Geophys. Res. Letters*, 35(L07606). doi:10.1029/2007GL032903.
- Timmermann, R. and Beckmann, A. (2004). Parameterization of vertical mixing in the Weddell Sea. *Ocean Modelling*, 6:83–100.
- Timmermann, R., Danilov, S., Schröter, J., Böning, C., Sidorenko, D., and Rollenhagen, K. (2009). Ocean circulation and sea ice distribution in a finite element global sea ice-ocean model. *Ocean Modelling*, 27:114–129.
- Timmermann, R., Le Brocq, A., Deen, T., Domack, E., Dutrieux, P., Galton-Fenzi, B., Hellmer, H., Humbert, A., Jansen, D., Jenkins, A., Lambrecht, A., Makinson, K., Niederjasper, F., Nitsche, F., Nøst, O. A., Smedsrud, L. H., and Smith, W. H. F. (2010). A consistent dataset of Antarctic ice sheet topography, cavity geometry, and global bathymetry. *Earth System Science Data*, 3(2):261–273. doi:10.5194/essd-2-261-2010.

- Timmermann, R., Lemke, P., and Kottmeier, C. (1999). Formation and maintenance of a polynya in the Weddell Sea. *J. Phys. Oceanogr.*, 29(6):1251–1264.
- Van Dam, R. and Kooyman, G. (2004). Latitudinal distribution of penguins, seals and whales observed during a late autumn transect through the Ross Sea. *Antarct Sci.*, 16:313–318.
- Veth, C., Peeken, I., and Scharek, R. (1997). Physical anatomy of fronts and surface waters in the ACC near the 6° meridian during austral spring 1992. *Deep-Sea Research II*, 44(1–2):23–49.
- Wang, Q. (2007). The Finite Element Ocean Model and its aspect of vertical discretization. *Dissertation*. University of Bremen, Bremen, Germany. <http://nbn-resolving.de/urn:nbn:de:gbv:46-diss000108304>.
- Weppernig, R., Schlosser, P., Khatiwala, S., and Fairbanks, R. G. (1996). Isotope data from Ice Station Weddell: Implications for deep water formation in the Weddell Sea. *J. Geophys. Res.*, 101(C11):25723–25739. doi:10.1029/96JC01895.
- Whitworth III, T. and Nowlin Jr., W. D. (1987). Water masses and currents of the Southern Ocean at the Greenwich Meridian. *J. Geophys. Res.*, 92(C6):6462–6476.
- Whitworth III, T., Nowlin Jr., W. D., and Worley, S. J. (1982). The net transport of the Antarctic Circumpolar Current through Drake Passage. *J. Phys. Oceanogr.*, 12:960–971.
- Williams, G. D. and Bindoff, N. L. (2003). Wintertime oceanography of the Adélie Depression. *Deep-Sea Research II*, 50:1373–1392.
- Windmüller, M. (1997). Untersuchung von atmosphärischen Reanalysedaten im Weddellmeer und Anwendung auf ein dynamisch thermodynamisches Meereismodell. *Diplomarbeit*. Institut für Meereskunde, Christian-Albrechts-Universität, Kiel, Germany. 65 pages.
- Yi, D., Zwally, H. J., and Robbins, J. W. (2011). ICESat observations of seasonal and interannual variations of sea-ice freeboard and estimated thickness in the Weddell Sea, Antarctica (2003–2009). *Annals of Glaciology*, 52(57):43–51.
- Yuan, X. (2004). ENSO-related impacts on Antarctic sea ice: a synthesis of phenomenon and mechanisms. *Antarctic Science*, 16(4):415–425.
- Zillman, J. W. (1972). A study of some aspects of the radiation and heat budgets of the southern hemisphere oceans. In *Meteorological study*, volume 26. Bureau of Meteorology, Dept. of the Interior, Canberra, Australia. 526 pages.

BIBLIOGRAPHY

Zwally, H. J., Comiso, J. C., and Gordon, A. L. (1985). Antarctic offshore leads and polynyas and oceanographic effects. In Jacobs, S., editor, *Oceanology of the Antarctic Continental Shelf, Antarctic Research Series 43*, pages 203–226. AGU, Washington, D. C. doi:10.1029/AR043p0203.